Supplementary Information (SI) for Catalysis Science & Technology.
This journal is © The Royal Society of Chemistry 2025

Towards Superior Efficiency of CO_2-Derived Fischer–Tropsch Synthesis Process over Iron-Based Metal-Organic Framework-derived Multifunctional Catalytic Materials

Shican Jiang[1], Zuozheng Liu[1], Abhishek Dutta Chowdhury[1]*

[1] *College of Chemistry and Molecular Sciences, Wuhan University, Wuhan, 430072, Hubei, PR China.*

**Corresponding author email: abhishek@whu.edu.cn*

Content

S1. Experimental Section

S1.1. Chemicals.

Trimesic acid ($C_9H_6O_6$,98%, Bide Pharmatech Ltd.), methanol (CH_3OH, ≥99%), Iron (II) chloride tetrahydrate ($FeCl_2 \cdot 4H_2O$,98%), Sodium hydroxide (NaOH, ≥99%), Lithium carbonate (Li_2CO_3, ≥99%), Sodium carbonate (Na_2CO_3, ≥99%) and Potassium carbonate (K_2CO_3, ≥99%) were purchased from Sinopharm Chemical Reagent Co. and tetraethyl orthosilicate (TEOS, 99 wt%, Shanghai Macklin, China), tetrapropyl-ammonium hydroxide (TPAOH, 40 wt% in H_2O, HEOWNS, China) were used without further purification. Zeolites (ZSM-5, ZSM-22, ZSM-35, MCM-22) were all purchased from Nankai University Catalyst Co. Ltd. ZSM-11 was obtained from Zhuoran Environmental Protection (Dalian) Co. Ltd. All zeolites were dried at 110 °C for 12 h and then calcined at 550 °C for another 6h. All gases were obtained from Wuhan Zhongxin Ruiyuan Gas Co. Ltd. The deionized water with a resistivity larger than 18.2 MΩ was obtained from the Millipore Milli-Q ultrapure water purification system.

S1.2. Catalyst Preparation.

S1.2.1. Synthesis of MIL-100(Fe): The synthesis recipe was based on the previously reported literature.[1,2] Typically, solution 1 ($pH \approx 11$) containing 1.676 g (7.6 mmol) of H_3BTC dissolved in 23.72 g of 1 M NaOH aqueous solution (22.8 mmol). Solution 2 ($pH \approx 2.7$) was prepared by dissolving 2.26 g (11.4 mmol) of $FeCl_2 \cdot 4H_2O$ in 97.2 g of H_2O. After becoming completely clear solutions in both cases, solution 1 was added dropwise over solution 2 under stirring, giving a mixture with a molar ratio of 1.5 Fe/1.0 H_3BTC/3.0 NaOH/880 H_2O, whose pH was around 5.2. Time zero was taken when the addition of all Solution 1 over Solution 2 was finished. The stirring continued at room temperature for up to 24 h, and some aliquots were taken off at different synthesis times, as mentioned in the respective Figure captions. The solid was recovered by centrifugation at 3700 rpm, and then it was washed three times with water and one more time with methanol. The sample was dried at 70°C overnight. Finally, the product was dried at 150 °C under vacuum for 12 h to acquire a total of 4.20 g of orange powder (79% yield).

S1.2.2. Synthesis of Fe@C and K/Fe@C catalysts: The Fe@C catalysts were obtained by carbonization of the MIL-100(Fe) precursors. The heating was carried out on a tubular oven (Hefei Kejing Material Technology Co. Ltd) at 700°C-900°C for 4 h-16 h with a heating rate of 2 °C/min, under the nitrogen atmosphere. Before the samples were opened to the atmosphere, they were passivated under 2% O_2 in N_2 for 4 h at room temperature. The catalysts were named in a Fe@C(x,y) manner, where x and y refer to the pyrolysis duration (in hours) and temperature (in °C), respectively [i.e., Fe@C<(4/8/16),(700/800/900)>: x=4 hours or 8 hours or 16 hours; y= 700°C or 800°C or 900°C]. For example, the MIL-100(Fe) precursor was heated in a tubular oven at 800 °C for 4 h, which was then named "Fe@C(4,800)" catalyst. The potassium-promoted catalysts were further prepared by incipient wetness impregnation. A certain amount of the potassium carbonate as the potassium precursor to achieve the desired promotion level (as mentioned in the respective Figure captions) was dissolved in a mixture of water and methanol (1:1) and impregnated inside the pores of the Fe@C (black) catalyst under ultrasonic for 15 min, which was then were macerated overnight at room temperature. The resultant material was heated up to 75 °C for 12 h and 350 °C for 2 h under N_2 atmosphere.[3,4] The resultant catalyst is black in color (named as "nK/Fe@C(x,y)" manner) and then stored in a plastic tube at room temperature for later use.

S1.2.3. Synthesis of Silicalite-1 zeolite.

The normal Silicalite-1 zeolite (S1) was prepared by a conventional hydrothermal method.[5] In a typical run, 3.5 g of TEOS was added into a mixture containing 11.28 g of deionized water and 3.3 g of TPAOH (40 wt%), followed by stirring at room temperature for 12 h. Then, the mixture was transferred into an autoclave and heated at 180 °C for 3 days. After removal of the organic template by calcination at 550 °C for 4 h, the Silicalite-1 (S1) zeolite was finally obtained.

S1.3. Catalyst Characterization.

X-ray diffraction patterns (XRD) were obtained in a Bruker D8 equipment in Bragg–Brentano configuration using Cu K radiation. The spectra were scanned with a step size of 0.02° in the 2θ range of 5–90°.The crystalline phase was identified by comparison data from the inorganic crystal structure database, JCPDS. Nitrogen adsorption and desorption isotherms were recorded on a Micromeritics ASAP 2040 at 77 K. Samples (Fe@C catalysts) were previously evacuated at 373 K for 16 h. The BET method was used to calculate the surface area, while the micropore volumes and micropore surface areas were evaluated using the t-plot method. The zeolites were outgassed at 350 °C for 8h before the sorption measurements. The total specific surface area was determined after using the BET method, while the external surface area and micropore volume were derived from the t-plot method. The total pore volume was derived from a single-point measurement at $P/P_0=0.99$. CO_2 temperature-programmed desorption (CO_2-TPD) measurements were performed on the Micromeritics AutoChem II 2920 instrument. Typically, 100 mg of the samples were first dried under an argon atmosphere at 100 °C for 1h. After that, the adsorption of CO_2 was performed at 50 °C in the 10% CO_2-argon (10 vol% CO_2) atmosphere, and the TPD was measured in the He gas flow by raising the temperature from 50 °C to 600 °C. H_2 temperature-programmed desorption (H_2-TPD) measurements were performed on the Micromeritics AutoChem II 2920 instrument. Typically, 100 mg of the samples were first dried under an argon atmosphere at 100 °C for 1h. After that, the adsorption of H_2 was performed at 50 °C in the 10% H_2-argon (10 vol% H_2) atmosphere, and the TPD was measured in the He gas flow by raising the temperature from 50 °C to 800 °C. Temperature-programmed desorption of ammonia (NH_3-TPD) was measured on a MicrotracBel (BELCAT-B, Japan) chemical adsorption instrument. X-ray photoelectron analysis (XPS) was performed with an Axis Ultra DLD (Kratos Tech.) equipment. The spectra were excited by a monochromatized Al Kα source (1486.6 eV) run at 15 kV and 10 mA. For the calibration measurement, C 1s peak at 284.8 eV was used as a reference standard to calibrate the binding energy and the XPS data were processed and analyzed in Avantage software. To verify the outermost surface concentrations on the undoped and potassium-doped catalysts, the intensity ratios of each Fe 2p3/2 and O 1s peaks were calculated by using the integrated areas of each iron and oxygen species. The surface ratios of O to Fe were denoted as I_O/I_{Fe}. X-ray fluorescence spectroscopy (XRF) test was using the ARL Advant X IntellipowerTM 3600 equipment from Thermo Fisher Scientific, USA. Scanning electron microscopy (SEM) and transmission electron microscopy (TEM) were performed on a scanning microscope (Hitachi S4800 field-emission) operated at 15 kV and a transmission electron microscope (Tecnai G2 F30 S-TWIN), respectively. Thermal gravimetric analysis (TGA) using a STA 449 F3 Jupiter® instrument manufactured by NETZSCH in Germany. Typically, 10 mg of the MIL-100(Fe) samples were heated from room temperature to 900 °C at a rate of 10 °C/min in N_2 flow of 30 ml/min. Typically, 10 mg of the Fe@C catalysts or reacted zeolites samples were heated from room temperature to 900 °C at a rate of 10 °C/min in an air flow of 30 ml/min. The Raman spectra were obtained on a LabRAM HR Evolution Raman spectroscopy at a 532 nm laser source.

S1.4. Catalytic Testing.

The performance of CO_2 hydrogenation over catalysts was evaluated using a fixed-bed reactor (Xiamen Hande Engineering Co. Ltd). First, the zeolites and/or K/Fe@C catalyst were compressed and sieved to a mesh size of 20-40. Catalytic activity measurement was carried out by using 50 mg catalyst with 300 mg inert material of SiC in a fixed-bed tubular reactor under the reaction conditions of $T = 350$ °C, $P = 3.0$ MPa, weight hourly space velocity (SV) of 4800-48000 mL/(g_{cat}·h) and $H_2/CO_2/N_2$ (vol%) = 72/24/4 without any previous reductive treatment. The tubes were then pressurized to 30 bar using a pressure controller (Xiamen HanDe Engineering Co., Ltd). 50 mg of the standalone K/Fe@C catalyst and 100 mg of the composite catalyst with K/Fe@C//Zeolite with the mass ratio of 1/1 in a dual bed configuration were typically used (N.B.: All the zeolites were dried at 120 °C for 12 h and calcined at 550 °C for 2 hours before the catalytic testing). A composite catalyst-particle mixing configuration was prepared by simple physical mixing and the stacking of K/Fe@C and zeolites individually with 20–40 meshes. All of the products from the reactor were introduced in a gaseous state and analyzed with two tandem online gas chromatographs (GC, HOPE 9860). N_2, CO, CO_2, H_2, and C1-C4 were analyzed using a GC-1 system with a TCD, an HP-PLOT Q column, and a molecular sieve 5A column. Other organic compounds, including higher hydrocarbons and oxygenates, were analyzed using another GC system equipped with a flame ionization detector (FID) and an HP-PONA capillary column. All connection lines between our reactor and GCs were always heated at 200 °C to avoid any condensation. Proper passivation was conducted before exposure to air to characterize the catalyst used.[6] The conversions (X, %), and selectivities (S, %) are defined as follows [Eqs. (1)–(3)]:

$$X_{co_2} = 1 - \frac{C_{N2,blk} * C_{CO2,R}}{C_{N2,R} * C_{CO2,blk}} \times 100 \qquad (1)$$

$$S_{Cn} = \frac{n * \frac{C_{Cn,R}}{C_{N2,R}}}{\frac{C_{CO2,blk}}{C_{N2,blk}} - \frac{C_{CO2,R}}{C_{N2,R}}} \times 100 \qquad (2)$$

$$S_{co} = 1 - \frac{\frac{C_{CO,R}}{C_{N2,R}}}{\frac{C_{CO2,blk}}{C_{N2,blk}} - \frac{C_{CO2,R}}{C_{N2,R}}} \times 100 \qquad (3)$$

where $C_{N2,blk}$, $C_{N2,R}$, $C_{CO2,blk}$, $C_{CO2,R}$, and $C_{CO2,R}$ are the concentrations determined by GC analysis of N_2 in the blank, N_2 in the reactor effluent, CO_2 in the blank, CO_2 in the reactor effluent and CO in the reactor effluent respectively. $C_{Cn,R}$ is the concentration of the reactor effluent determined by GC analysis of a product with n carbon atoms. The reactions were carried out using MOF-derived catalysts synthesized from various batches to confirm the reliability and consistency of our synthesis protocol. Carbon balances were all higher than 95%. The error in carbon balance was better than 5% in all cases.[3,4,7]

S2. Supplementary Figures.

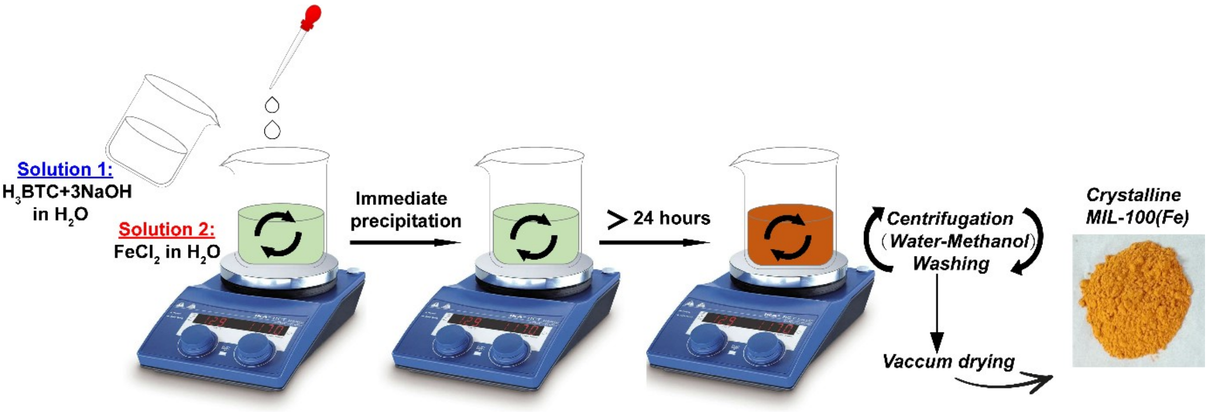

Fig. S1. Simplified illustration of the synthetic protocols of MIL-100 (Fe) room temperature preparation method (see Section S1.2.1 for details).

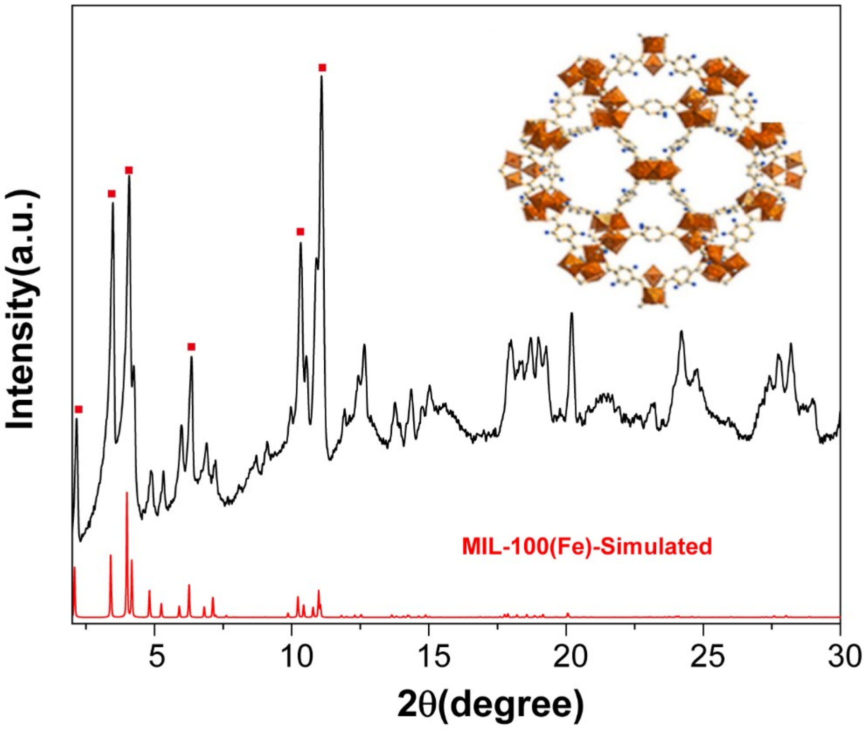

Fig. S2. Wide-angle XRD patterns of the as-prepared MIL-100(Fe) with its simulated patterns. These samples exhibited strong X-ray diffraction intensity, indicating high purity and crystallinity of the obtained MOF-based catalyst precursors. Compared with the simulated XRD spectra, MIL-100(Fe) displays diffraction peaks at positions of 3.1°, 3.8°, and 10.6°, which are consistent with literature reports.[8,9]

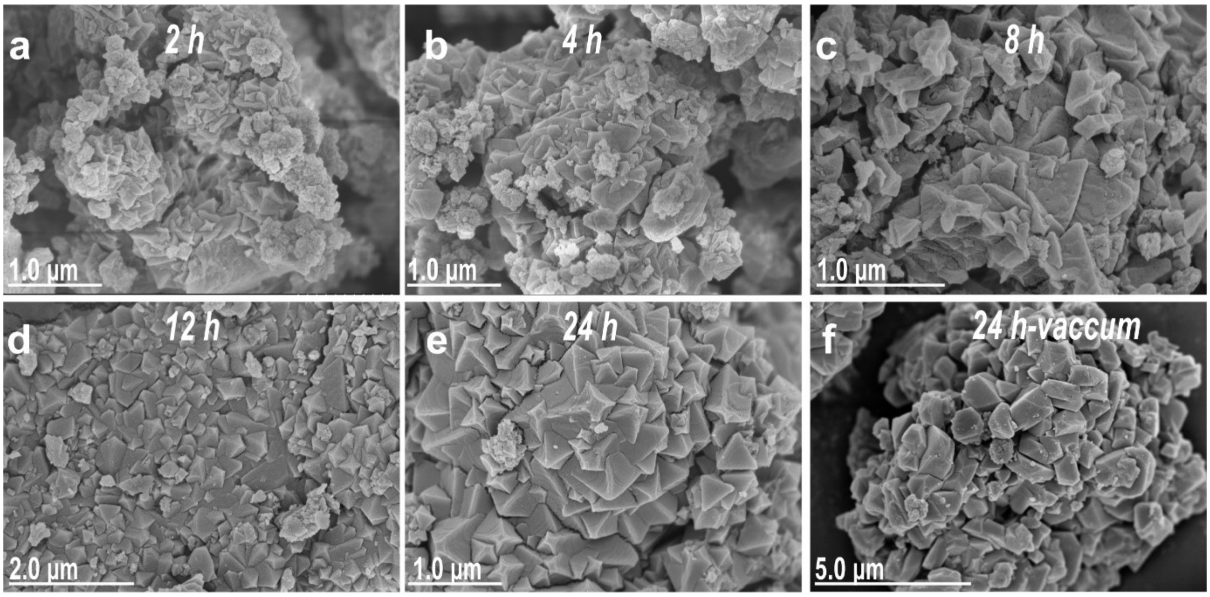

Fig. S3. SEM images of MIL-100(Fe) at different synthesis times.

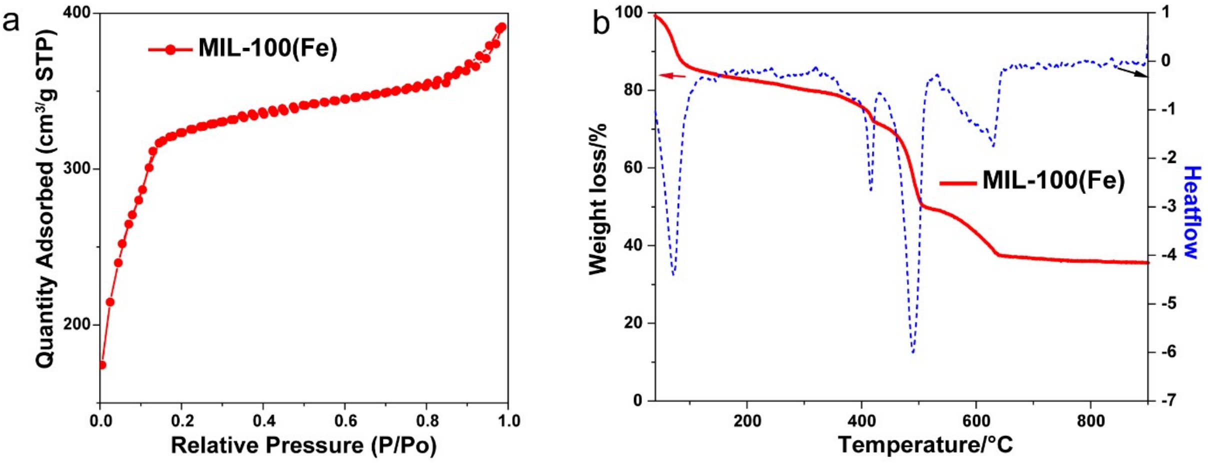

Fig. S4. (a) Nitrogen adsorption/desorption isotherms of MIL-100(Fe) and (b) TGA curve of MIL-100(Fe) under N_2 atmosphere. TGA testing of MIL-100(Fe) under N_2 atmosphere was carried out. The first weight loss occurred below 150°C, attributed to the loss of water in the sample, with a weight loss rate of 15%. The second weight loss between 150°-410°C was due to coordinated water loss, with a weight loss rate of 15%. The third weight loss between 410°-520°C corresponded to the decomposition of terephthalic acid in the framework, with a weight loss rate of 22%. The fourth weight loss between 520°-650°C was associated with the reduction of iron oxide to form iron carbides, iron, and carbon, with a weight loss rate of 11%.[10]

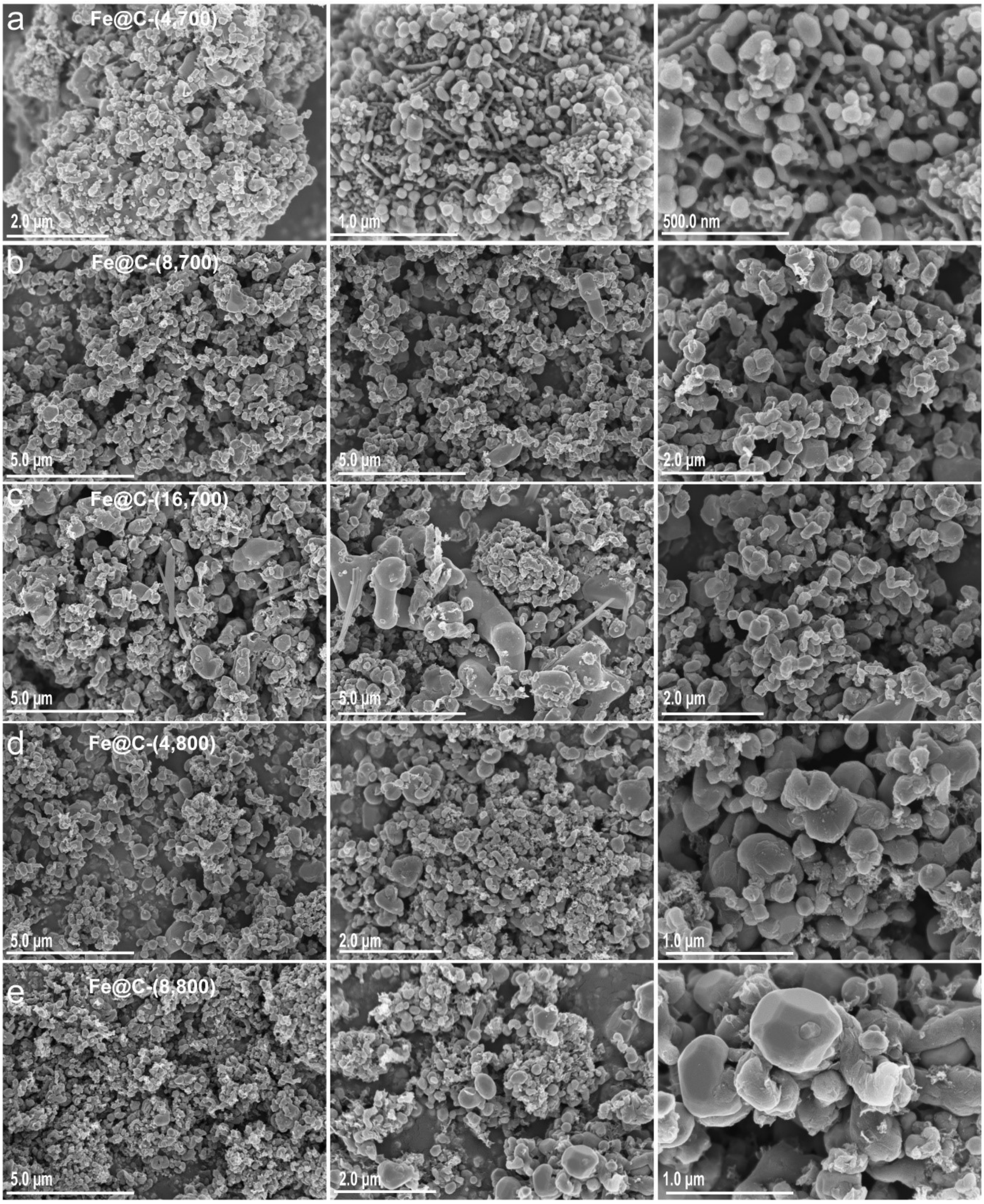

Fig. S5. SEM images of (a) Fe@C(4,700) [Avg. particle size: ~28 nm], (b) Fe@C(8,700) [Avg. particle size:~138 nm], (c) Fe@C(16,700) [Avg. particle size: ~158 nm], (d) Fe@C-(4,800) [Avg. particle size: ~94 nm], and (e) Fe@C-(8,800) [Avg. particle size: ~156 nm] catalysts. Note that synthesized materials were presented in a Fe@C(x,y) manner, where x and y refer to the pyrolysis duration (in hours) and temperature (in °C), respectively.

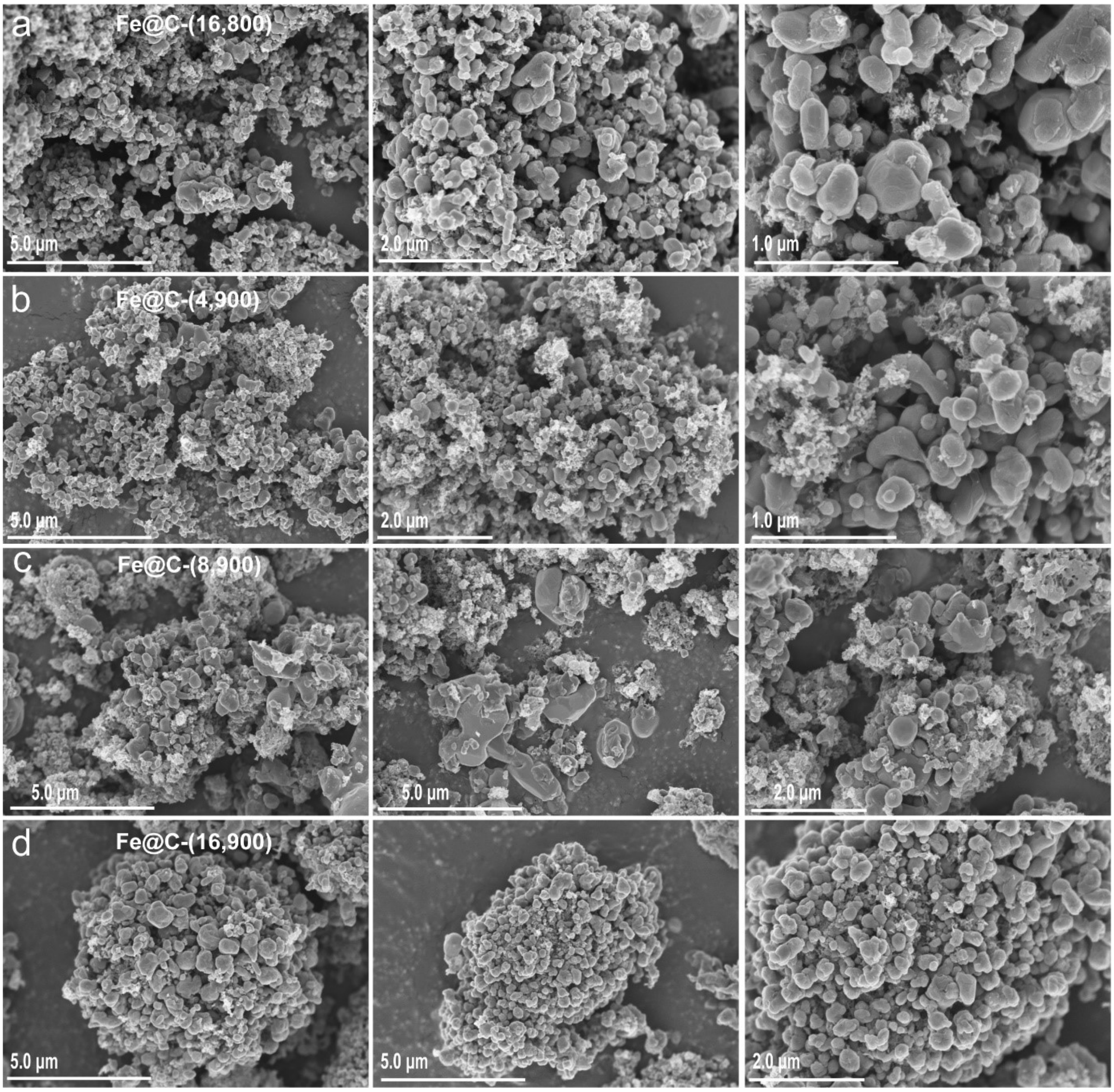

Fig. S6. SEM images of (a) Fe@C(16,800) [Avg. particle size: ~190 nm], (b) Fe@C(4,900) [Avg. particle size: ~172 nm], (c) Fe@C(8,900) [Avg. particle size:~190 nm], and (d) Fe@C-(16,900) [Avg. particle size: ~217 nm] catalysts. Note that synthesized materials were presented in a Fe@C(x,y) manner, where x and y refer to the pyrolysis duration (in hours) and temperature (in °C), respectively.

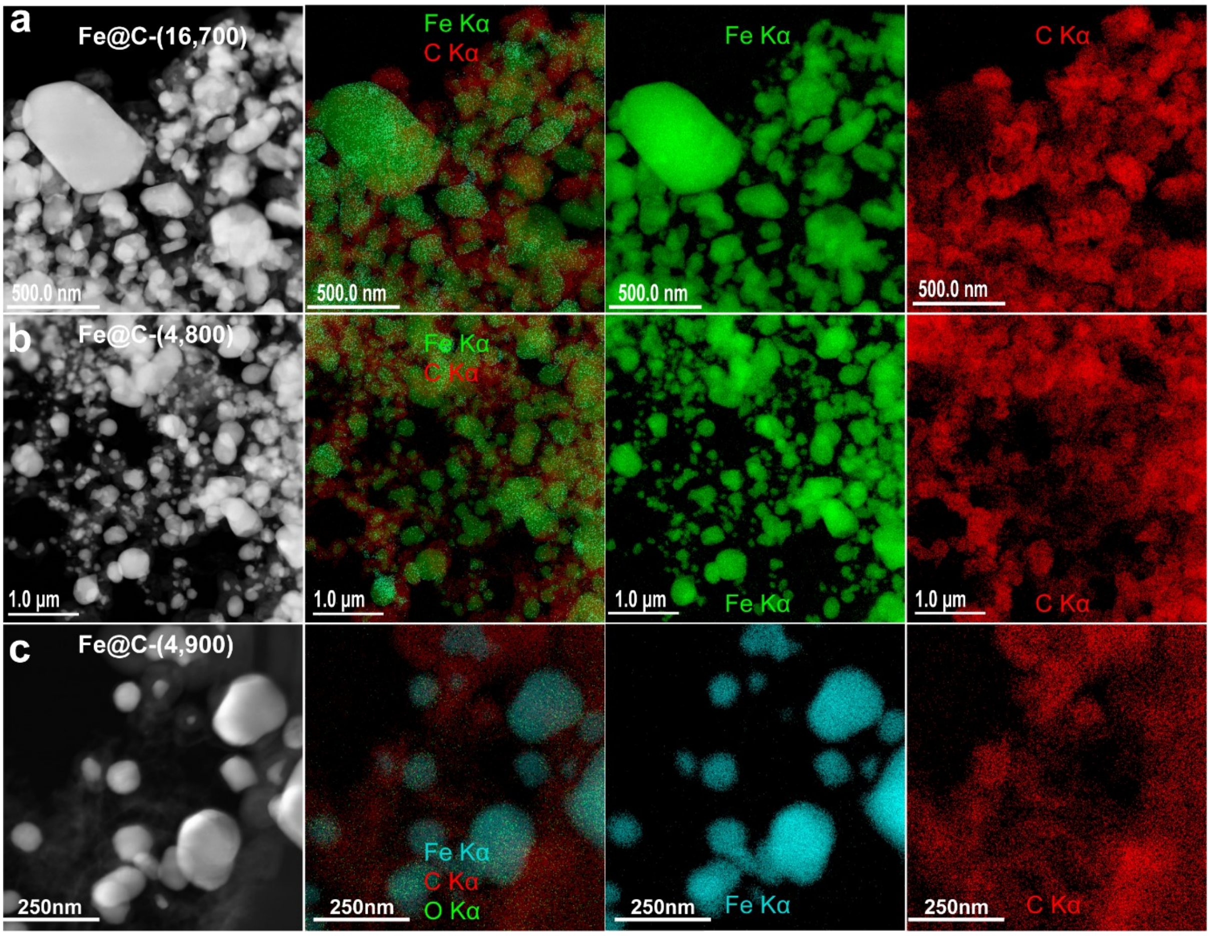

Fig. S7. HAADF-STEM imaging and elemental mapping of (a) Fe@C(16,700), (b) Fe@C(4,800), and (c) Fe@C(4,900) catalysts. Note that synthesized materials were presented in a Fe@C(x,y) manner, where x and y refer to the pyrolysis duration (in hours) and temperature (in °C), respectively. The relatively uniform distribution of the active component Fe was observed over as-synthesized Fe@C materials. Notably, the carbon matrix has encircled the catalytically active Fe-based nanoparticles over as-synthesized Fe@C materials, suggesting uniform embedding of both Fe within the porous carbon-based matrix.

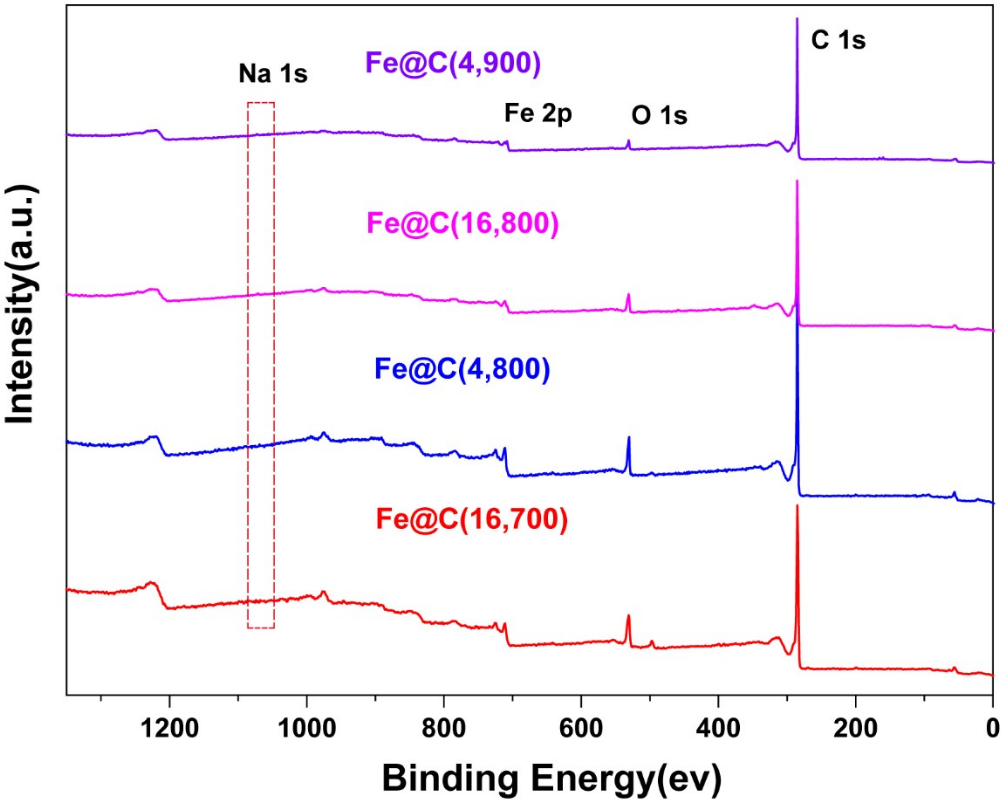

Fig. S8. XPS survey scan of Fe@C(16,700), Fe@C(4,800), Fe@C(16,800), and Fe@C-(4,900) catalysts. Note that synthesized materials were presented in a Fe@C(x,y) manner, where x and y refer to the pyrolysis duration (in hours) and temperature (in °C), respectively. It can be seen that C, O, and Fe are the major elements in the surface. The Na 1s peak was also slightly weaker in all catalysts, possibly due to the NaOH reactant MIL-100 (Fe) during the synthesis process, indicating that the Na element was essentially washed away after adequate rinsing.

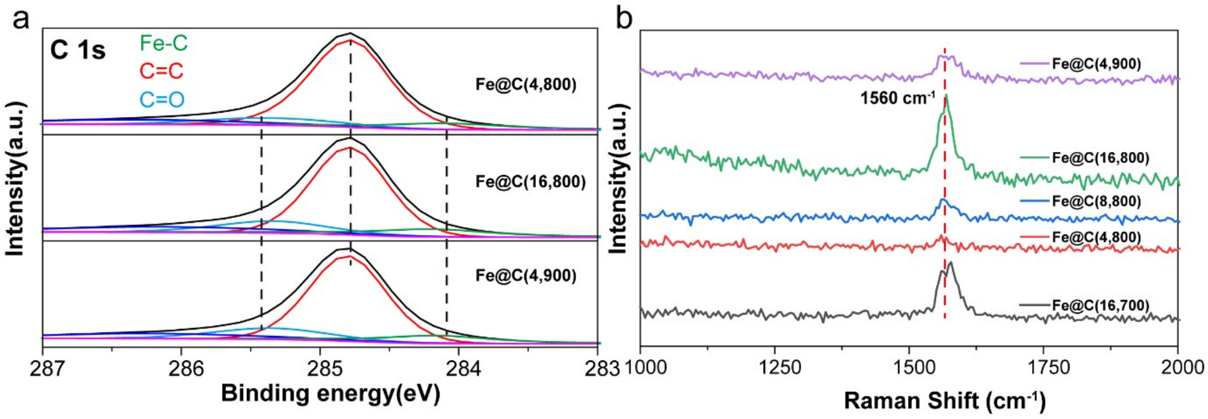

Fig. S9. (a) XPS survey scan of C 1s high-resolution and (b) Raman spectra of Fe@C catalysts for MIL-100-derived Fe@C catalysts. Note that synthesized materials were presented in a Fe@C(x,y) manner, where x and y refer to the pyrolysis duration (in hours) and temperature (in °C), respectively. As the calcination temperature increases, the degree of graphitization increases, and similarly, the degree of graphitization increases as the calcination holding time increases. Raman spectroscopy also showed that the same phenomenon was obtained with the increase in calcination temperature, the enhancement of the G-type peak, and the extension of the holding time.

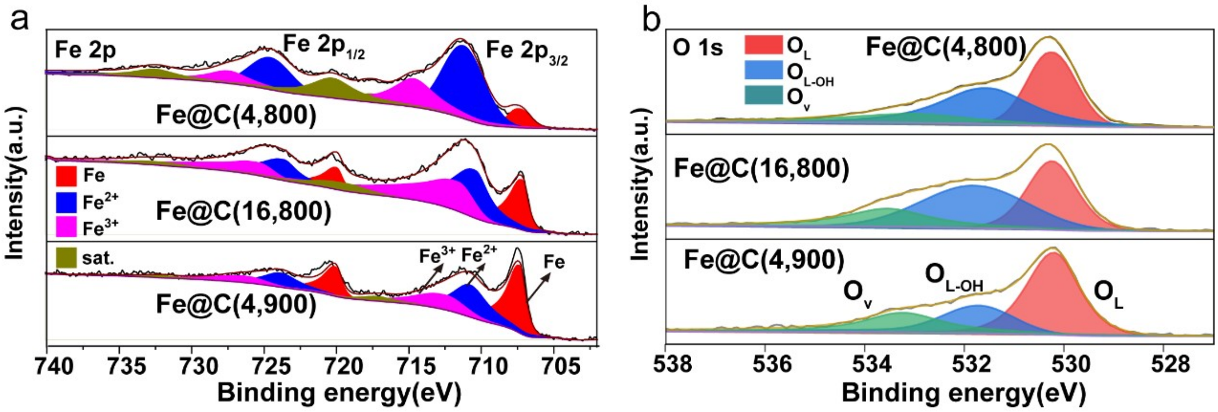

Fig. S10. (a) XPS survey scan of Fe 2p high-resolution and (b) O 1s of Fe@C catalysts for MIL-100-derived Fe@C catalysts. Note that synthesized materials were presented in a Fe@C(x,y) manner, where x and y refer to the pyrolysis duration (in hours) and temperature(in °C), respectively. Peak area displays of XPS Fe 2p. With the increase of calcination temperature, the area of Fe^0 increased from 18.6 for Fe@C (4,800) to 22.7 for Fe@C (16,800) and 44.1 for Fe@C (4,900). Similarly, the Fe^0 area increases as the calcination holding time increases. For the O1s peak area display, the O$_L$ area increased from 34.6 for Fe@C (4,800) to 40.3 for Fe@C (16,800) and 49.9 for Fe@C (4,900).

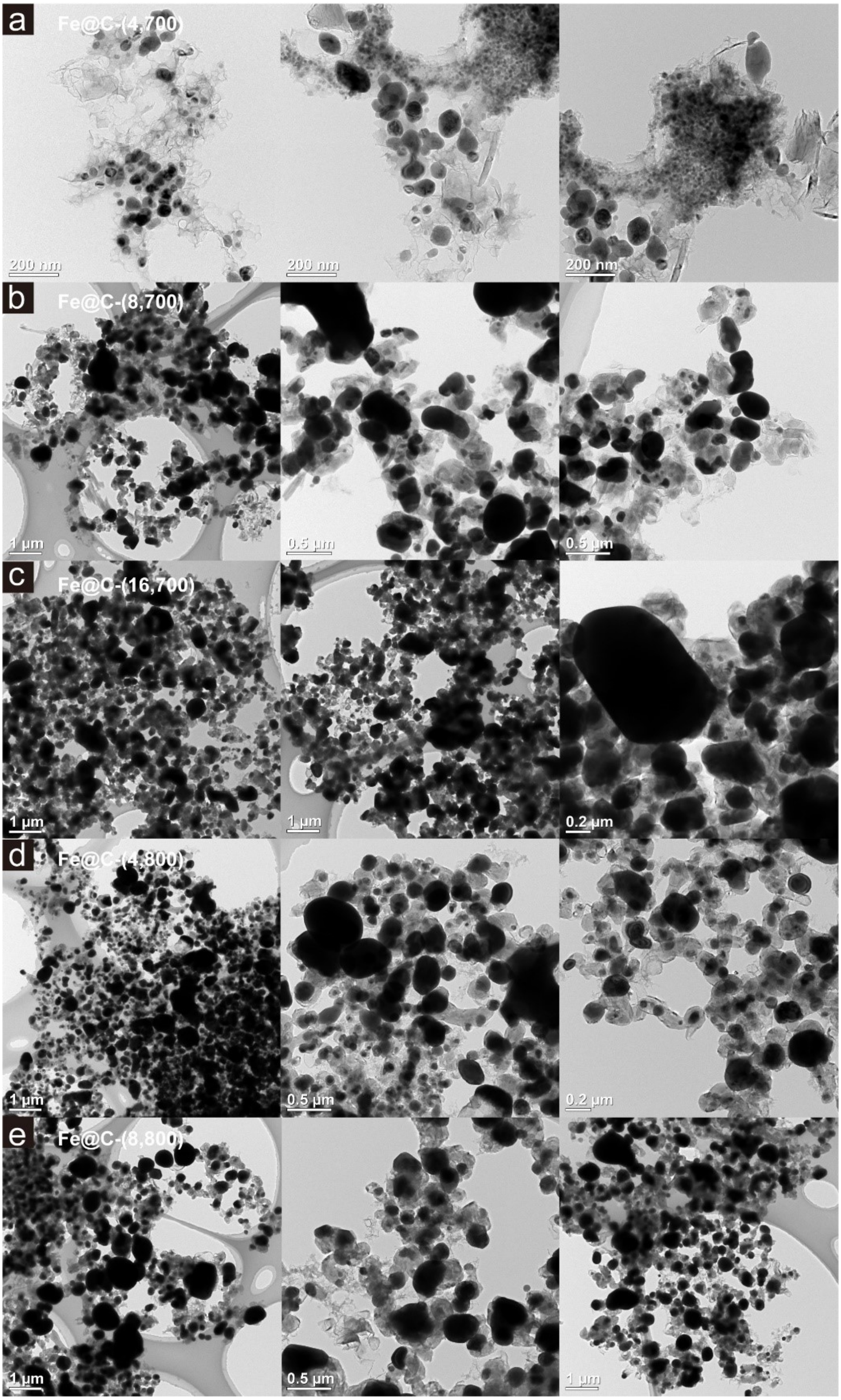

Fig. S11. TEM images of (a) Fe@C(4,700), (b) Fe@C(8,700), (c) Fe@C(16,700), (d) Fe@C-

(4,800), and (e) Fe@C-(8,800) catalysts. Note that synthesized materials were presented in a Fe@C(x,y) manner, where x and y refer to the pyrolysis duration (in hours) and temperature (in °C), respectively. All materials exhibit high dispersion, and the iron nanoparticles are well encased in graphite-carbon shells with a porous structure. The particle size increases with the calcination temperature and holding time.

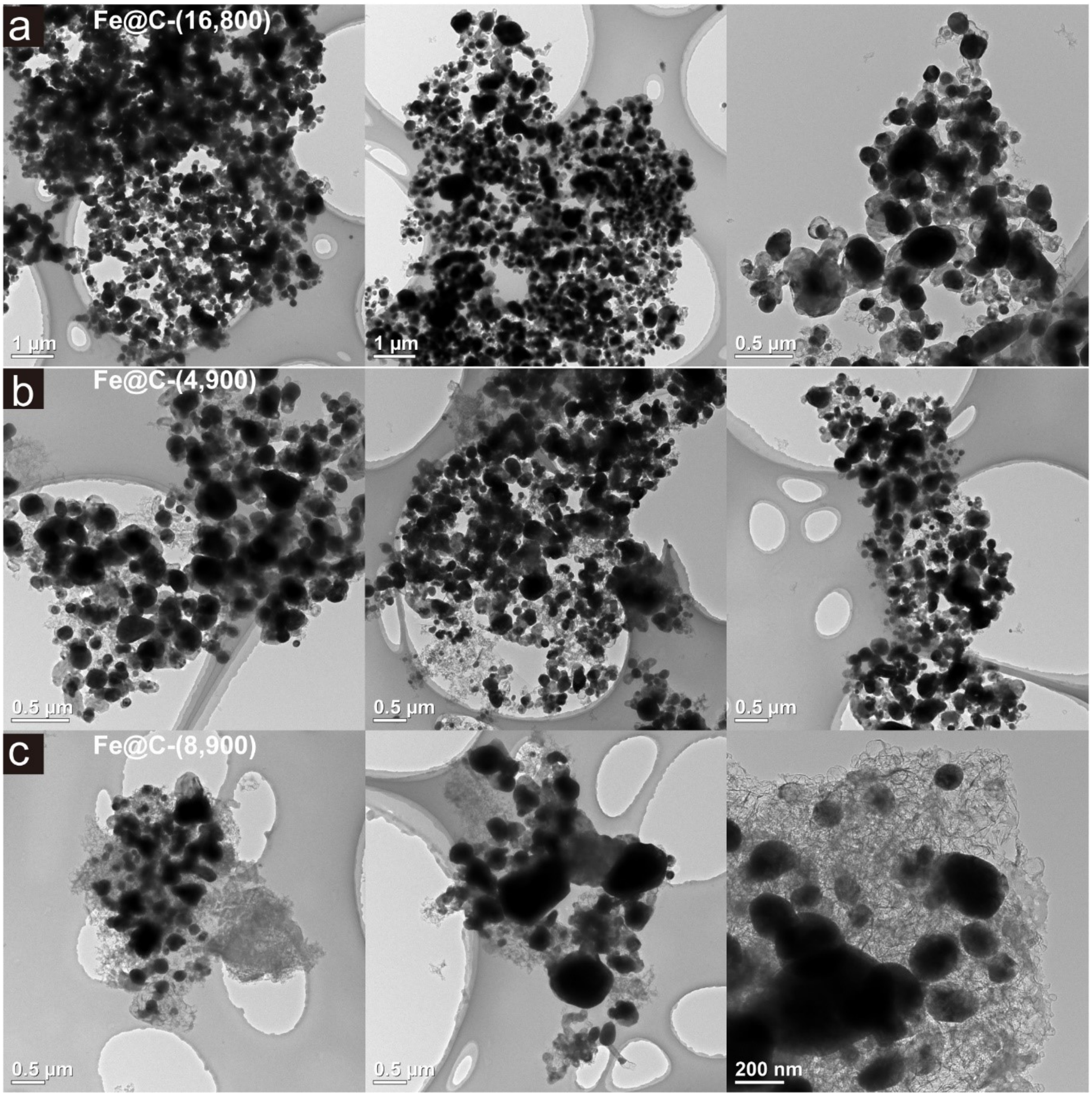

Fig. S12. TEM images of (a) Fe@C(16,800), (b) Fe@C(4,900), and (c) Fe@C(8,900) catalysts. Note that synthesized materials were presented in a Fe@C(x,y) manner, where x and y refer to the pyrolysis duration (in hours) and temperature (in °C), respectively. All materials exhibit high dispersion, the iron nanoparticles are well encased by a graphite-carbon shell with a porous structure, and the particle size increases with the calcination temperature and holding time.

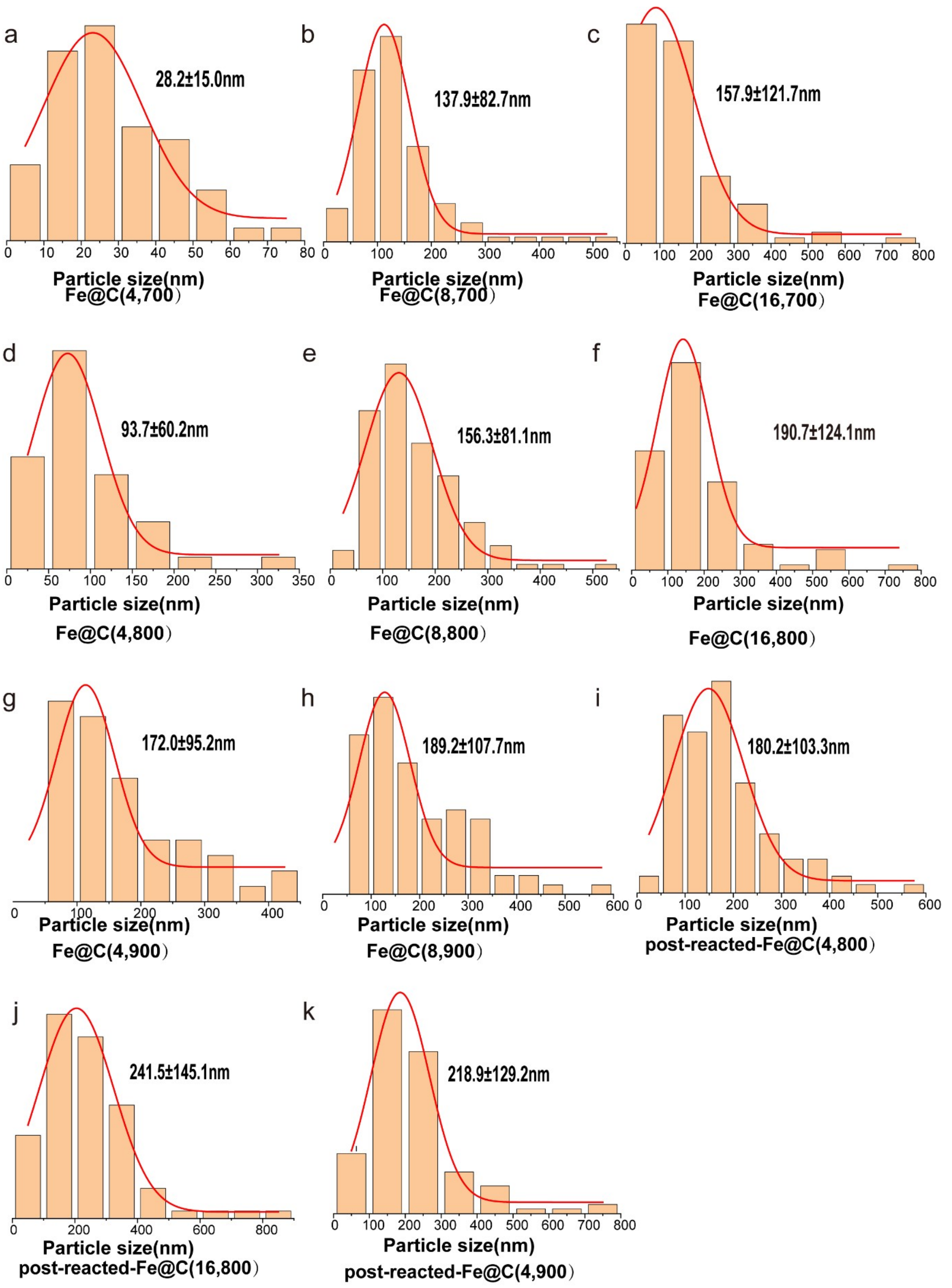

Fig. S13. Particle size distributions of (a) Fe@C(4,700), (b) Fe@C(8,700), (c) Fe@C(16,700), (d) Fe@C-(4,800), (e) Fe@C-(8,800), (f) Fe@C(16,800), (g) Fe@C(4,900), (h) Fe@C(8,900),

(i) post-reacted-Fe@C(4,800), (j) post-reacted-Fe@C(16,800), and (k) post-reacted-Fe@C(4,900) catalysts. The post-reacted catalysts were collected after 24-30 hours of reaction. Note that synthesized materials were presented in a Fe@C(x,y) manner, where x and y refer to the pyrolysis duration (in hours) and temperature (in °C), respectively. The size of Fe@C (4,800) increased from 93.7 nm to 180.2 nm before the reaction, and the grain size increased mainly due to the change to Fe_3O_4[11,12]. For Fe@C (16,800), the size of the reaction increased from 190.7 nm to 241.5 nm before the reaction, and the size of the (4,800) changed greatly Fe@C due to its thin and loose carbon layer and weak binding ability to iron metal. For the Fe@C(4,900) reaction, the size increased from 172.0 nm to 218.9 nm before the reaction, and the size also showed a large change in size. The results indicate that the graphitic carbon layer has a binding effect on controlling the increase of grain size.

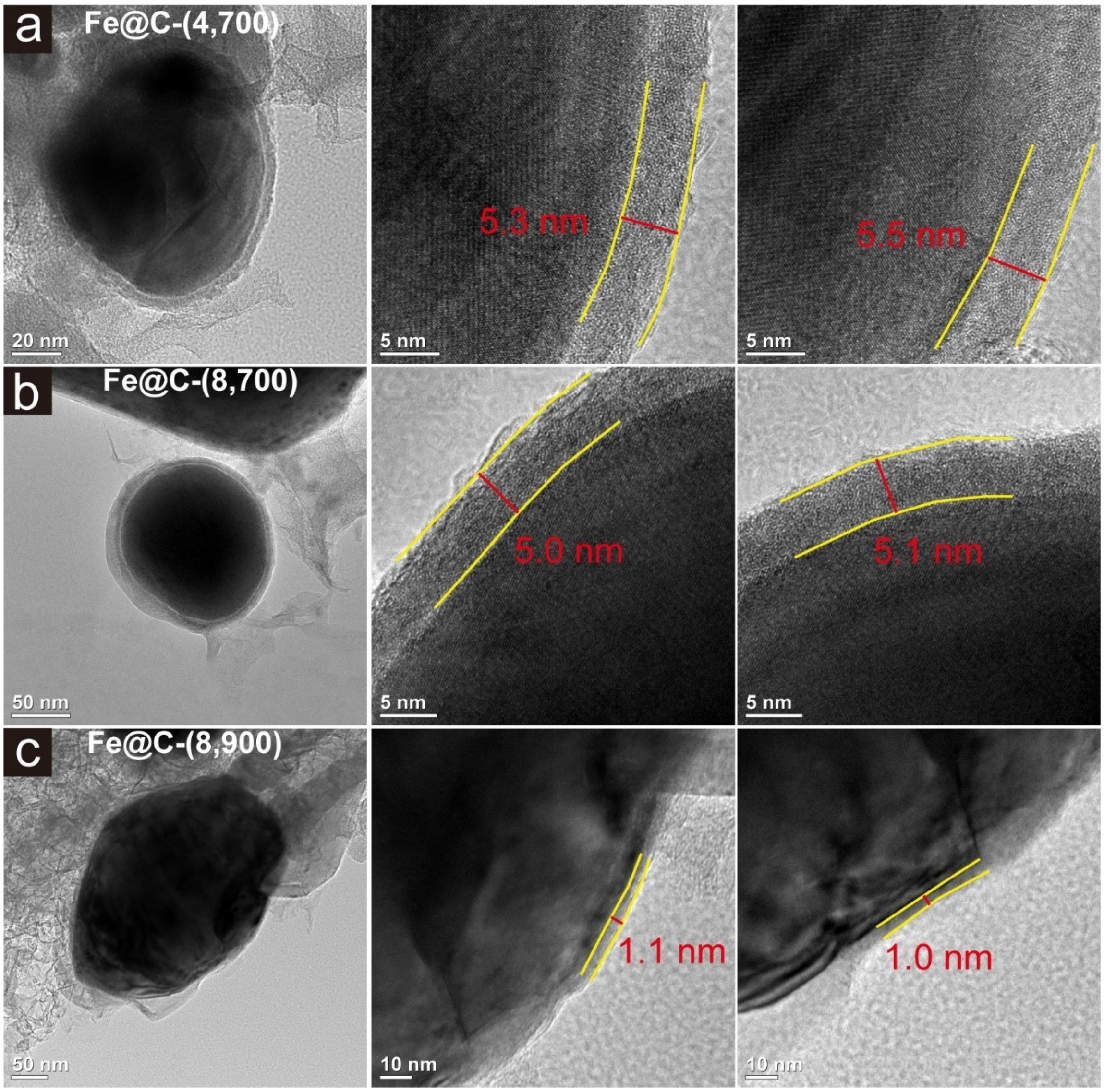

Fig. S14. TEM images of the (a) Fe@C(4,700), (b) Fe@C(8,700), and (c) Fe@C (8,900) catalysts. Note that synthesized materials were presented in a Fe@C(x,y) manner, where x and y refer to the pyrolysis duration (in hours) and temperature (in °C), respectively. With the increase of calcination temperature, the thickness of the carbon layer decreases, the defects increase, and the same phenomenon occurs for increasing the calcination holding time[12].

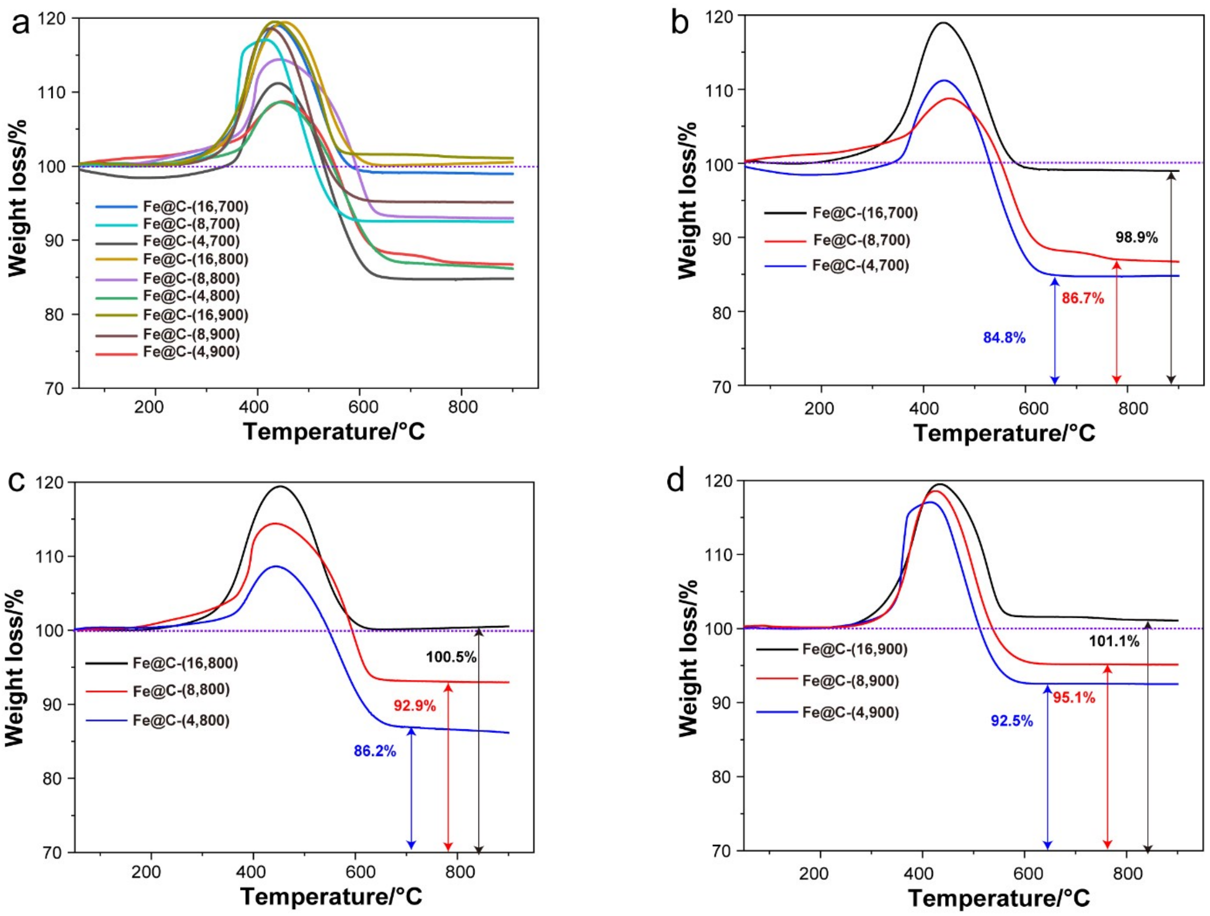

Fig. S15.TGA of the (a) Fe@C, (b) Fe@C-700, (c) Fe@C-800, and (d) Fe@C-900 catalysts. Note that synthesized materials were presented in a Fe@C(x,y) manner, where x and y refer to the pyrolysis duration (in hours) and temperature (in °C), respectively. The slight weight loss below 200 °C and the apparent weight loss above 200 °C are attributed to the evaporation of the adsorbed water and the combustion of the carbon matrix, respectively[12]. The weight gain zone in the TG curve is the process by which iron carbide is oxidized into iron oxide in air. As the calcination temperature increases, the total amount of carbon matrix in the Fe@C catalyst decreases slightly. As the calcination holding time increases, the total amount of carbon matrix in the Fe@C catalyst also decreases slightly. This is because high temperatures disrupt the continuous layered structure of graphite-carbon and introduce more defects[13].

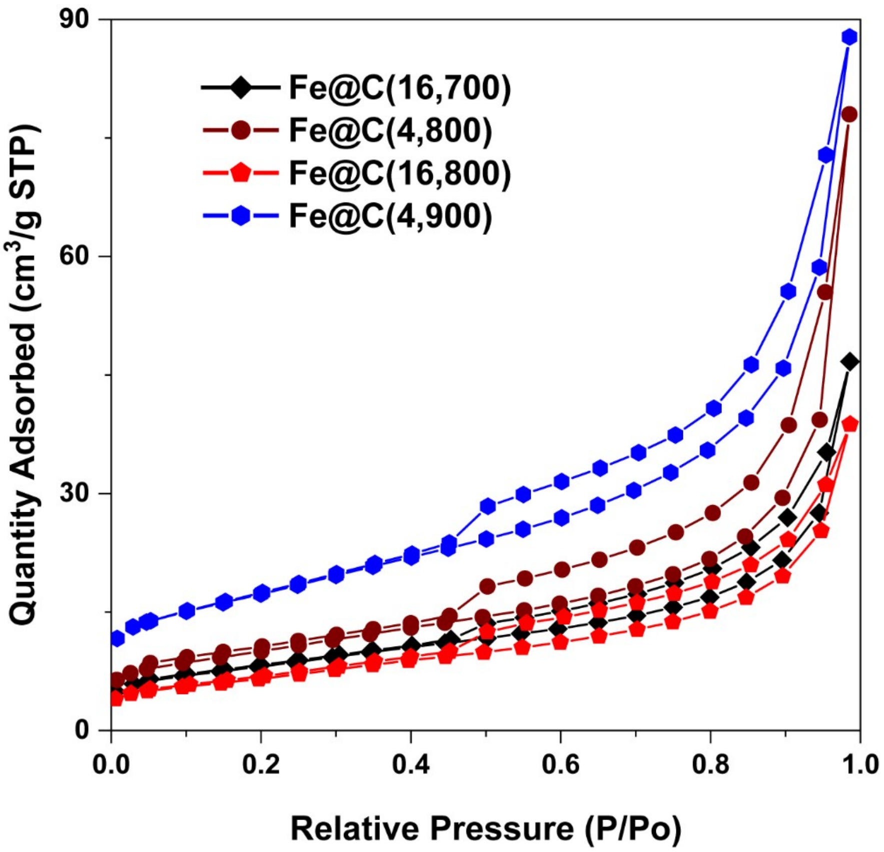

Fig. S16. Nitrogen adsorption/desorption isotherms of Fe@C(16,700), Fe@C(4,800), Fe@C(16,800), and Fe@C(4,900) catalysts. Note that synthesized materials were presented in a Fe@C(x,y) manner, where x and y refer to the pyrolysis duration (in hours) and temperature (in °C), respectively. Mesopores formed on fresh FeC are highly ordered mesoporous structures with type IV isotherms and H_2 hysteresis. This phenomenon is mainly due to the highly porous carbon layer encapsulated with metallic iron nanoparticles[14,15]. The higher the calcination temperature, the shorter the holding time, and the more obvious the isothermal adsorption curve.

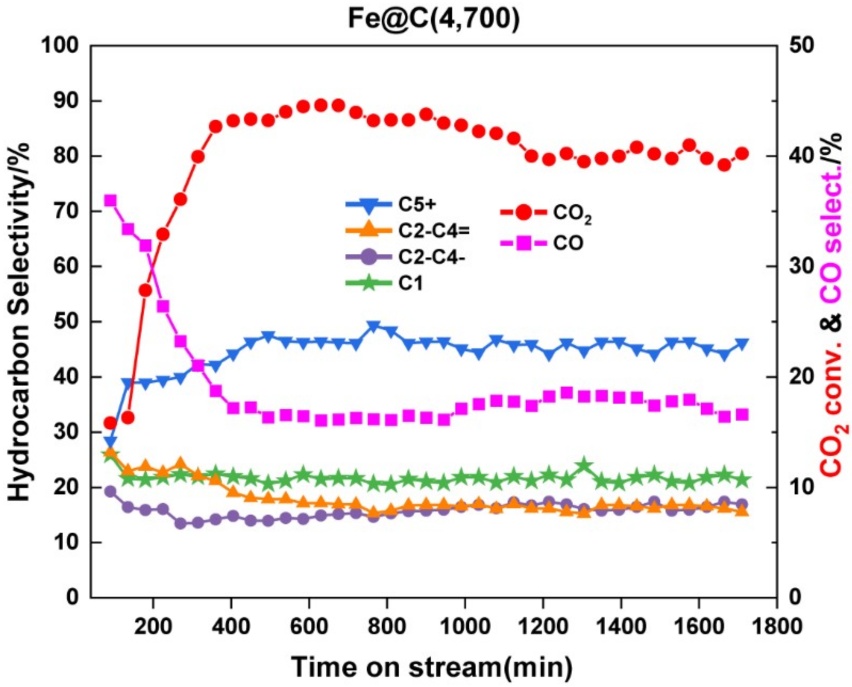

Fig. S17. Catalytic performance data of the Fe@C(4,700) catalysts with respect to time-on-stream (in min) [Reaction conditions: $H_2/CO_2 = 3$, 350 °C, 3 MPa, 4800 mL g^{-1} h^{-1}].

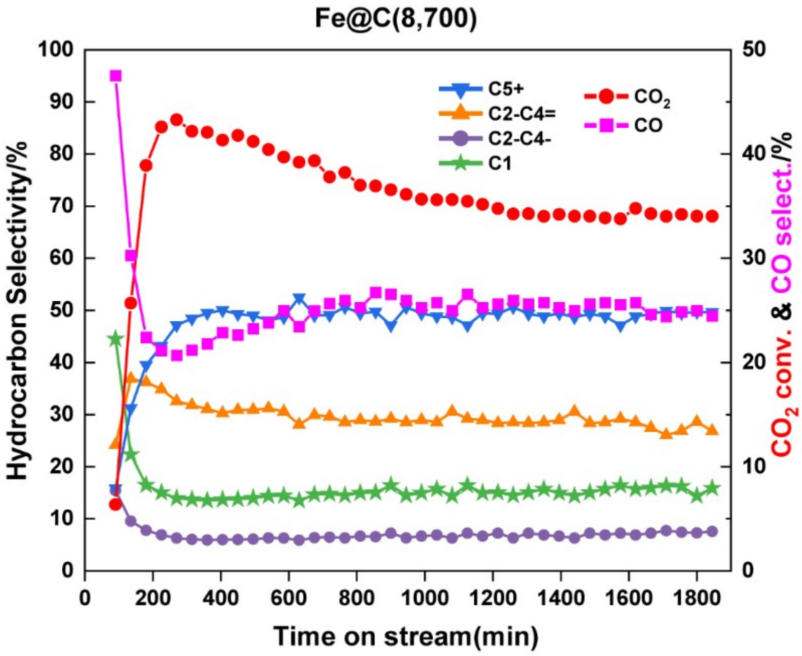

Fig. S18. Catalytic performance data of the Fe@C(8,700) catalysts with respect to time-on-stream (in min) [Reaction conditions: $H_2/CO_2 = 3$, 350 °C, 3 MPa, 4800 mL g^{-1} h^{-1}].

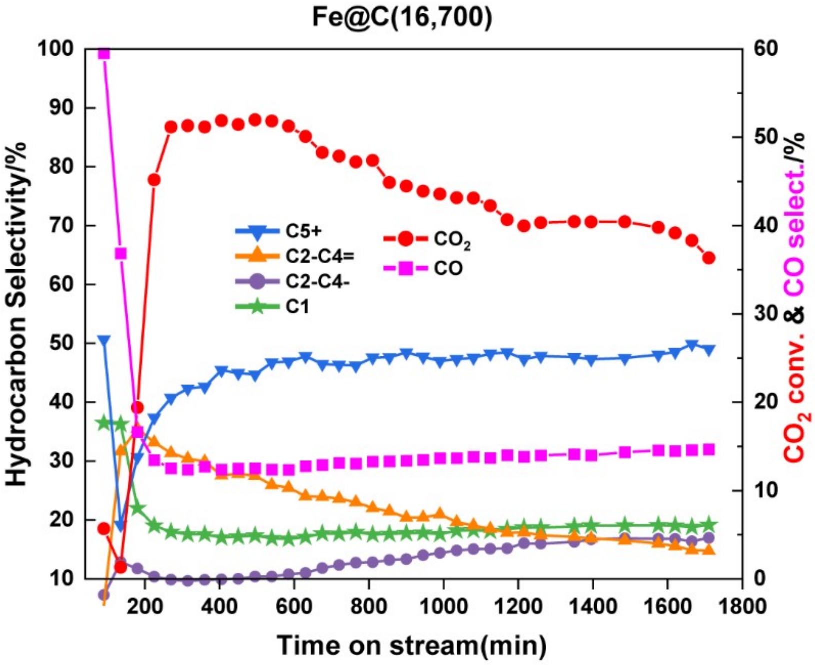

Fig. S19. Catalytic performance data of the Fe@C(16,700) catalysts with respect to time-on-stream (in min) [Reaction conditions: $H_2/CO_2 = 3$, 350 °C, 3 MPa, 4800 mL g^{-1} h^{-1}].

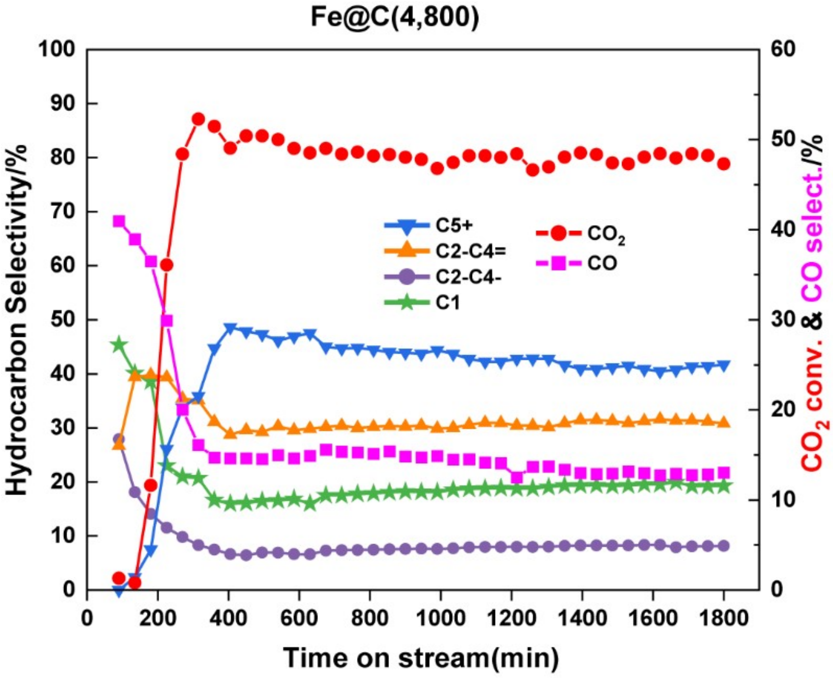

Fig. S20. Catalytic performance data of the Fe@C(4,800) catalysts with respect to time-on-stream (in min) [Reaction conditions: $H_2/CO_2 = 3$, 350 °C, 3 MPa, 4800 mL g^{-1} h^{-1}].

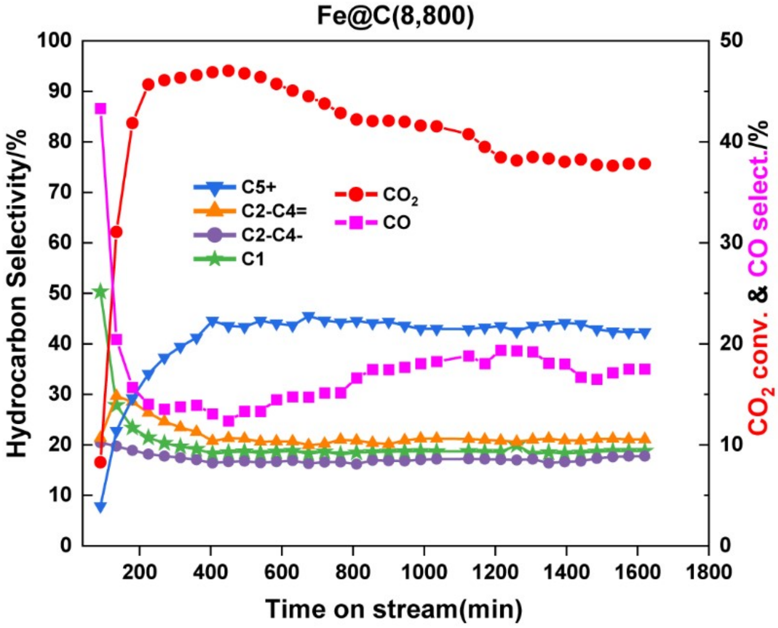

Fig. S21. Catalytic performance data of the Fe@C(8,800) catalysts with respect to time-on-stream (in min) [Reaction conditions: $H_2/CO_2 = 3$, 350 °C, 3 MPa, 4800 mL g^{-1} h^{-1}].

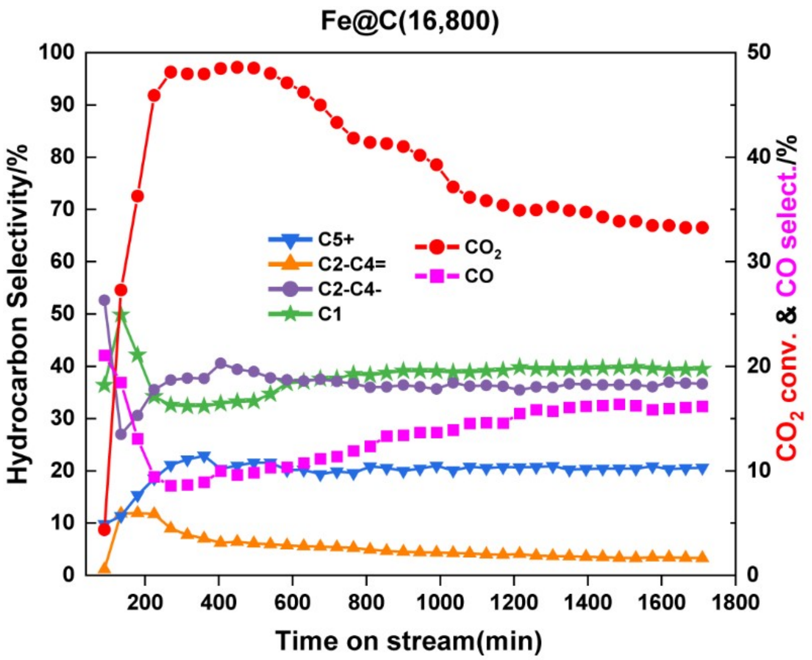

Fig. S22. Catalytic performance data of the Fe@C(16,800) catalysts with respect to time-on-stream (in min) [Reaction conditions: $H_2/CO_2 = 3$, 350 °C, 3 MPa, 4800 mL g^{-1} h^{-1}].

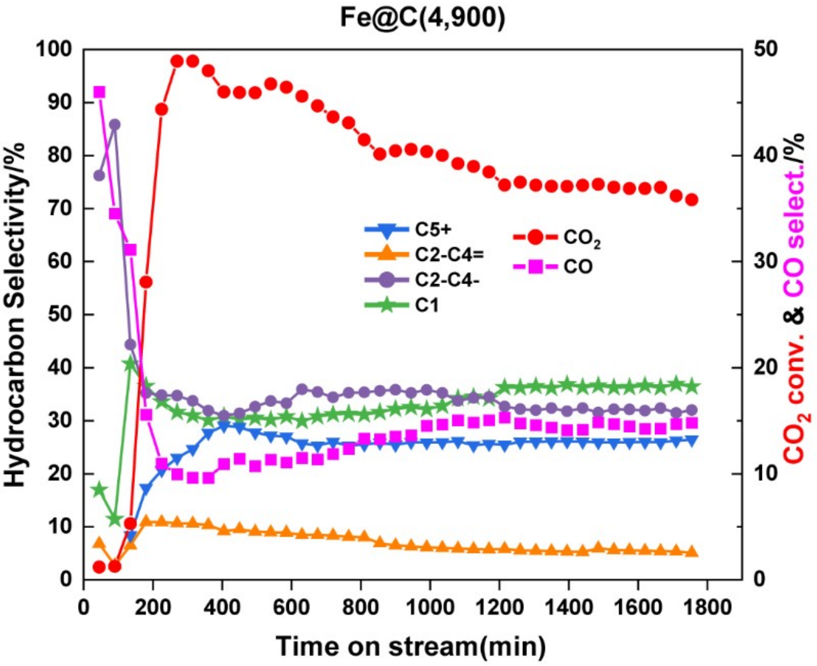

Fig. S23. Catalytic performance data of the Fe@C(4,900) catalysts with respect to time-on-stream (in min) [Reaction conditions: $H_2/CO_2 = 3$, 350 °C, 3 MPa, 4800 mL g^{-1} h^{-1}].

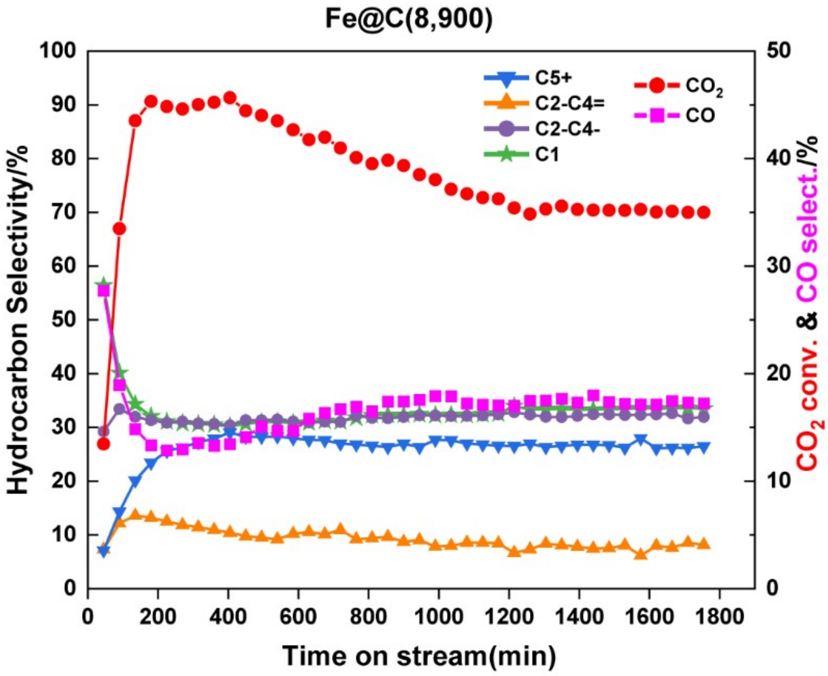

Fig. S24. Catalytic performance data of the Fe@C(8,900) catalysts with respect to time-on-stream (in min) [Reaction conditions: $H_2/CO_2 = 3$, 350 °C, 3 MPa, 4800 mL g^{-1} h^{-1}].

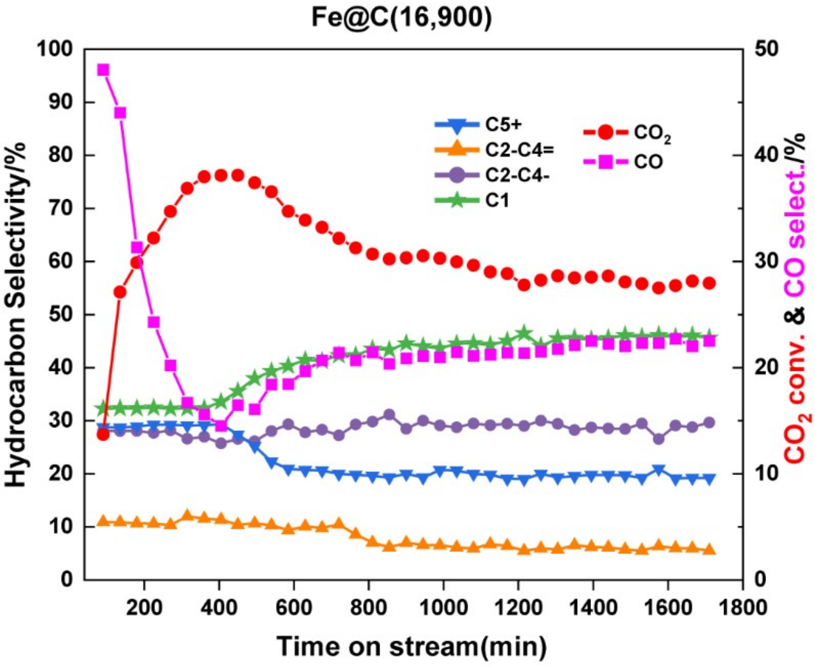

Fig. S25. Catalytic performance data of the Fe@C(16,900) catalysts with respect to time-on-stream (in min) [Reaction conditions: $H_2/CO_2 = 3$, 350 °C, 3 MPa, 4800 mL g^{-1} h^{-1}].

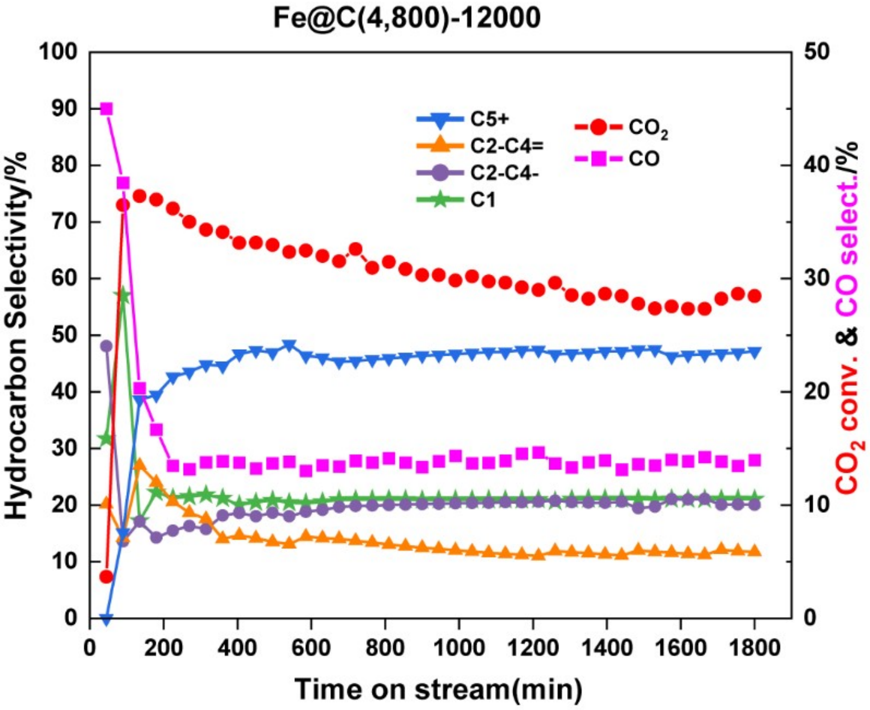

Fig. S26. Catalytic performance data of the Fe@C(4,800) catalysts with respect to time-on-stream (in min) at higher GHSV [Reaction conditions: $H_2/CO_2 = 3$, 350 °C, 3 MPa, 12000 mL g^{-1} h^{-1}].

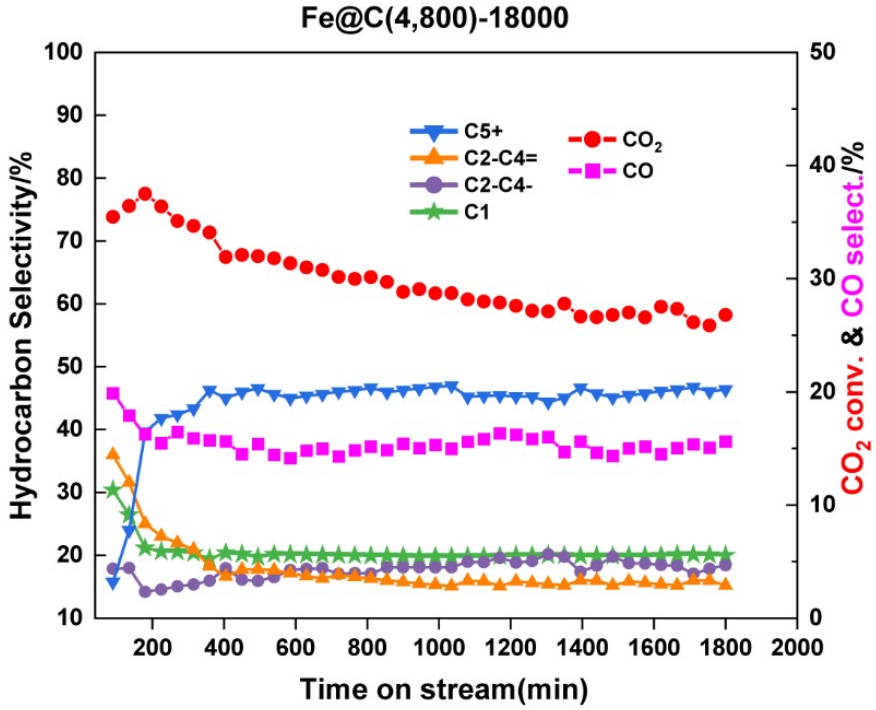

Fig. S27. Catalytic performance data of the Fe@C(4,800) catalysts with respect to time-on-stream (in min) at higher GHSV [Reaction conditions: $H_2/CO_2 = 3$, 350 °C, 3 MPa, 18000 mL g^{-1} h^{-1}].

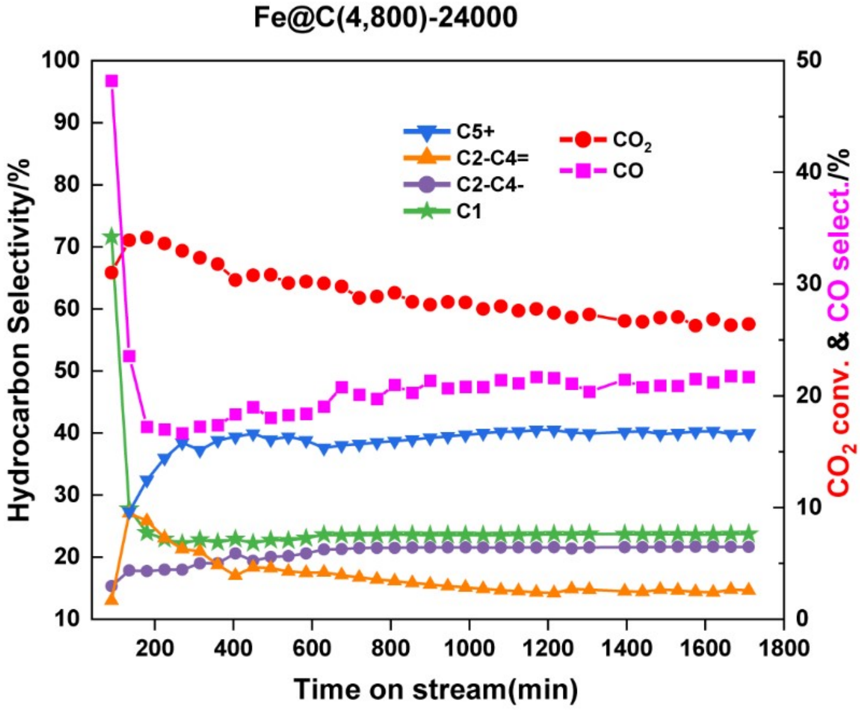

Fig. S28. Catalytic performance data of the Fe@C(4,800) catalysts with respect to time-on-stream (in min) at higher GHSV [Reaction conditions: $H_2/CO_2 = 3$, 350 °C, 3 MPa, 24000 mL g^{-1} h^{-1}].

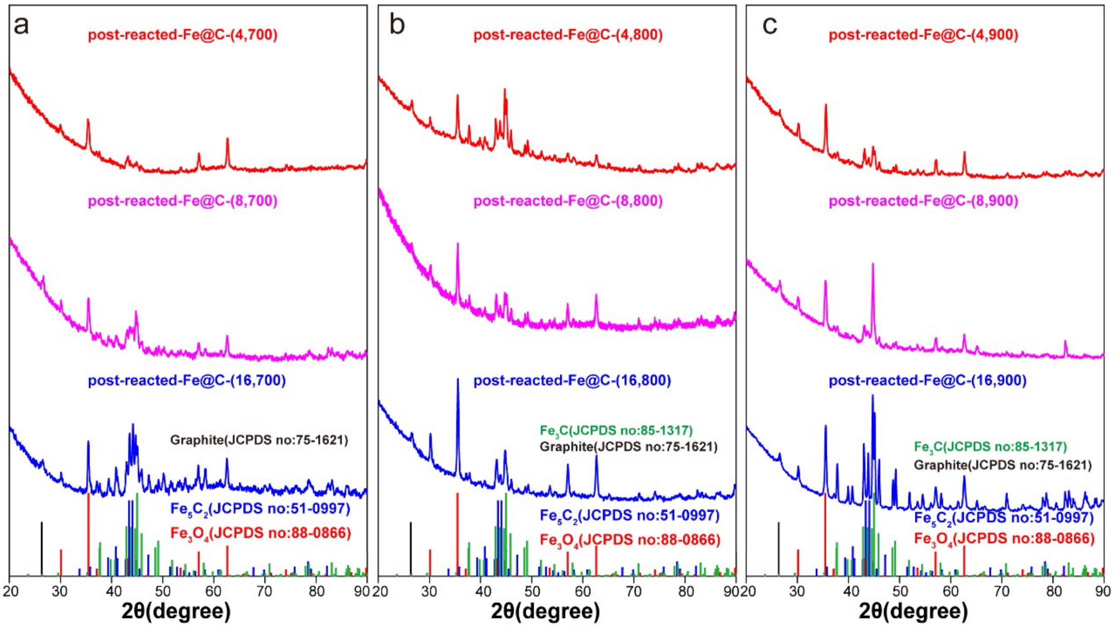

Fig. S29. XRD patterns of post-reacted (a) Fe@C-700, (b) Fe@C-800, and (c) Fe@C-900 catalysts. Note that synthesized materials were presented in a Fe@C(x,y) manner, where x and y refer to the pyrolysis duration (in hours) and temperature (in °C), respectively. All catalysts with high C_{5+} hydrocarbon selectivity, such as Fe@C(4,700), Fe@C(8,700), Fe@C(16,700), Fe@C(4,800), and Fe@C(8,800), exhibit a prominent Fe_5C_2 phase with a less distinct Fe_3O_4 phase. In contrast, catalysts favoring methane and C_2-C_4 alkanes, such as Fe@C(16,800), Fe@C(4,900), Fe@C(8,900), and Fe@C(16,900), show a weaker Fe_5C_2 phase and more prominent Fe_3C and Fe_3O_4 phases.

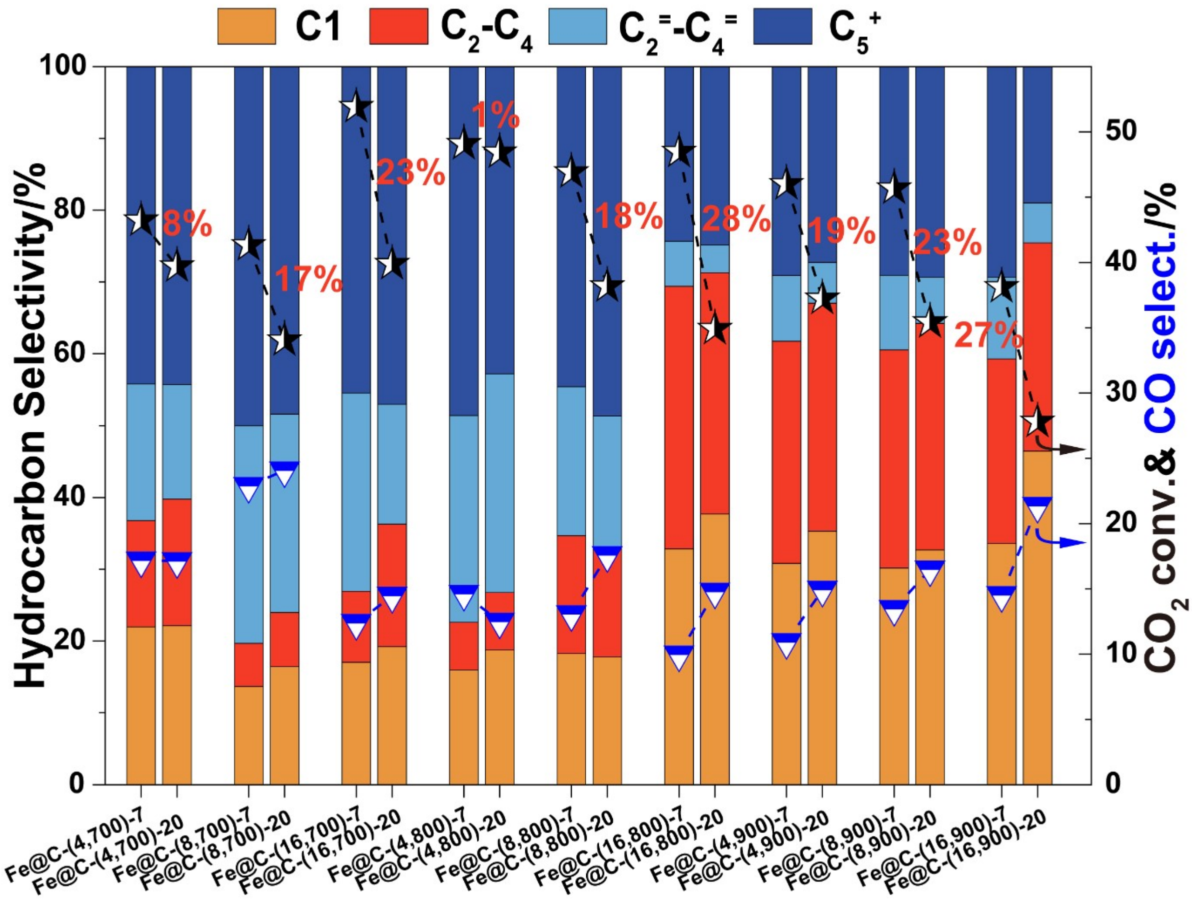

Fig. S30. Catalytic performance data of the Fe@C catalysts with time-on-stream at ~7h and ~20h. [Reaction conditions: $H_2/CO_2 = 3$, 350 °C, 3 MPa, 4800 mL h^{-1}]. Notes: catalyst deactivation=1-CO_2 conversion at TOS 20h/ CO_2 conversion at TOS 7h. Also note that synthesized materials were presented in a Fe@C(x,y) manner, where x and y refer to the pyrolysis duration (in hours) and temperature (in °C), respectively.

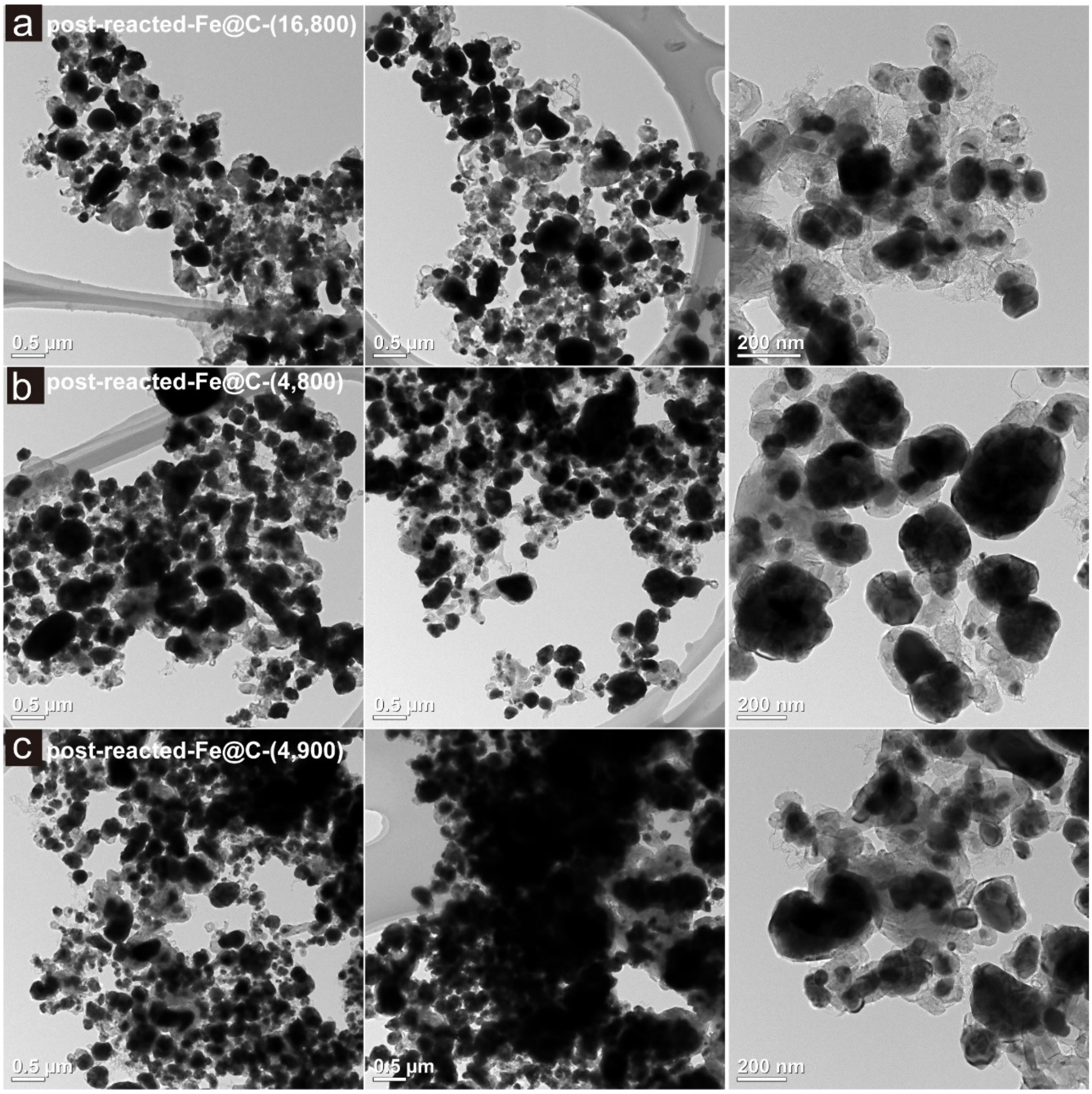

Fig. S31. TEM images of post-reacted (a) Fe@C(16,800), (b) Fe@C(4,800), and (c) Fe@C(4,900) catalysts. Note that synthesized materials were presented in a Fe@C(x,y) manner, where x and y refer to the pyrol1ysis duration (in hours) and temperature (in °C), respectively. The size of post-reacted Fe@C (16,800), Fe@C (4,800), and Fe@C (4,900) were increased, and the grain size increased mainly due to the change to Fe_3O_4[11,12]. For Fe@C (16,800) and Fe@C(4,800) materials, after the reaction, the catalyst maintains high dispersion, and its graphitic carbon layer is relatively dense, which is conducive to the catalyst to maintain high dispersion. However, for Fe@C(4,900) material, the graphite-carbon layer is loose and weakly binds iron particles, and the catalyst aggregates after the reaction.

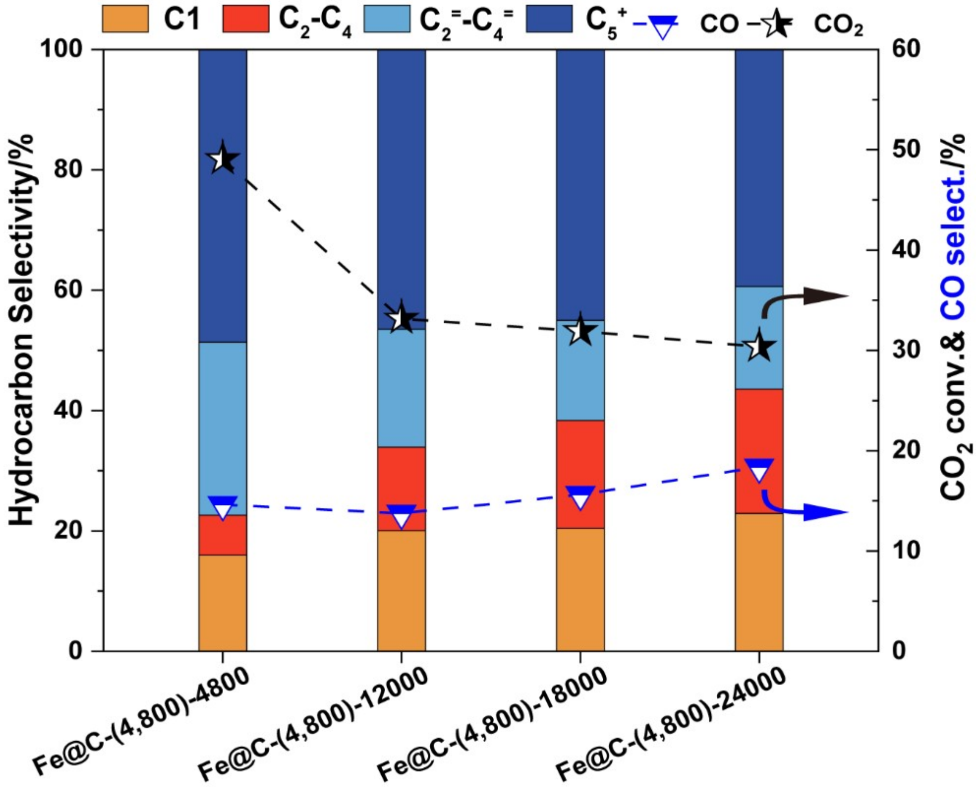

Fig. S32. Catalytic performance data of the Fe@C(4,800) catalysts with time-on-stream at 7h with different GHSV [Reaction conditions: $H_2/CO_2 = 3$, 350 °C, 3 MPa]. Note that synthesized materials were presented in a Fe@C(x,y) manner, where x and y refer to the pyrolysis duration (in hours) and temperature (in °C), respectively.

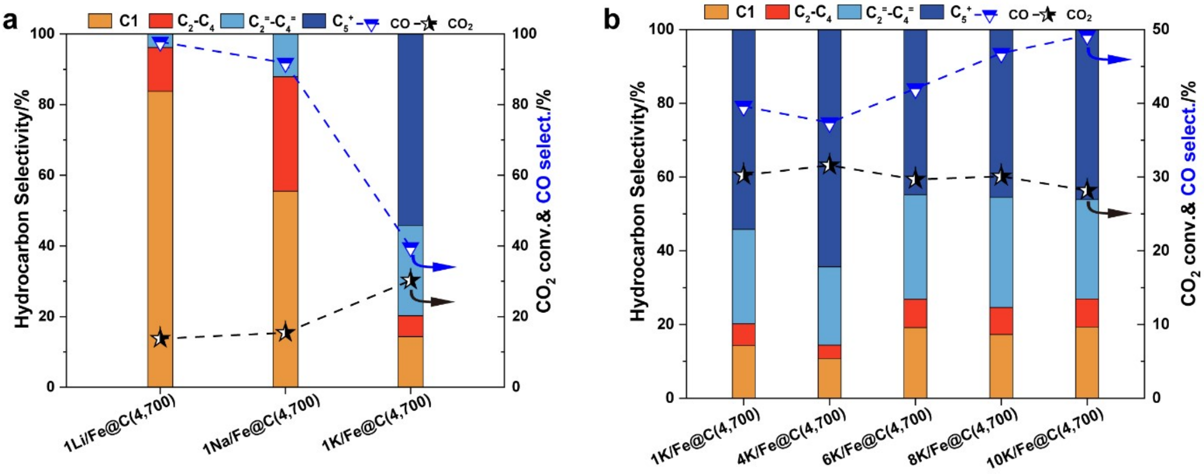

Fig. S33. Catalytic performance data of (a) Li or Na or K-promoted Fe@C(4,700) catalysts, (b) Fe@C(4,700) catalysts with time-on-stream at 7h with different K loading. [Reaction conditions: $H_2/CO_2 = 3$, 350 °C, 3 MPa, 18000 $mLg^{-1}h^{-1}$]. Note that synthesized materials were presented in a Fe@C(x,y) manner, where x and y refer to the pyrolysis duration (in hours) and temperature (in °C), respectively.

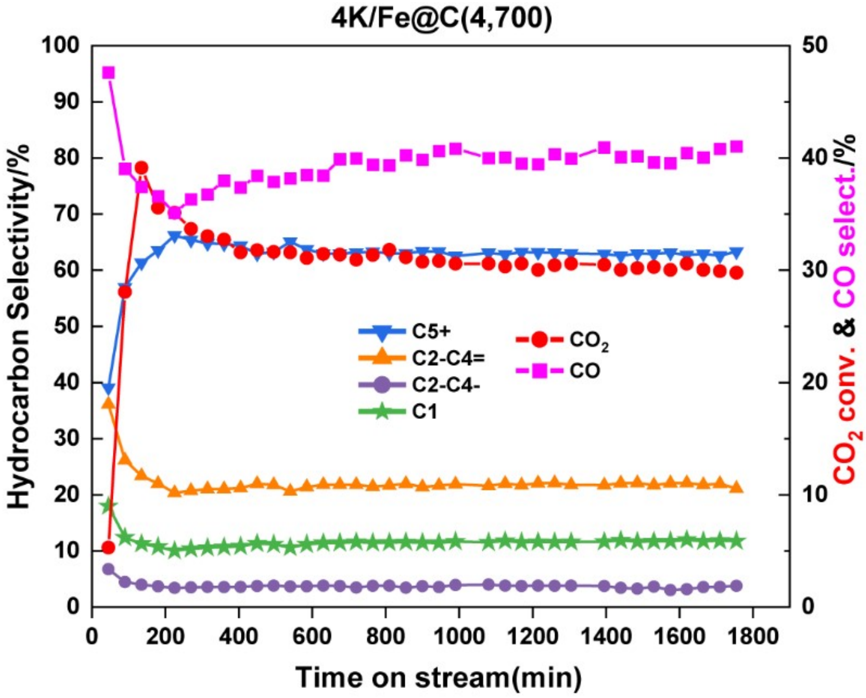

Fig. S34. Catalytic performance data of the 4K/Fe@C(4,700) catalysts with respect to time-on-stream (in min) [Reaction conditions: $H_2/CO_2 = 3$, 350 °C, 3 MPa, 18000 mL g^{-1} h^{-1}].

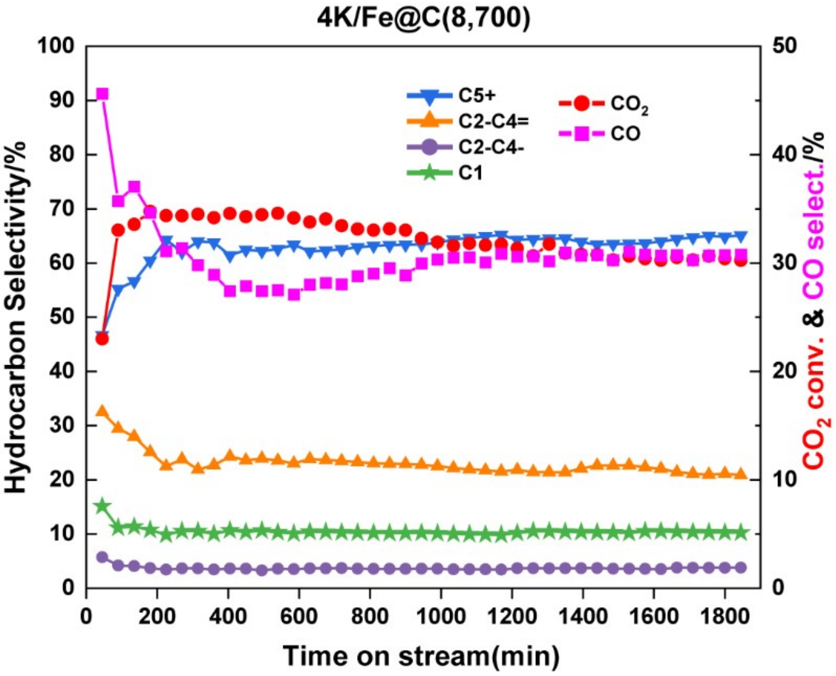

Fig. S35. Catalytic performance data of the 4K/Fe@C(8,700) catalysts with respect to time-on-stream (in min) [Reaction conditions: $H_2/CO_2 = 3$, 350 °C, 3 MPa, 18000 mL g^{-1} h^{-1}].

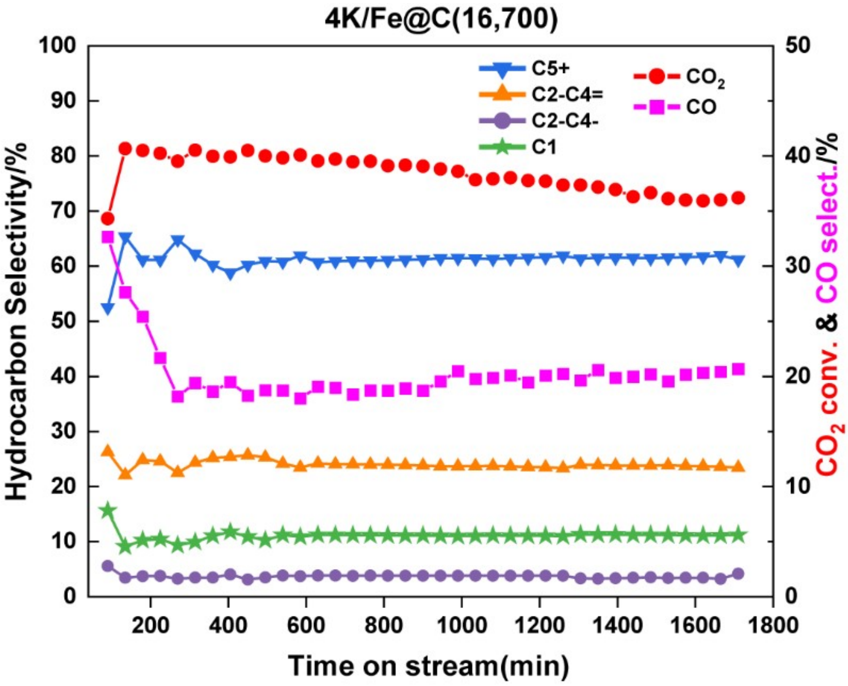

Fig. S36. Catalytic performance data of the 4K/Fe@C(16,700) catalysts with respect to time-on-stream (in min) [Reaction conditions: $H_2/CO_2 = 3$, 350 °C, 3 MPa, 18000 mL g^{-1} h^{-1}].

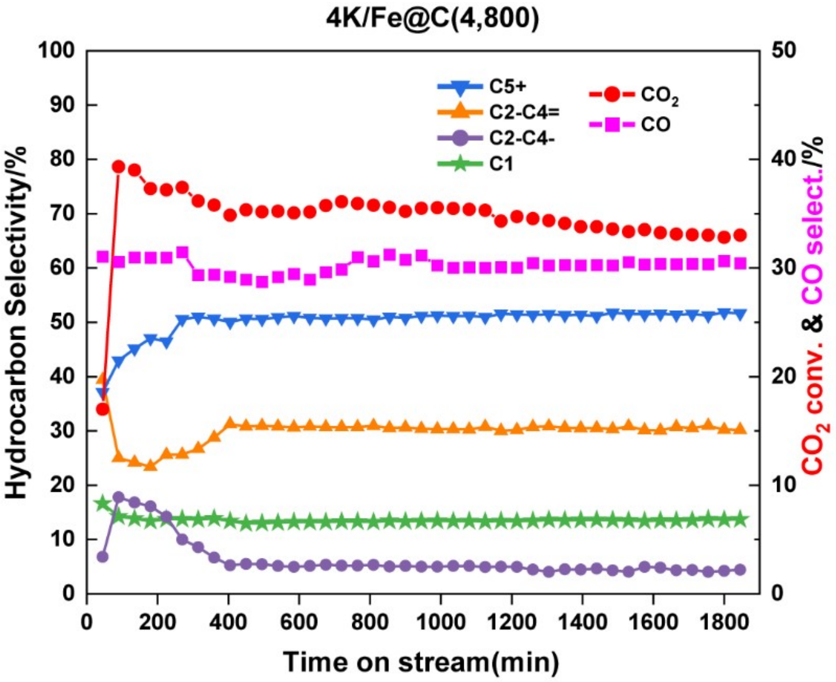

Fig. S37. Catalytic performance data of the 4K/Fe@C(4,800) catalysts with respect to time-on-stream (in min) [Reaction conditions: $H_2/CO_2 = 3$, 350 °C, 3 MPa, 18000 mL g^{-1} h^{-1}].

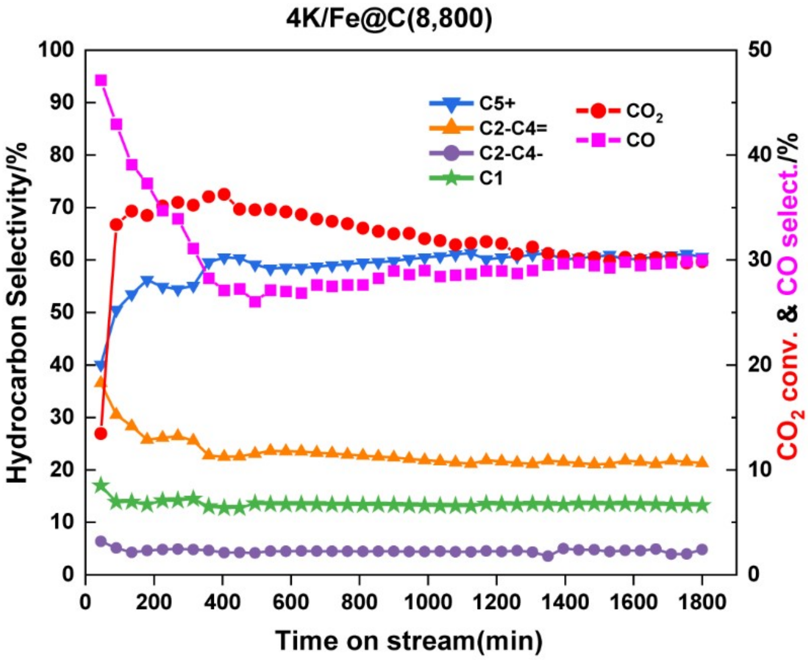

Fig. S38. Catalytic performance data of the 4K/Fe@C(8,800) catalysts with respect to time-on-stream (in min) [Reaction conditions: $H_2/CO_2 = 3$, 350 °C, 3 MPa, 18000 mL g^{-1} h^{-1}].

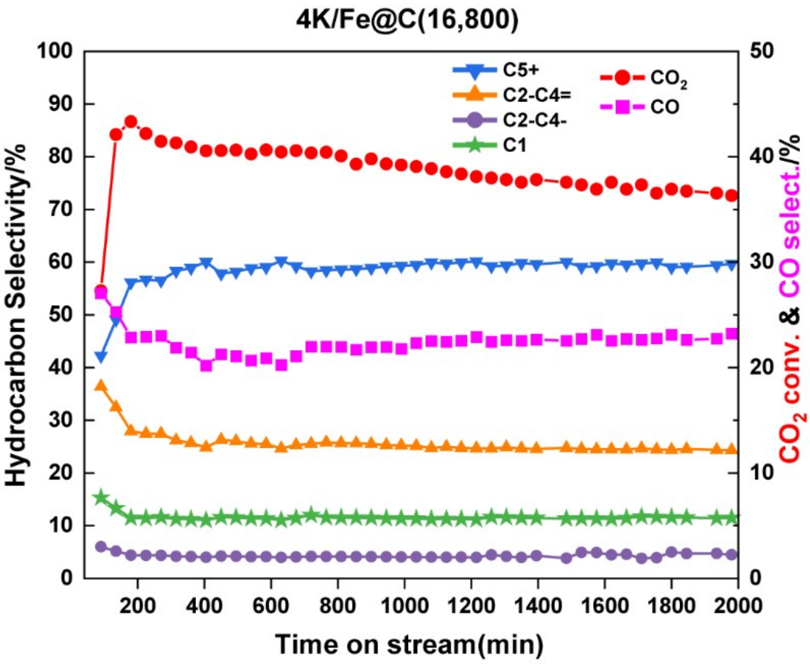

Fig. S39. Catalytic performance data of the 4K/Fe@C(16,800) catalysts with respect to time-on-stream (in min) [Reaction conditions: $H_2/CO_2 = 3$, 350 °C, 3 MPa, 18000 mL g^{-1} h^{-1}].

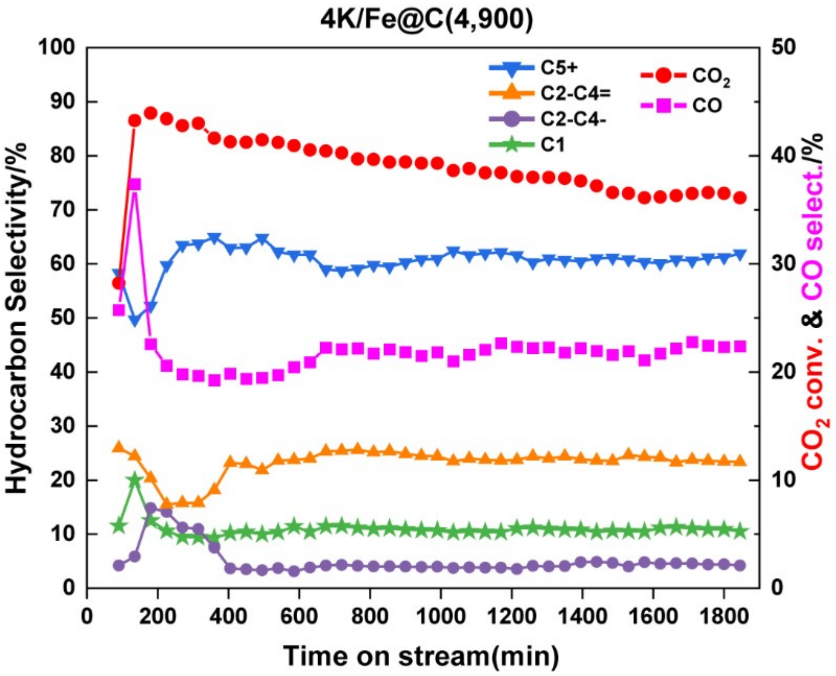

Fig. S40. Catalytic performance data of the 4K/Fe@C(4,900) catalysts with respect to time-on-stream (in min) [Reaction conditions: $H_2/CO_2 = 3$, 350 °C, 3 MPa, 18000 mL g^{-1} h^{-1}].

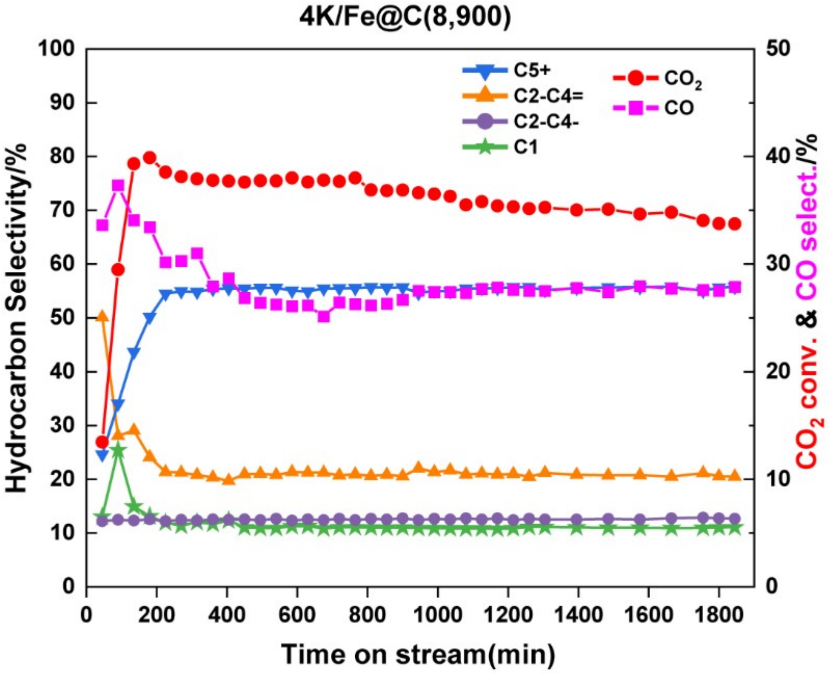

Fig. S41. Catalytic performance data of the 4K/Fe@C(8,900) catalysts with respect to time-on-stream (in min) [Reaction conditions: $H_2/CO_2 = 3$, 350 °C, 3 MPa, 18000 mL g^{-1} h^{-1}].

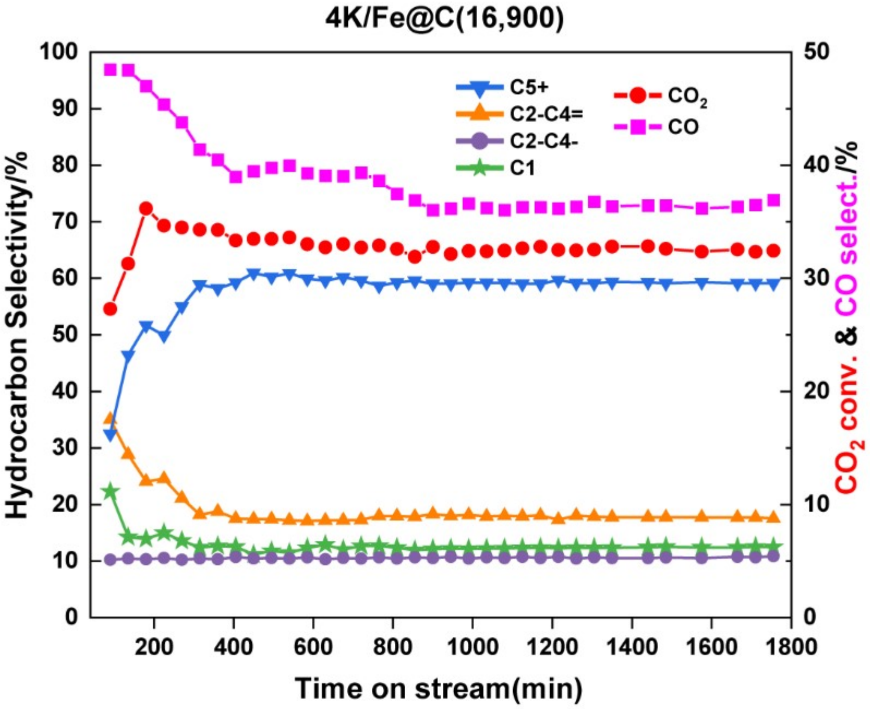

Fig. S42. Catalytic performance data of the 4K/Fe@C(16,900) catalysts with respect to time-on-stream (in min) [Reaction conditions: $H_2/CO_2 = 3$, 350 °C, 3 MPa, 18000 mL g^{-1} h^{-1}].

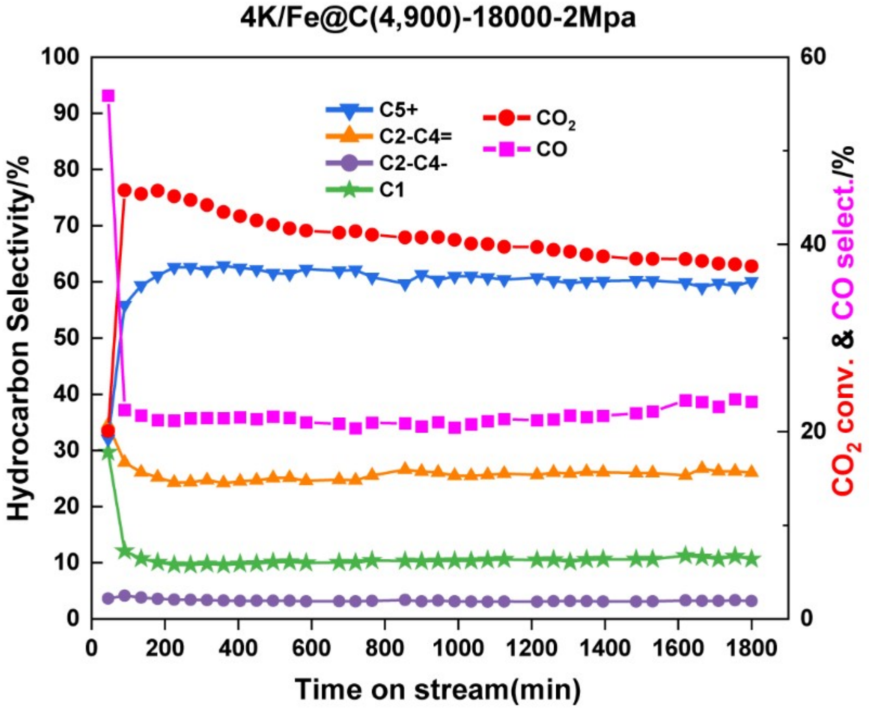

Fig. S43. Catalytic performance data of the 4K/Fe@C(4,900) catalysts with respect to time-on-stream (in min) [Reaction conditions: $H_2/CO_2 = 3$, 350 °C, 2 MPa, 18000 mL g^{-1} h^{-1}].

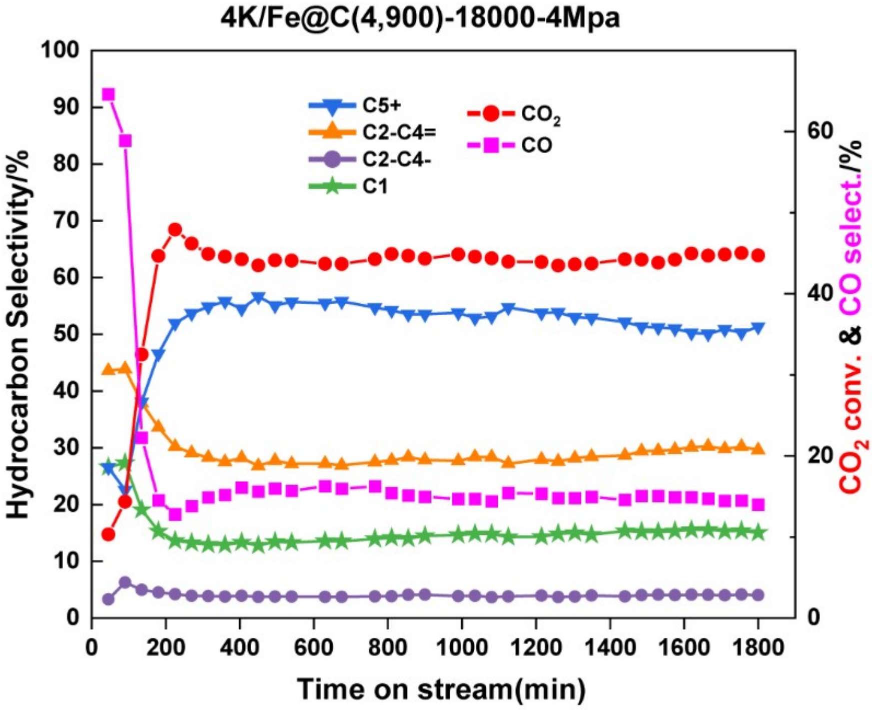

Fig. S44. Catalytic performance data of the 4K/Fe@C(4,900) catalysts with respect to time-on-stream (in min) [Reaction conditions: $H_2/CO_2 = 3$, 350 °C, 4 MPa, 18000 mL g^{-1} h^{-1}].

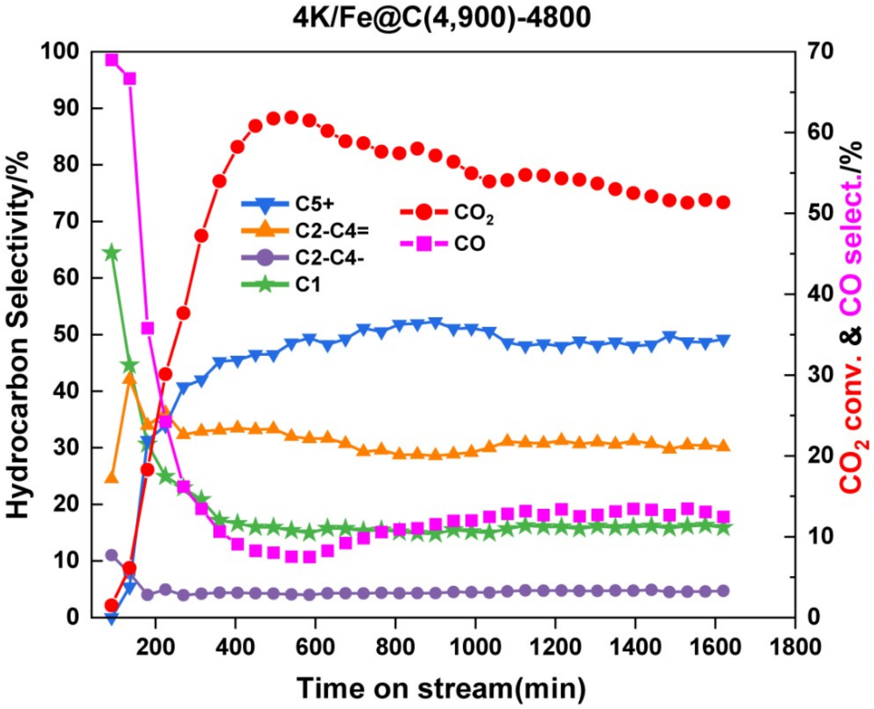

Fig. S45. Catalytic performance data of the 4K/Fe@C(4,900) catalysts with respect to time-on-stream (in min) [Reaction conditions: $H_2/CO_2 = 3$, 350 °C, 3 MPa, 4800 mL g^{-1} h^{-1}].

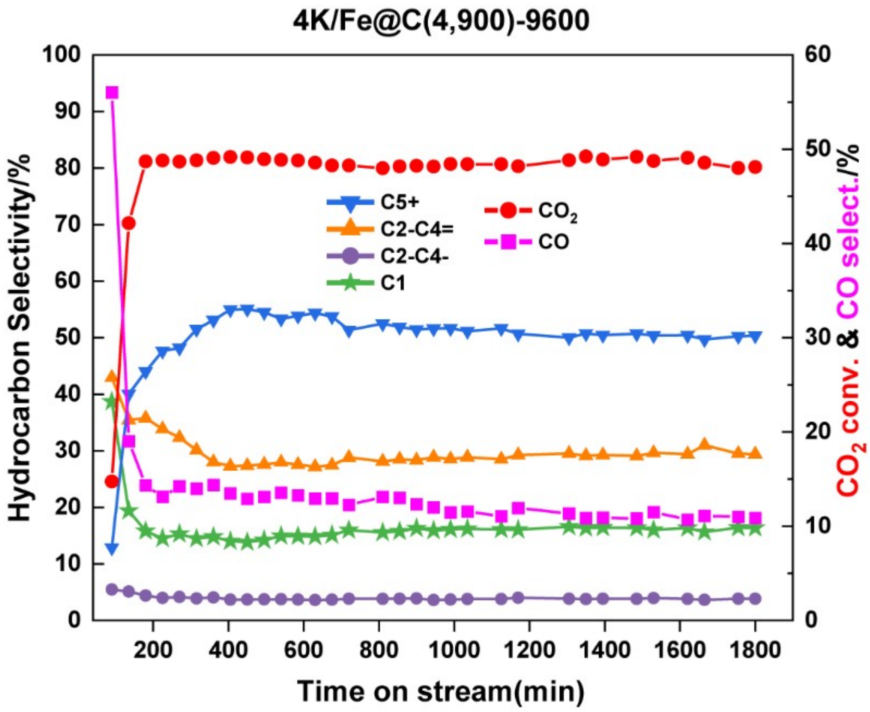

Fig. S46. Catalytic performance data of the 4K/Fe@C(4,900) catalysts with respect to time-on-stream (in min) [Reaction conditions: $H_2/CO_2 = 3$, 350 °C, 3 MPa, 9600 mL g^{-1} h^{-1}].

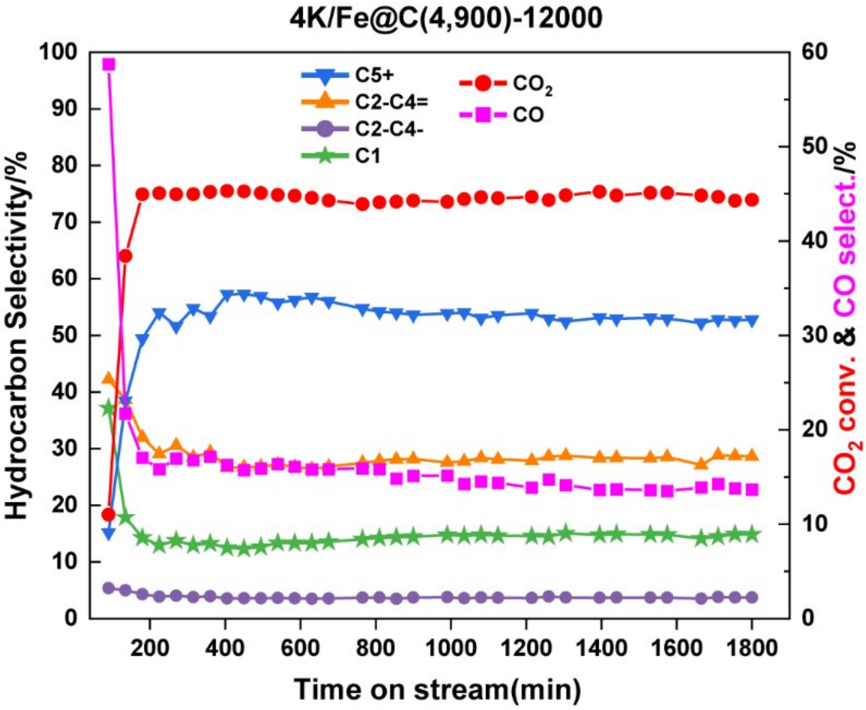

Fig. S47. Catalytic performance data of the 4K/Fe@C(4,900) catalysts with respect to time-on-stream (in min) [Reaction conditions: $H_2/CO_2 = 3$, 350 °C, 3 MPa, 12000 mL g^{-1} h^{-1}].

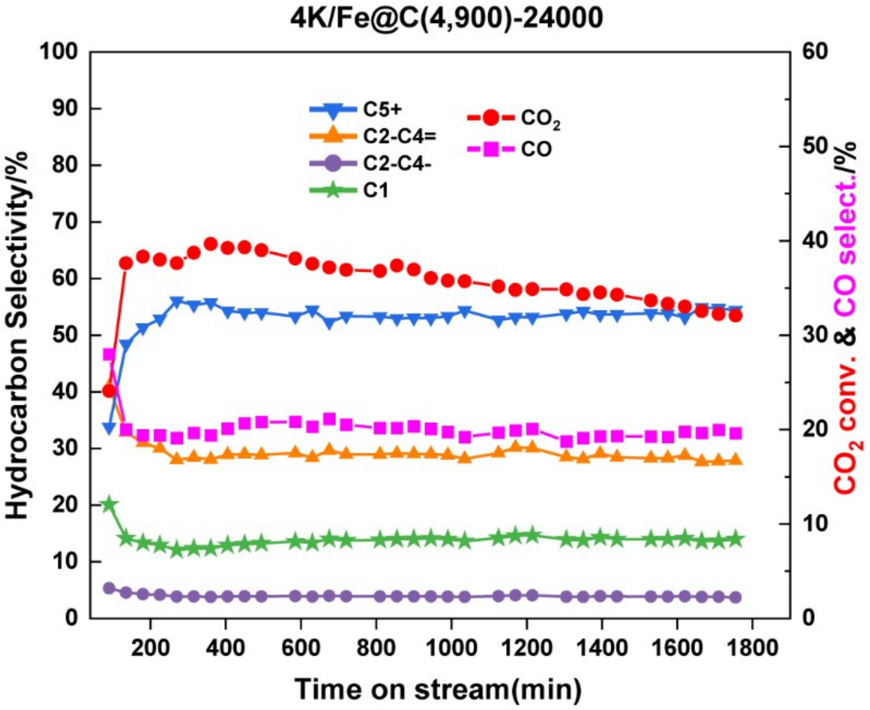

Fig. S48. Catalytic performance data of the 4K/Fe@C(4,900) catalysts with respect to time-on-stream (in min) [Reaction conditions: $H_2/CO_2 = 3$, 350 °C, 3 MPa, 24000 mL g^{-1} h^{-1}].

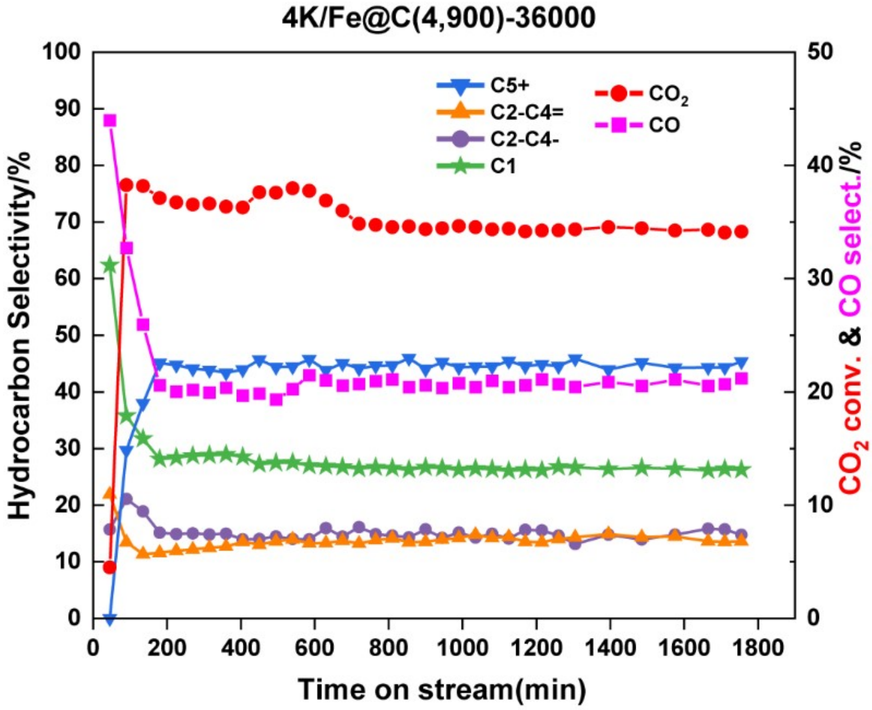

Fig. S49. Catalytic performance data of the 4K/Fe@C(4,900) catalysts with respect to time-on-stream (in min) at higher GHSV [Reaction conditions: $H_2/CO_2 = 3$, 350 °C, 3 MPa, 36000 mL g^{-1} h^{-1}].

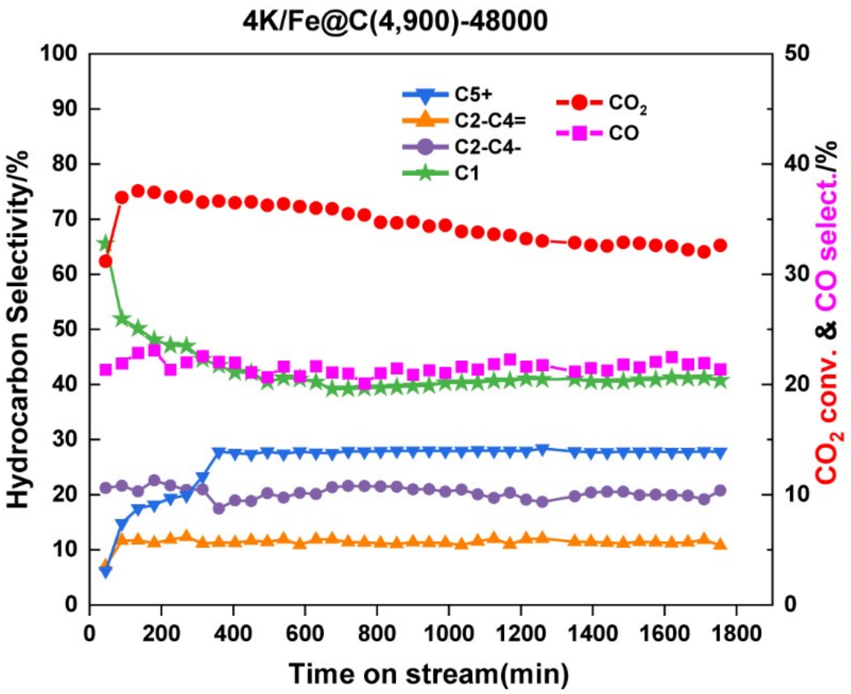

Fig. S50. Catalytic performance data of the 4K/Fe@C(4,900) catalysts with respect to time-on-stream (in min) at higher GHSV [Reaction conditions: $H_2/CO_2 = 3$, 350 °C, 3 MPa, 48000 mL g^{-1} h^{-1}].

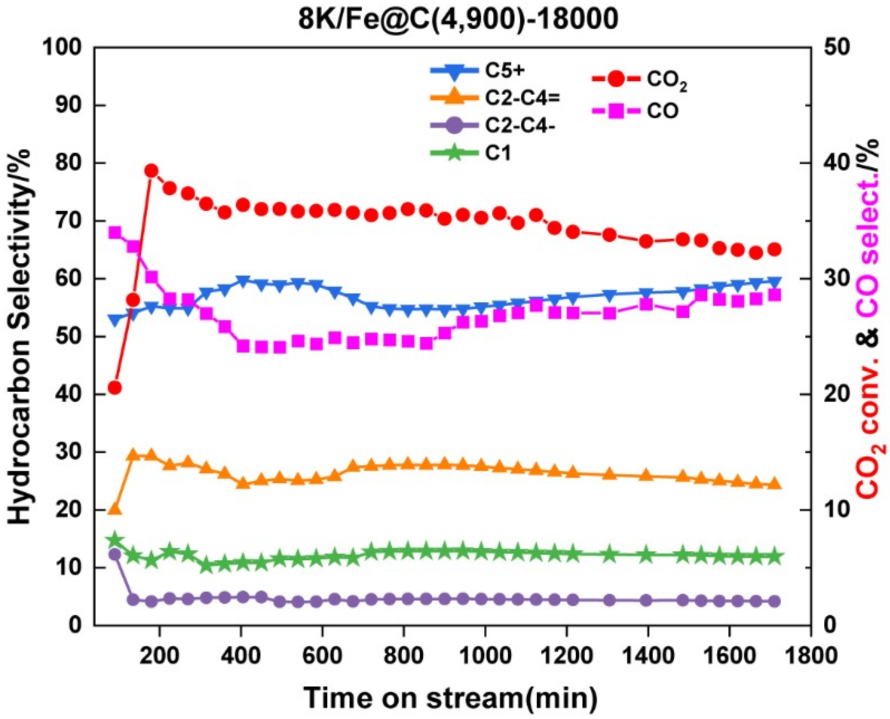

Fig. S51. Catalytic performance data of the 8K/Fe@C(4,900) catalysts with respect to time-on-stream (in min) [Reaction conditions: $H_2/CO_2 = 3$, 350 °C, 3 MPa, 18000 mL g^{-1} h^{-1}].

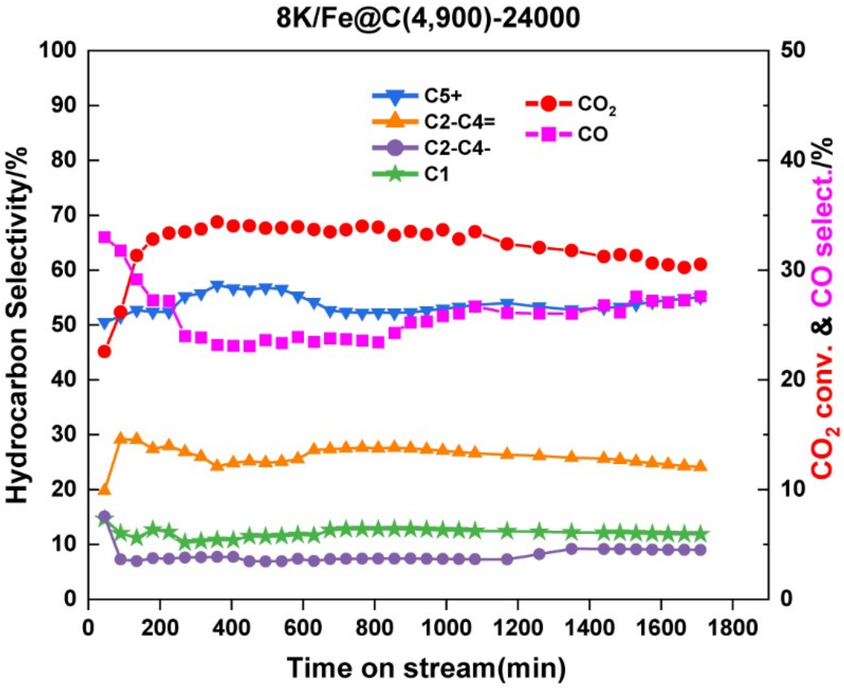

Fig. S52. Catalytic performance data of the 8K/Fe@C(4,900) catalysts with respect to time-on-stream (in min) at higher GHSV [Reaction conditions: $H_2/CO_2 = 3$, 350 °C, 3 MPa, 24000 mL g^{-1} h^{-1}].

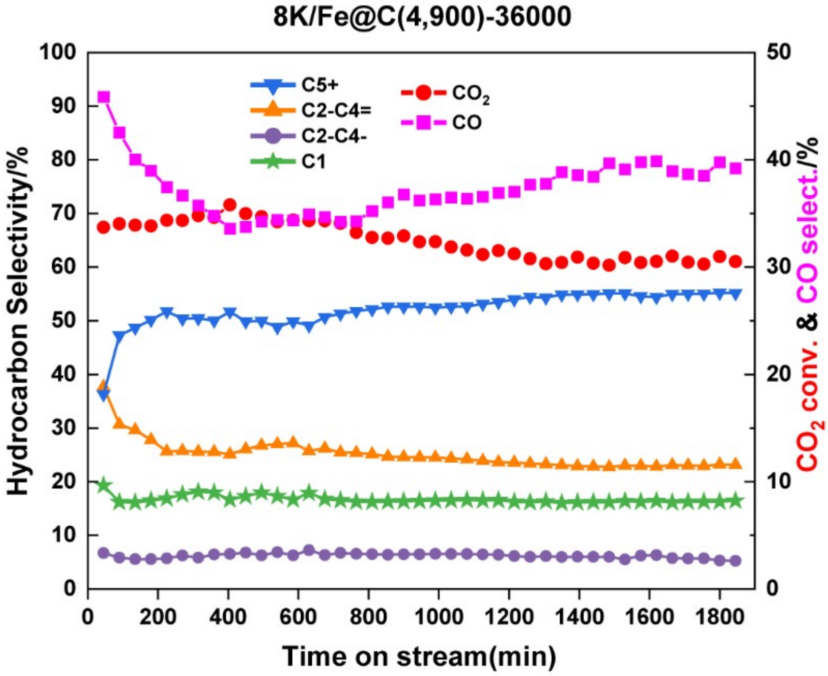

Fig. S53. Catalytic performance data of the 8K/Fe@C(4,900) catalysts with respect to time-on-stream (in min) at higher GHSV [Reaction conditions: $H_2/CO_2 = 3$, 350 °C, 3 MPa, 36000 mL g^{-1} h^{-1}].

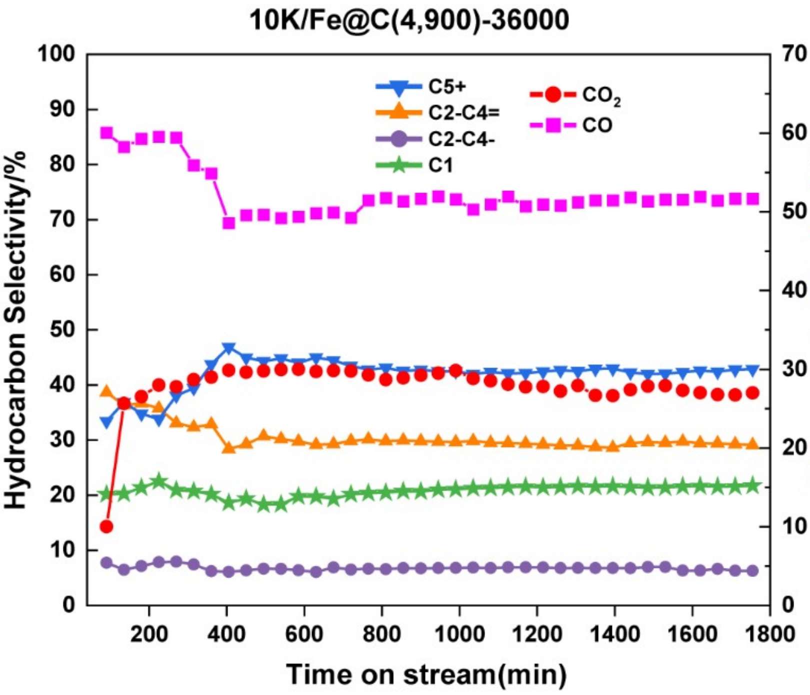

Fig. S54. Catalytic performance data of the 10K/Fe@C(4,900) catalysts with respect to time-on-stream (in min) [Reaction conditions: $H_2/CO_2 = 3$, 350 °C, 3 MPa, 36000 mL g^{-1} h^{-1}].

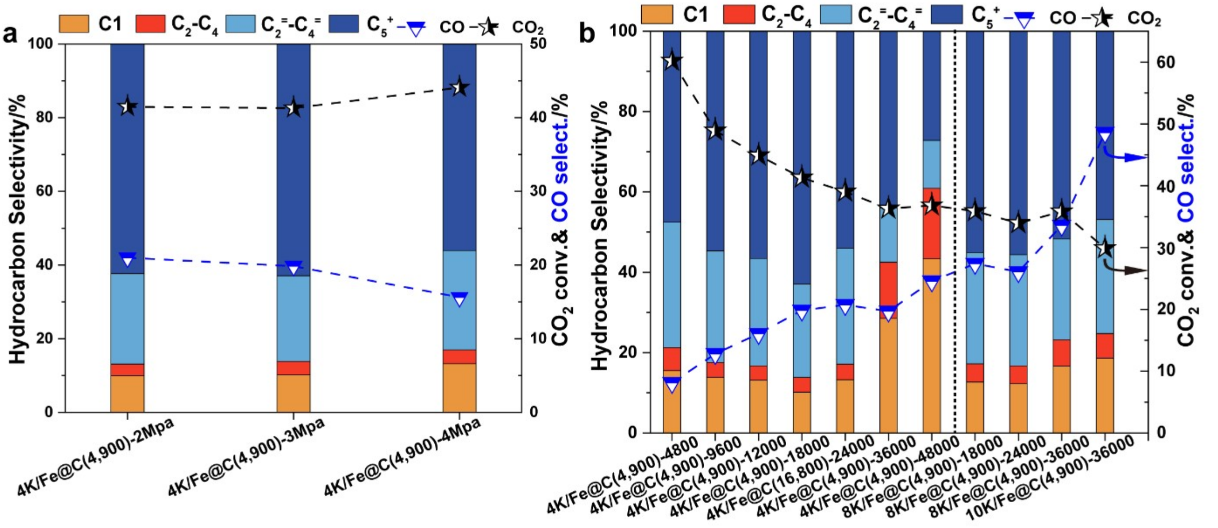

Fig. S55. Catalytic performance data of the K/Fe@C catalysts with time-on-stream at 7h at (a) different pressure [Reaction conditions: $H_2/CO_2 = 3$, 350 °C, 18000 mL g^{-1} h^{-1}], (b) different GHSVs [Reaction conditions: $H_2/CO_2 = 3$, 350 °C, 3 MPa]. Note that synthesized materials were presented in a Fe@C(x,y) manner, where x and y refer to the pyrolysis duration (in hours) and temperature (in °C), respectively. For the 4K/Fe@C (4,900) catalyst, the CO_2 conversion and CH_4 selectivity increased with the increase of pressure, while the selectivity of CO decreased. For the 4K/Fe@C (4,900) catalyst, the CO_2 conversion and C_{5+} selectivity decreased with the increase of GHSVs, while the selectivity of CO, CH_4, and C2-C4 alkanes increased. For 8K/Fe@C(4,900) catalysts, increasing the K content, C_{5+} selectivity increases even at high GSHVs of 36000 $mLg^{-1}h^{-1}$. Still, its CO selectivity rises, and excess K will mask the active site, resulting in a decrease in activity; at 10K/Fe@C(4,900) catalyst is more pronounced. The CO selectivity is close to 50%.

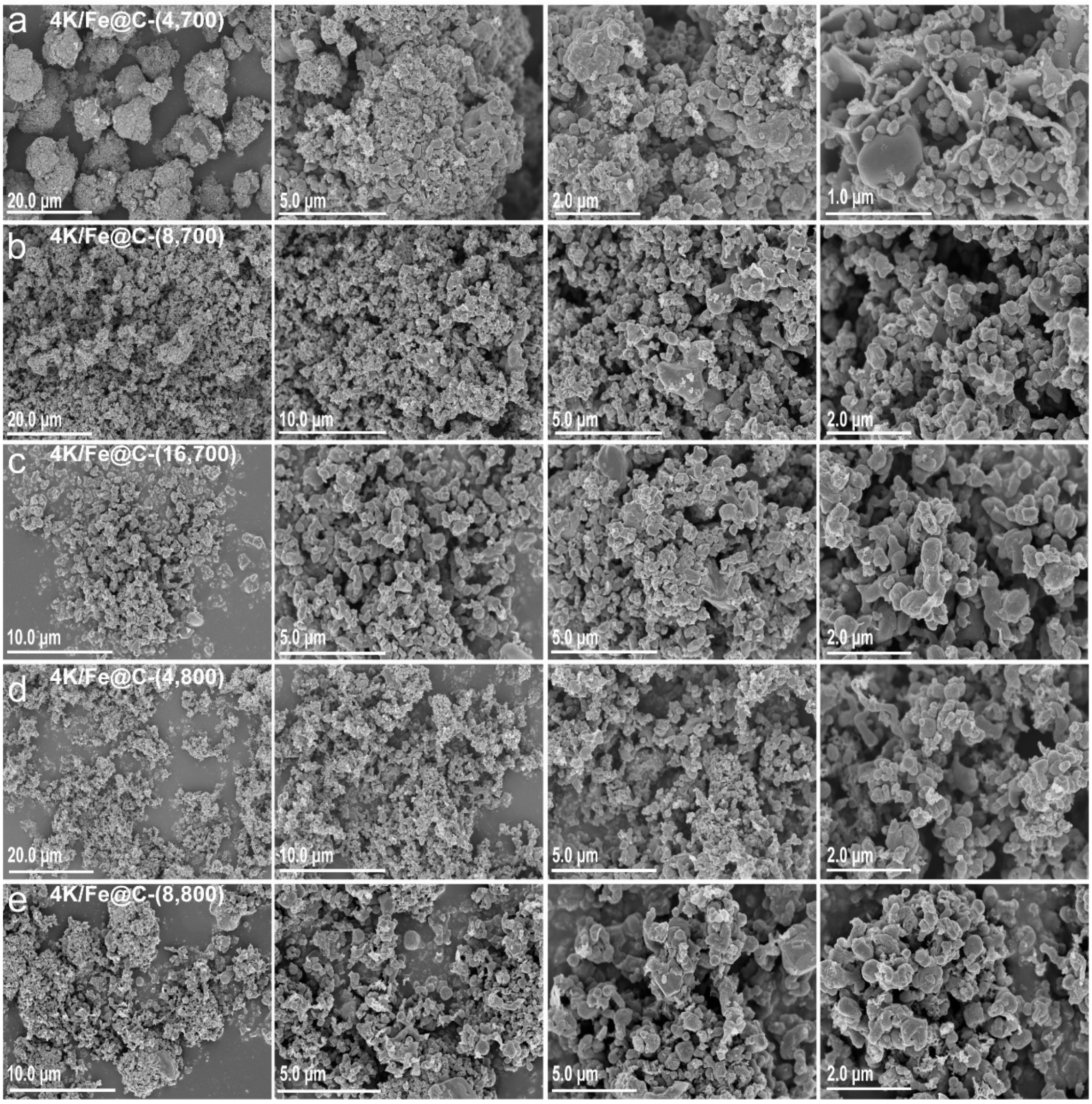

Fig. S56. SEM images of (a) 4K/Fe@C(4,700), (b) 4K/Fe@C(8,700), (c) 4K/Fe@C(16,700), (d) 4K/Fe@C-(4,800), and (e) 4K/Fe@C-(8,800) catalysts. Note that synthesized materials were presented in a Fe@C(x,y) manner, where x and y refer to the pyrolysis duration (in hours) and temperature (in °C), respectively. Specifically, 4K/Fe@C(4,700) material displayed smaller particle sizes (~ 23nm) predominantly distributed on carbonaceous matrix with porous structures, while other pyrolyzed materials exhibited dispersed carbon-coated iron particles.

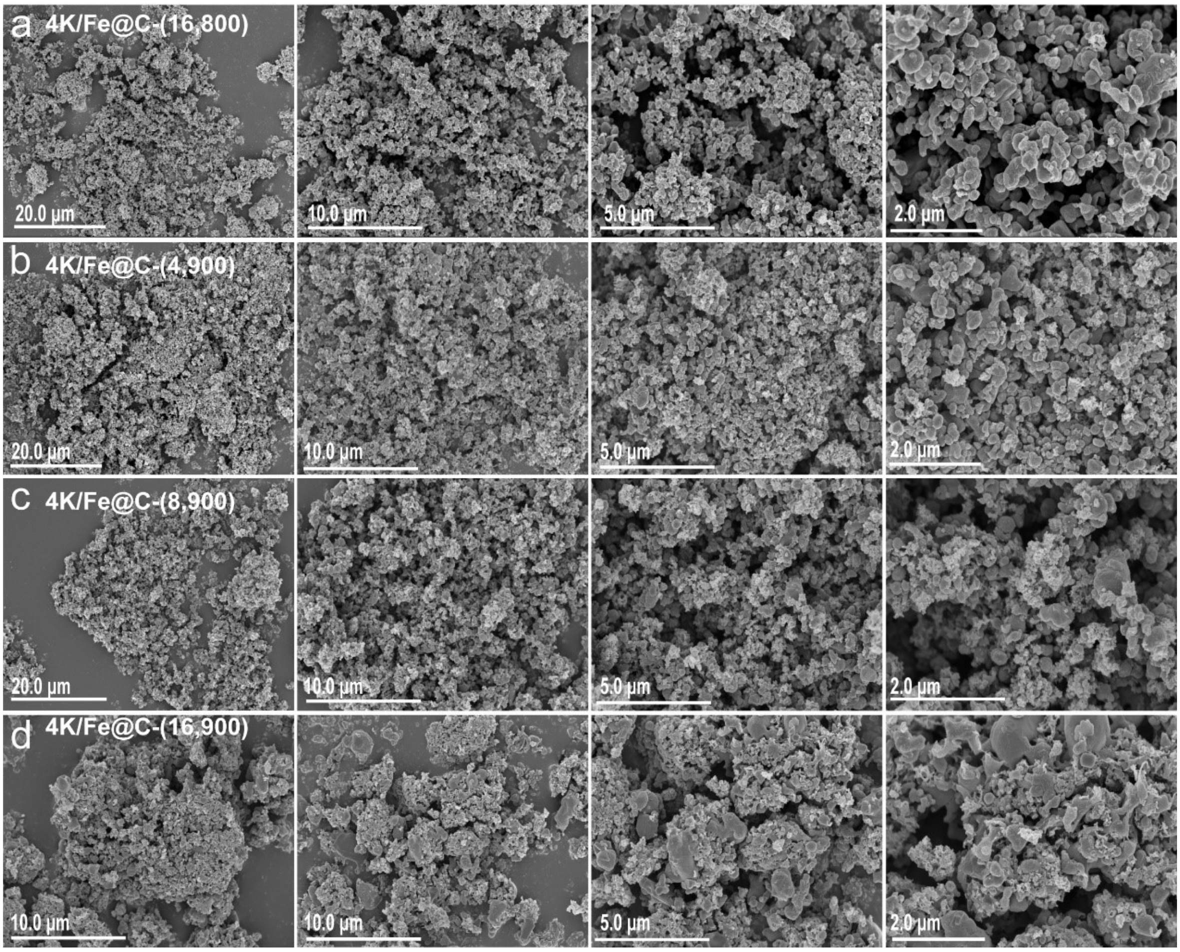

Fig. S57. SEM images of (a) 4K/Fe@C(16,800), (b) 4K/Fe@C(4,900), (c) 4K/Fe@C(8,900), and (d) 4K/Fe@C-(16,900) catalysts. Note that synthesized materials were presented in a Fe@C(x,y) manner, where x and y refer to the pyrolysis duration (in hours) and temperature (in °C), respectively. 4K/Fe@C(8,900) and 4K/Fe@C(16,900) materials manifested particle aggregation, possibly due to the higher calcination temperatures and prolonged durations, while other pyrolyzed materials exhibited dispersed carbon-coated iron particles.

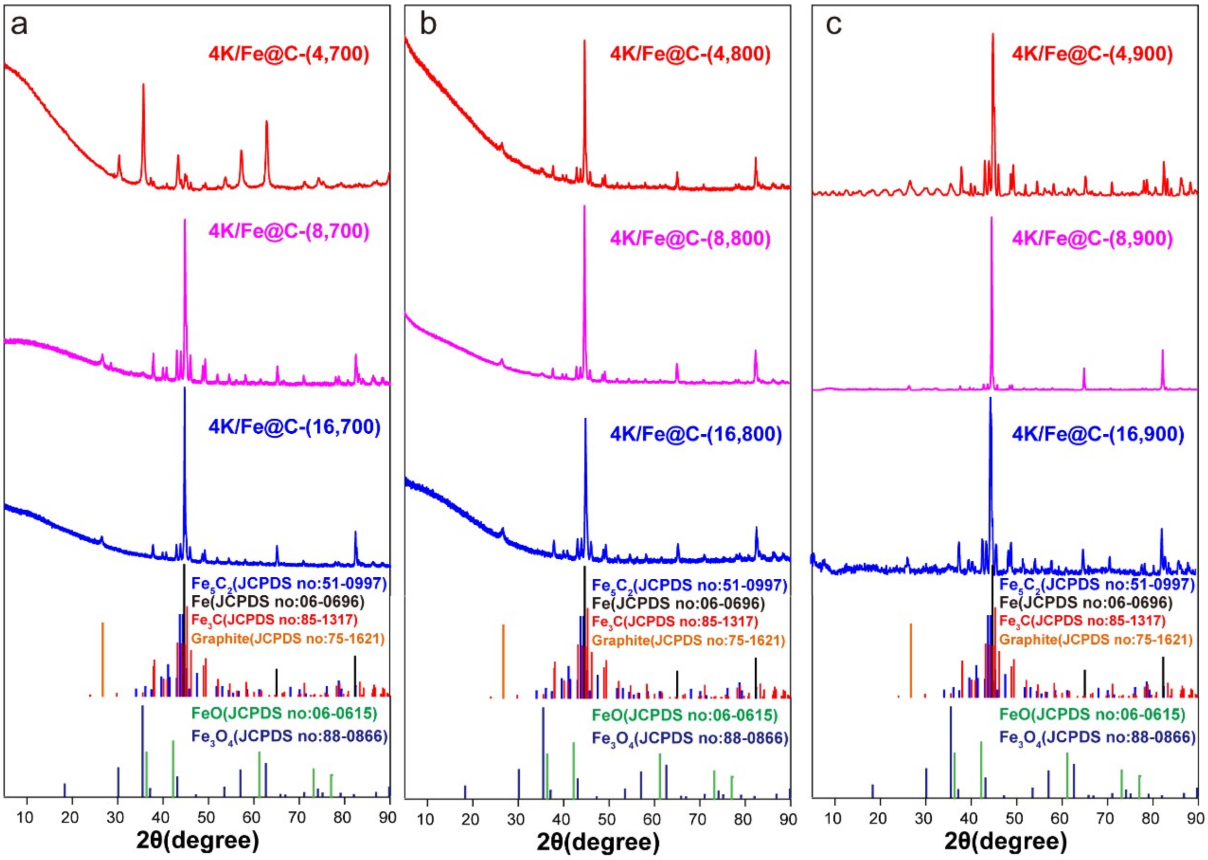

Fig. S58. XRD patterns of (a) 4K/Fe@C-700, (b) 4K/Fe@C-800, (c) 4K/Fe@C-900 catalysts. Note that synthesized materials were presented in a Fe@C(x,y) manner, where x and y refer to the pyrolysis duration (in hours) and temperature (in °C), respectively. For the 4K/Fe@C (4,700) catalyst, the main characteristic peak is Fe_3O_4, and the rest are mainly Fe_5C_2 and FeO; compared with the Fe@C (4,700) material, the addition of K is conducive to the reoxidation of iron[3,4]. For other catalysts, due to the high degree of graphitization, the reoxidation of K does not change significantly, and the main characteristic peak is Fe, and there are some Fe_5C_2 and Fe_3C.

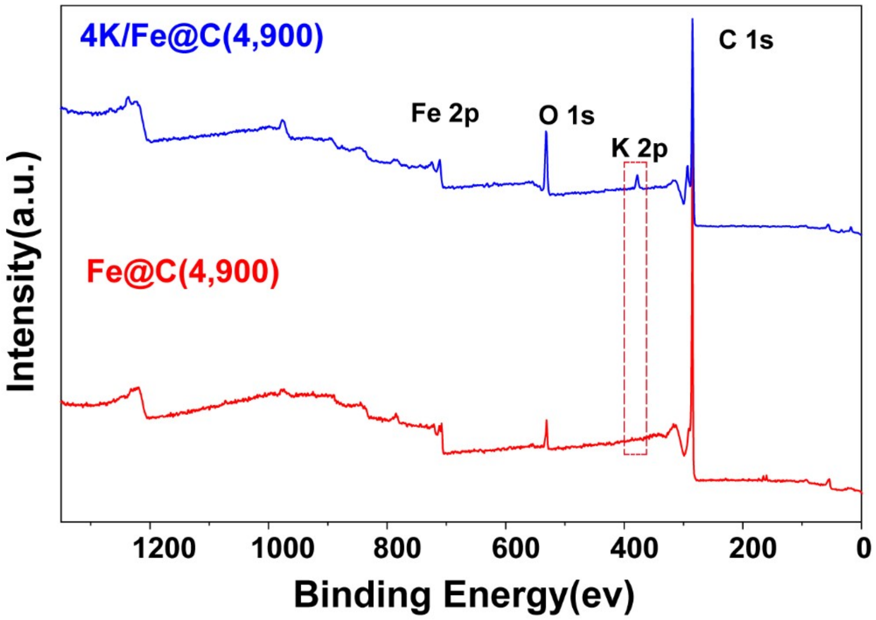

Fig. S59. XPS survey scan of 4K/Fe@C(16,900) and Fe@C-(4,900) catalysts. Note that synthesized materials were presented in a Fe@C(x,y) manner, where x and y refer to the pyrolysis duration (in hours) and temperature (in °C), respectively. It can be seen that C, O, and Fe are the major elements on the surface. After impregnating K metal, the O 1s peak increased, indicating that the addition of K was conducive to the reoxidation of Fe[3,4]. The catalyst after impregnation showed an obvious K 2p peak pattern.

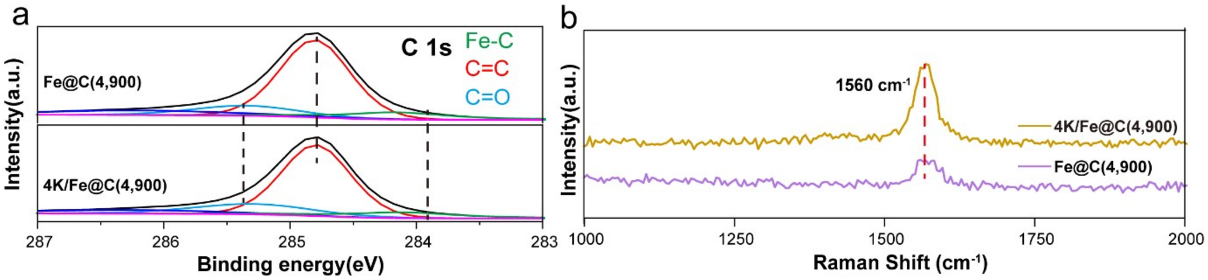

Fig. S60. (a) XPS survey scan of C 1s high-resolution and (b) Raman spectra of Fe@C catalysts for MIL-100-derived Fe@C catalysts. Note that synthesized materials were presented in a Fe@C(x,y) manner, where x and y refer to the pyrolysis duration (in hours) and temperature (in °C), respectively. After the addition of K, the degree of graphitization increases. The C1s segment of XPS showed a change from 36.3% for Fe@C (4,900) to 47.0% for 4K/Fe@C (4,900). Raman spectroscopy also showed that the enhancement of the G-bond peak obtained the same phenomenon.

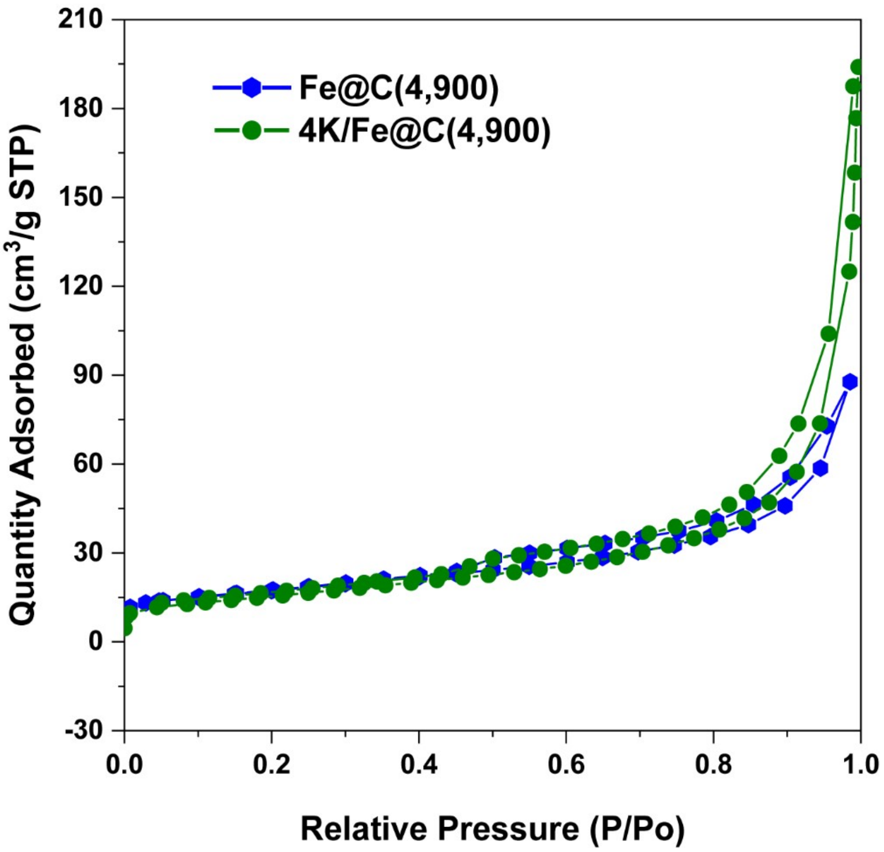

Fig. S61. Nitrogen adsorption/desorption isotherms of Fe@C(4,900) and 4K/Fe@C-(4,900) catalysts. Note that synthesized materials were presented in a Fe@C(x,y) manner, where x and y refer to the pyrolysis duration (in hours) and temperature (in °C), respectively.

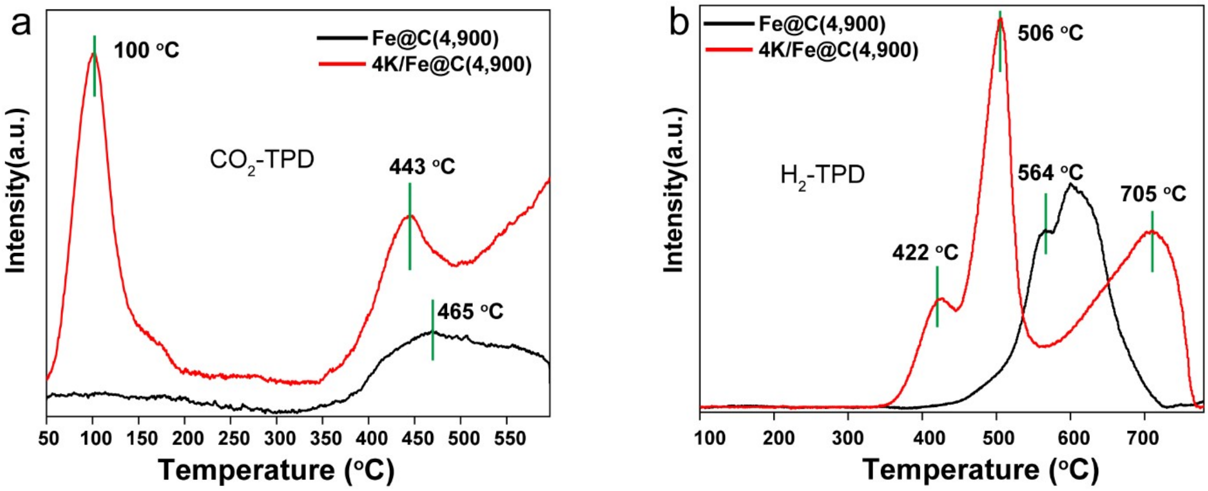

Fig. S62. (a) CO_2-TPD and (b) H_2-TPD profiles of 4K/Fe@C(4,900) and Fe@C(4,900) catalysts.

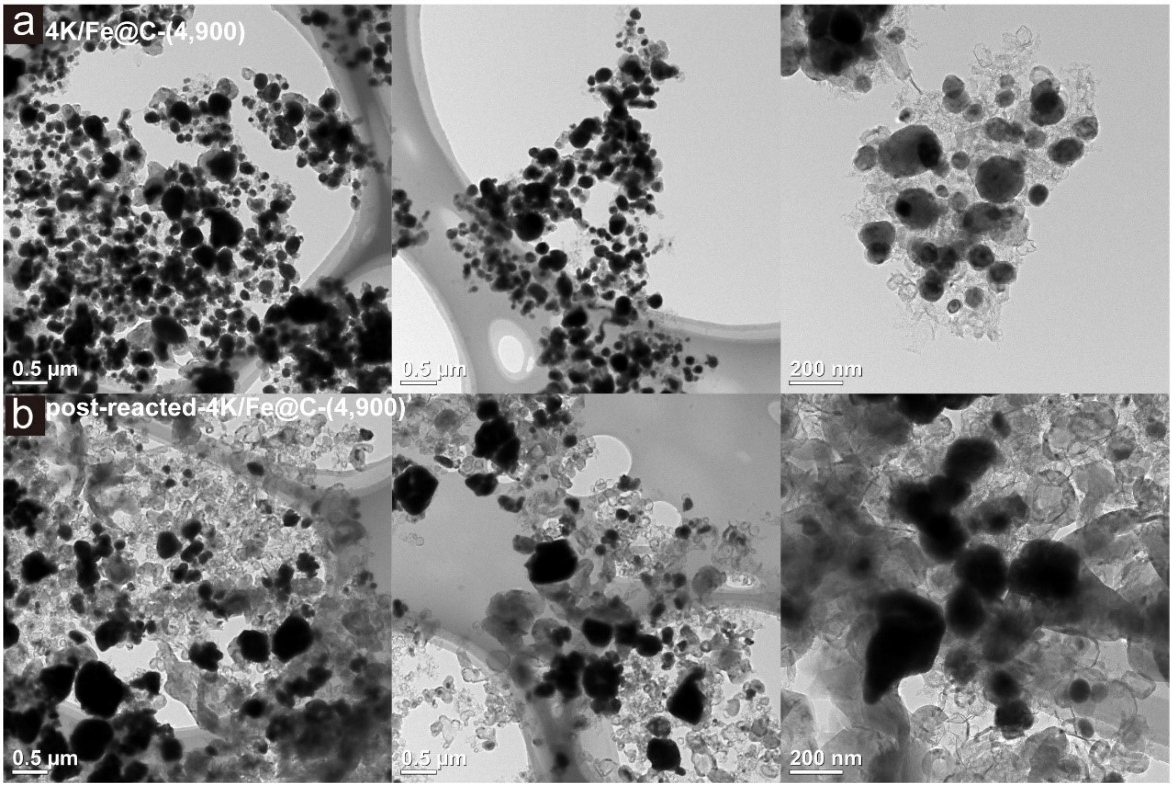

Fig. S63. TEM images of (a) 4K/Fe@C(4,900) and (b) post-reacted-4K/Fe@C(4,900) catalysts. Note that synthesized materials were presented in a Fe@C(x,y) manner, where x and y refer to the pyrolysis duration (in hours) and temperature (in °C), respectively. The catalyst after the reaction also has high dispersion and no obvious aggregation.

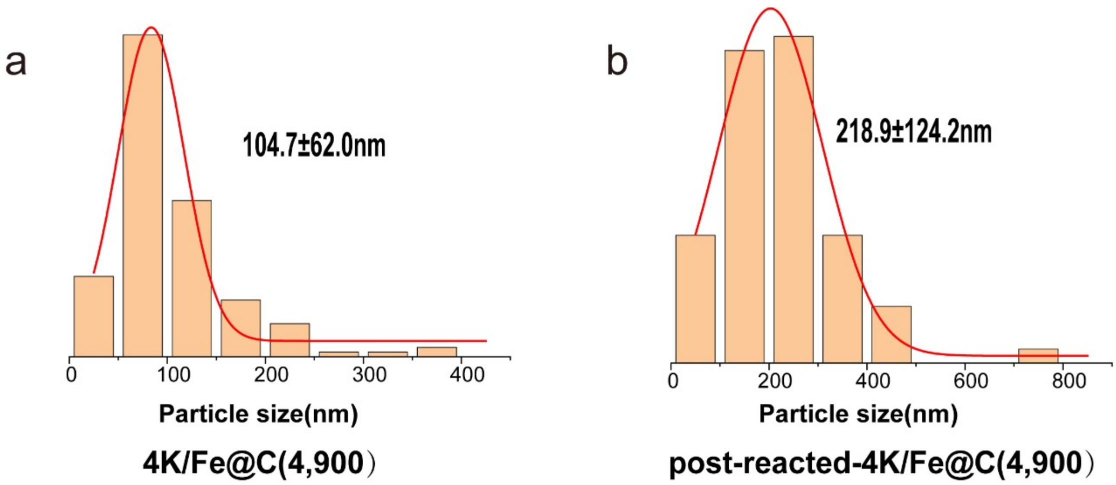

Fig. S64. Particle size distributions of (a) 4K/Fe@C(4,900) and (b) post-reacted-4K/Fe@C(4,900) catalysts. The post-reacted catalysts were collected after 24 hours of reaction. Note that synthesized materials were presented in a Fe@C(x,y) manner, where x and y refer to the pyrolysis duration (in hours) and temperature (in °C), respectively. The size of 4K/Fe@C (4,900) increased from 104.7 nm to 218.9 nm before the reaction, and the grain size increased mainly due to the change to Fe_3O_4[11,12].

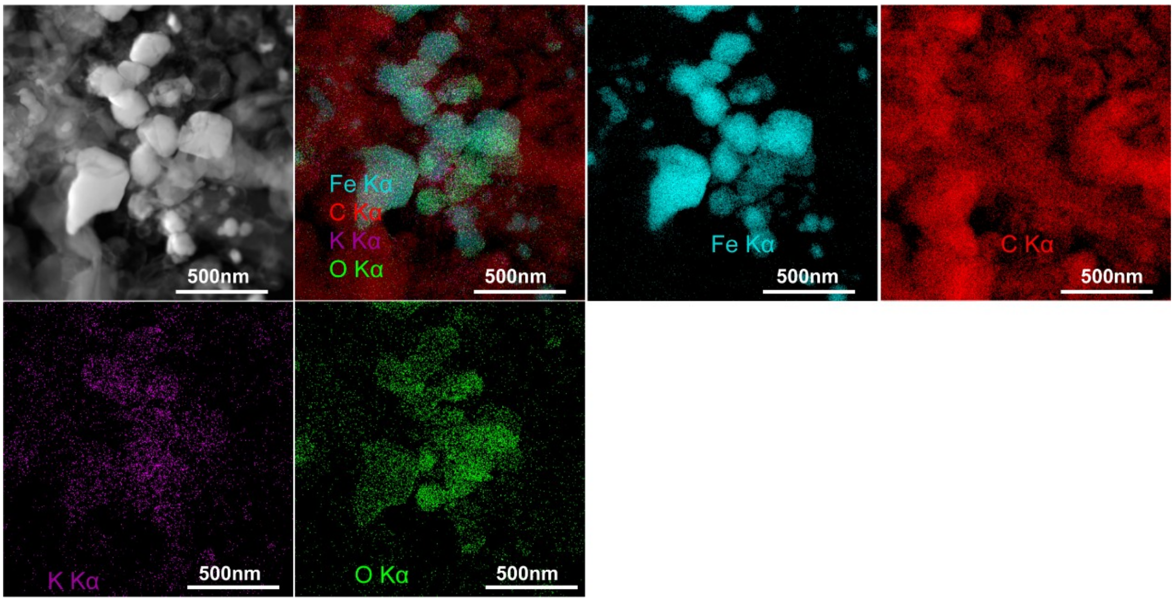

Fig. S65. HAADF-STEM imaging and elemental of post-reacted-4K/Fe@C(4,900) catalysts. Note that synthesized materials were presented in a Fe@C(x,y) manner, where x and y refer to the pyrolysis duration (in hours) and temperature (in °C), respectively. The catalyst after the reaction also has high dispersion, and the element distribution is very uniform, and there is no obvious aggregation.

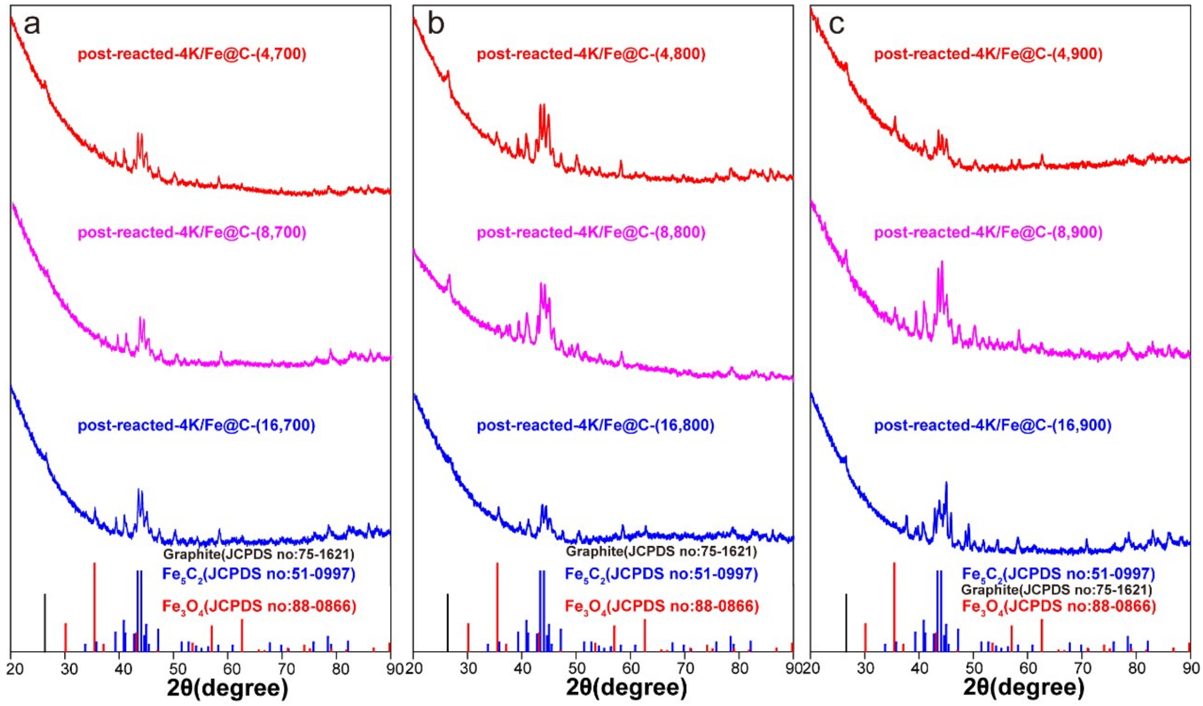

Fig. S66. XRD patterns of post-reacted (a) 4K/Fe@C-700, (b) 4K/Fe@C-800, and (c) 4K/Fe@C-900 catalysts. Note that synthesized materials were presented in a Fe@C(x,y) manner, where x and y refer to the pyrolysis duration (in hours) and temperature (in °C), respectively. All the catalysts after the reaction showed obvious Fe_5C_2 phase and Fe_3O_4 phase. The addition of K is conducive to the carbonization of iron to form Fe_5C_2.

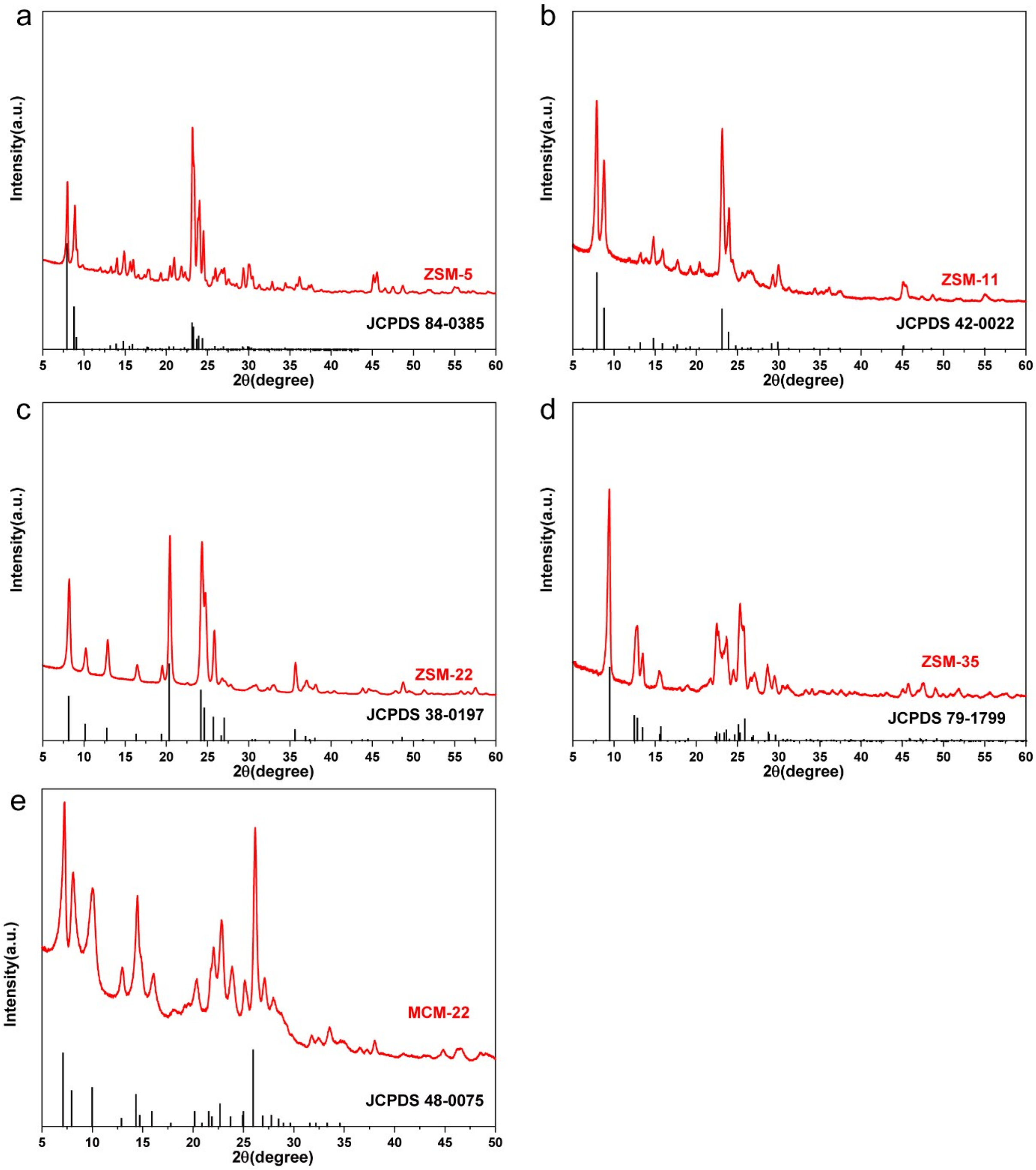

Fig. S67. XRD patterns of various zeolites with different framework topologies: (a) ZSM-5, (b) ZSM-11, (c) ZSM-22, (d) ZSM-35, and (e) MCM-22. Their XRD patterns confirmed their matching structures and high crystallinity compared to the corresponding JCPDS cards.

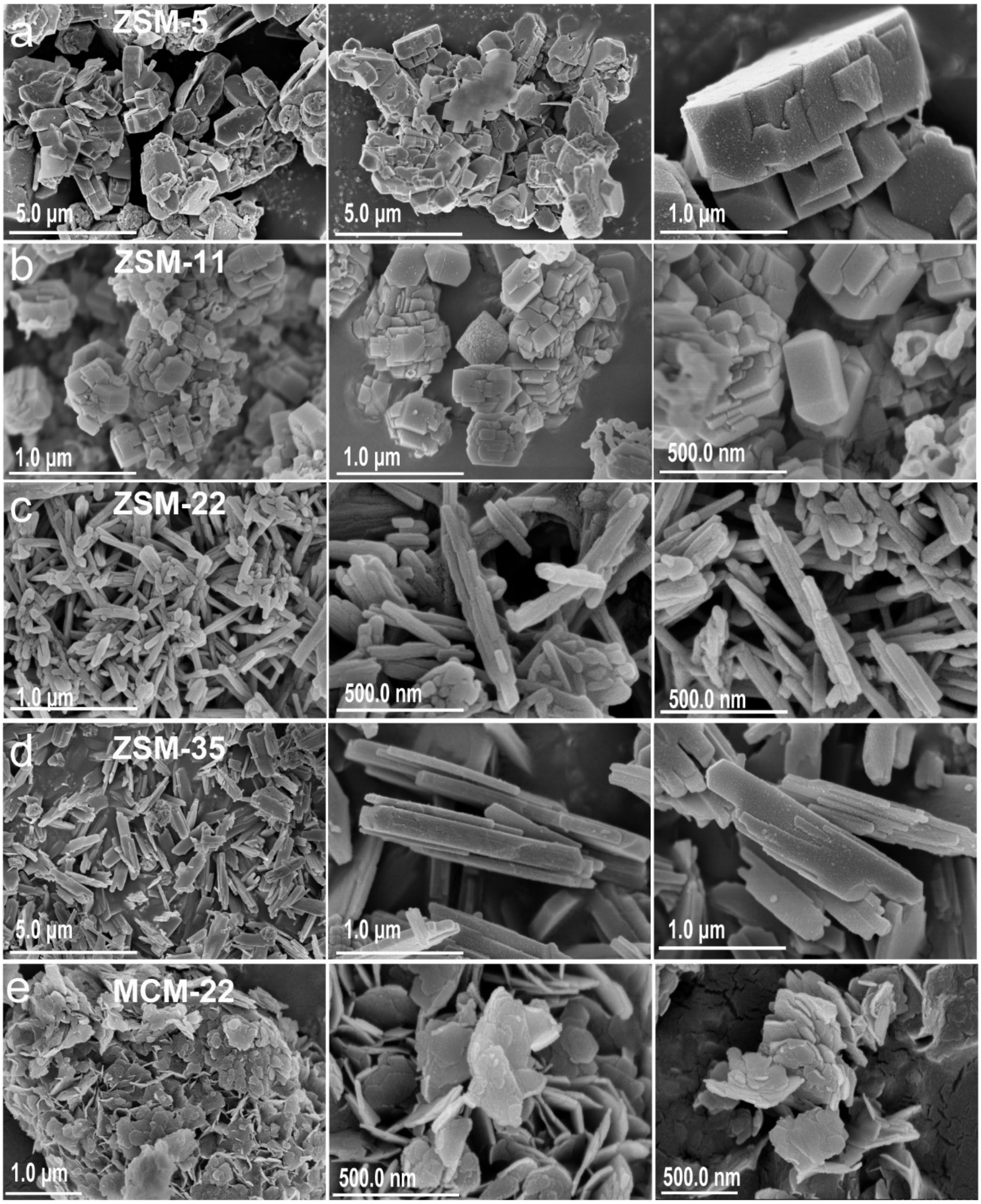

Fig. S68. SEM images of various zeolites with different framework topologies: (a) ZSM-5, (b) ZSM-11, (c) ZSM-22, (d) ZSM-35, and (e) MCM-22. SEM images showed that ZSM-5, ZSM-11, and ZSM-35 zeolites consisted of large single crystals larger than 1 μm, while the other zeolites, ZSM-22 had nanoscale dimensions. ZSM-35 and ZSM-5 zeolites showed typical morphologies of flakes and rectangular prisms with particle sizes ranging from 0.3 μm to 1.0 μm. ZSM-22, MCM-22 and ZSM-11 zeolites displayed regular shapes composed of nanorods or nanospheres with particle sizes ranging from 0.1 μm to 3.0 μm.

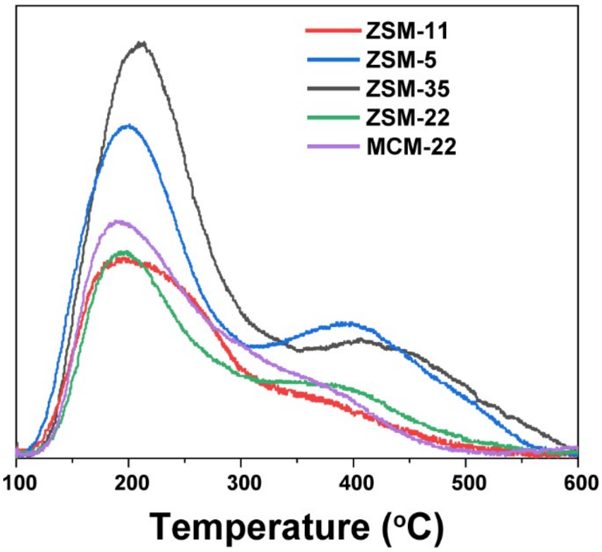

Fig. S69. NH_3-TPD adsorption isotherms of various zeolites with different framework topologies. NH_3-TPD experiments were performed to measure the strong acid site density of these zeolites, which is usually considered to be the Brønsted acid site (BAS) related to the substitution of Si by Al atoms in the zeolite framework[16–19]. All 10MR zeolites have strong acid peaks (greater than 300 degrees) and weak acid peaks (100-300 degrees)[19,20].

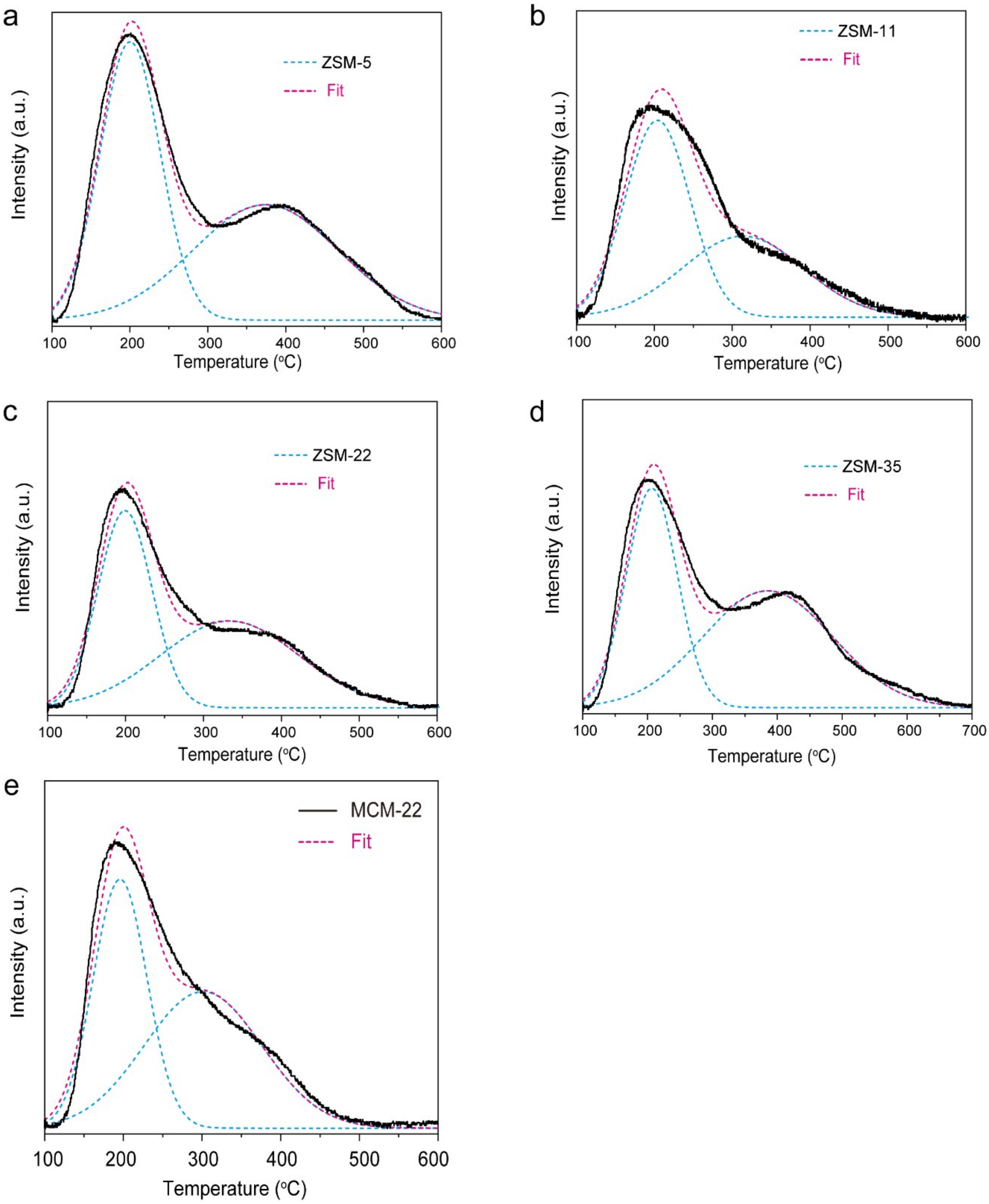

Fig. S70. NH_3-TPD adsorption isotherms of various zeolites with different framework topologies: (a) ZSM-5, (b) ZSM-11, (c) ZSM-22, and (d) ZSM-35, (e) MCM-22. All zeolites exhibit strong and weak acid peaks. The proportion of strong acid peaks in ZSM-5 was higher than that of ZSM-11 and MCM-22, while the proportion of weak acid peaks in ZSM-11 and MCM-22 was higher. The proportion of strong acid peaks in ZSM-35 was higher than that in ZSM-22, while the proportion of weak acid peaks in ZSM-22 was higher.

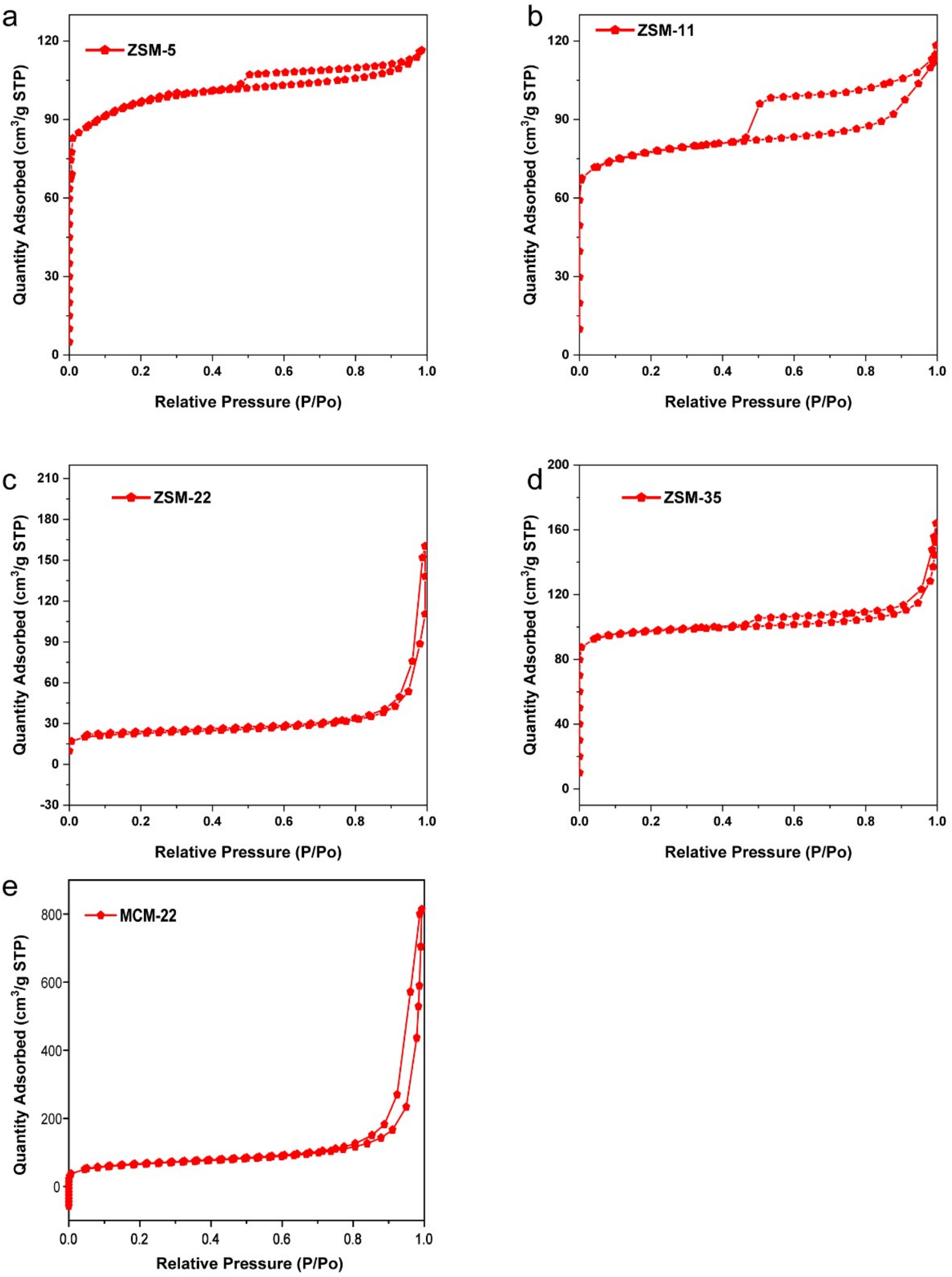

Fig. S71. N_2 adsorption isotherms of various zeolites with different framework topologies: (a) ZSM-5, (b) ZSM-11, (c) ZSM-22 and (d) ZSM-35, (e) MCM-22. All samples show a sharp increasing trend under a relative pressure of $P/P_0<0.01$, which is a typical feature of micropore appearance[17,20,21].

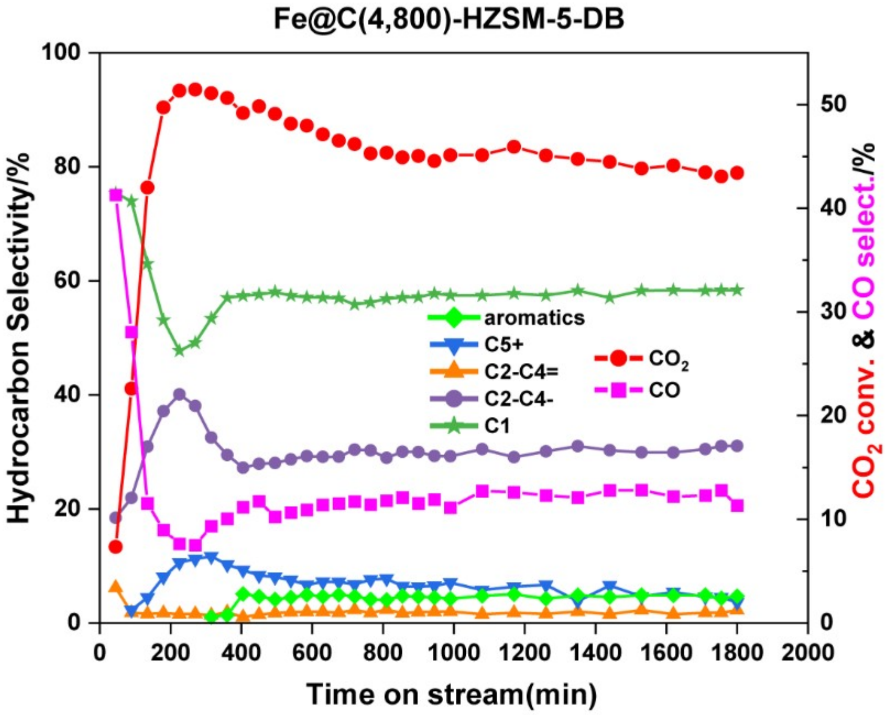

Fig. S72. Catalytic performance data of the metal/zeolite bifunctional material mediated CO_2 hydrogenation process: [Fe@C(4,800) + ZSM-5] dual-bed catalysts with respect to time-on-stream (in min) [Reaction condition: $H_2/CO_2 = 3$, 350 °C, 3 MPa, 4800 mL h^{-1}].

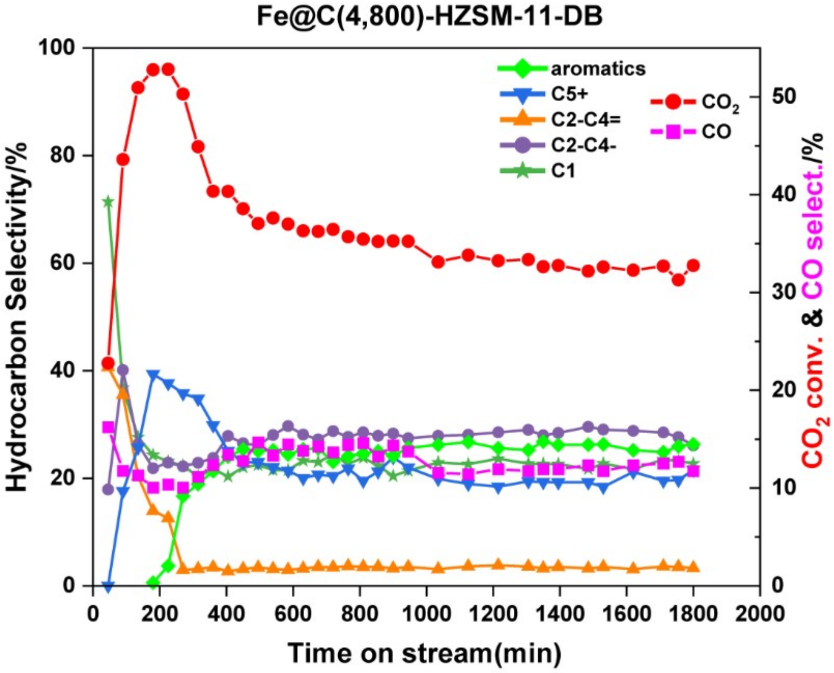

Fig. S73. Catalytic performance data of the metal/zeolite bifunctional material mediated CO_2 hydrogenation process: [Fe@C(4,800) + ZSM-11] dual-bed catalysts with respect to time-on-stream (in min) [Reaction condition: $H_2/CO_2 = 3$, 350 °C, 3 MPa, 4800 mL h^{-1}].

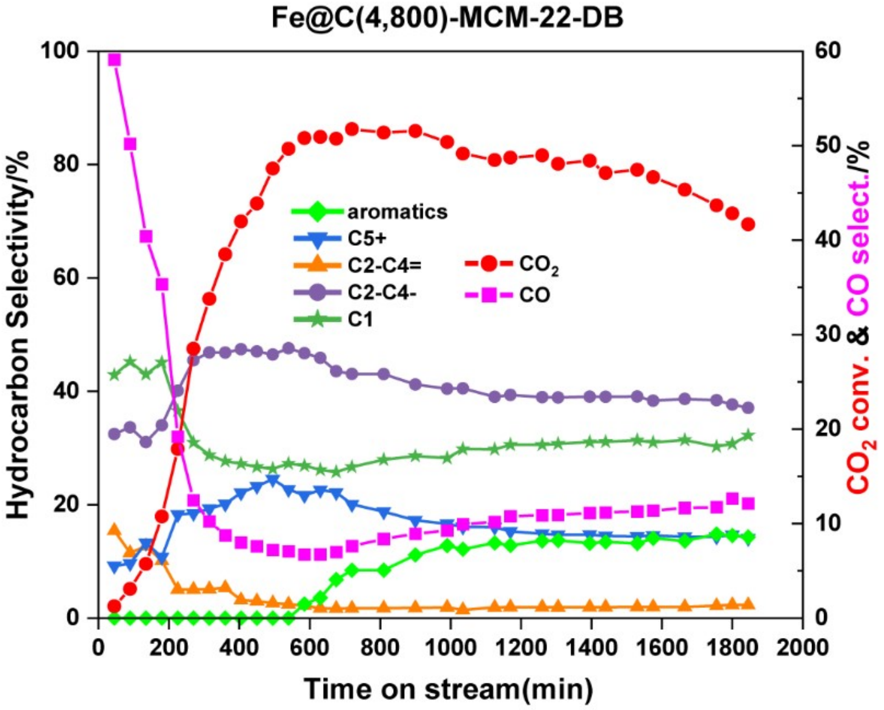

Fig. S74. Catalytic performance data of the metal/zeolite bifunctional material mediated CO_2 hydrogenation process: [Fe@C(4,800) + MCM-22] dual-bed catalysts with respect to time-on-stream (in min) [Reaction condition: $H_2/CO_2 = 3$, 350 °C, 3 MPa, 4800 mL h^{-1}].

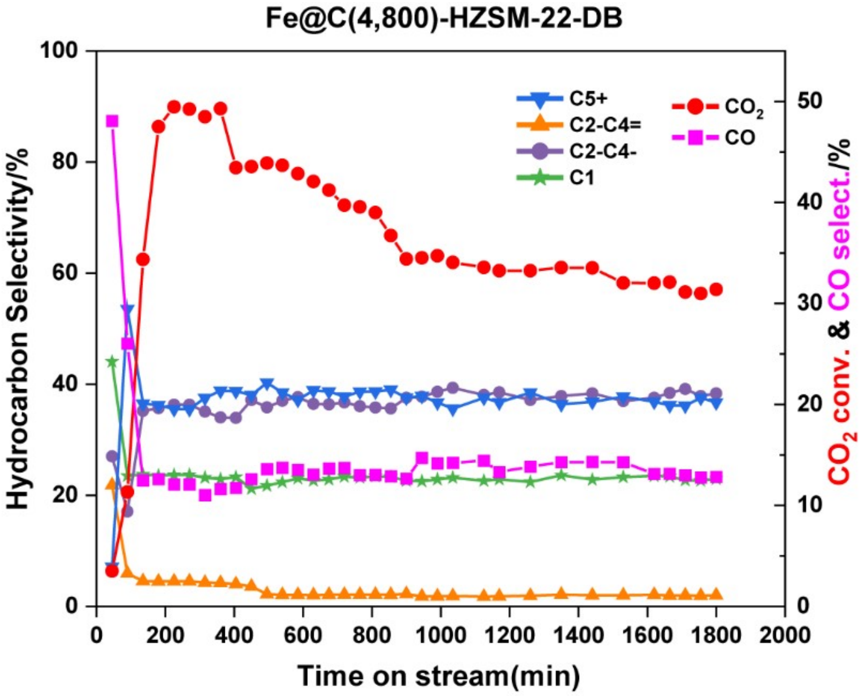

Fig. S75. Catalytic performance data of the metal/zeolite bifunctional material mediated CO_2 hydrogenation process: [Fe@C(4,800) + ZSM-22] dual-bed catalysts with respect to time-on-stream (in min) [Reaction condition: $H_2/CO_2 = 3$, 350 °C, 3 MPa, 4800 mL h^{-1}].

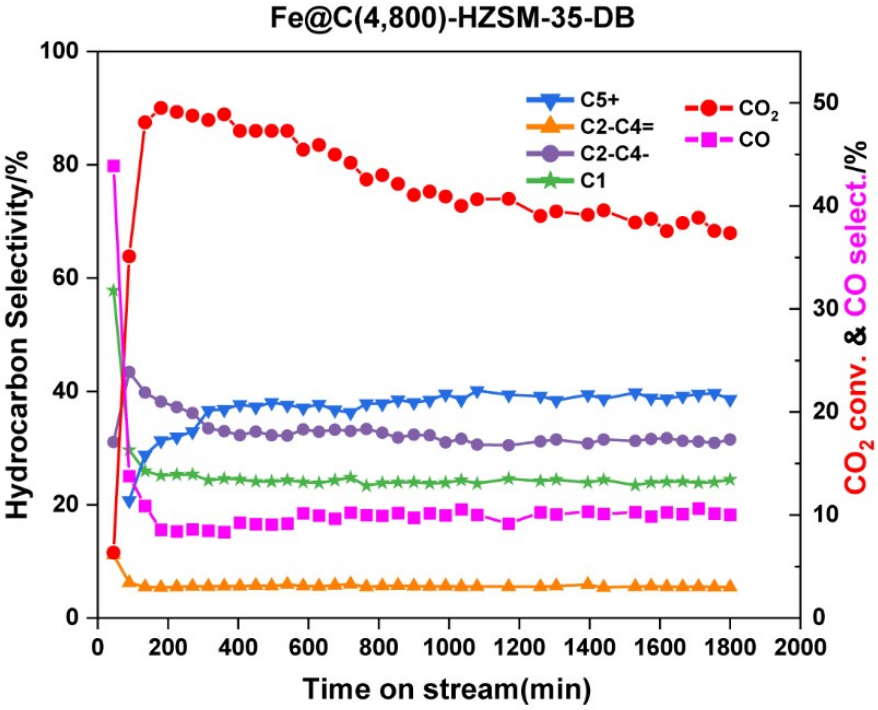

Fig. S76. Catalytic performance data of the metal/zeolite bifunctional material mediated CO_2 hydrogenation process: [Fe@C(4,800) + ZSM-35] dual-bed catalysts with respect to time-on-stream (in min) [Reaction condition: $H_2/CO_2 = 3$, 350 °C, 3 MPa, 4800 mL h^{-1}].

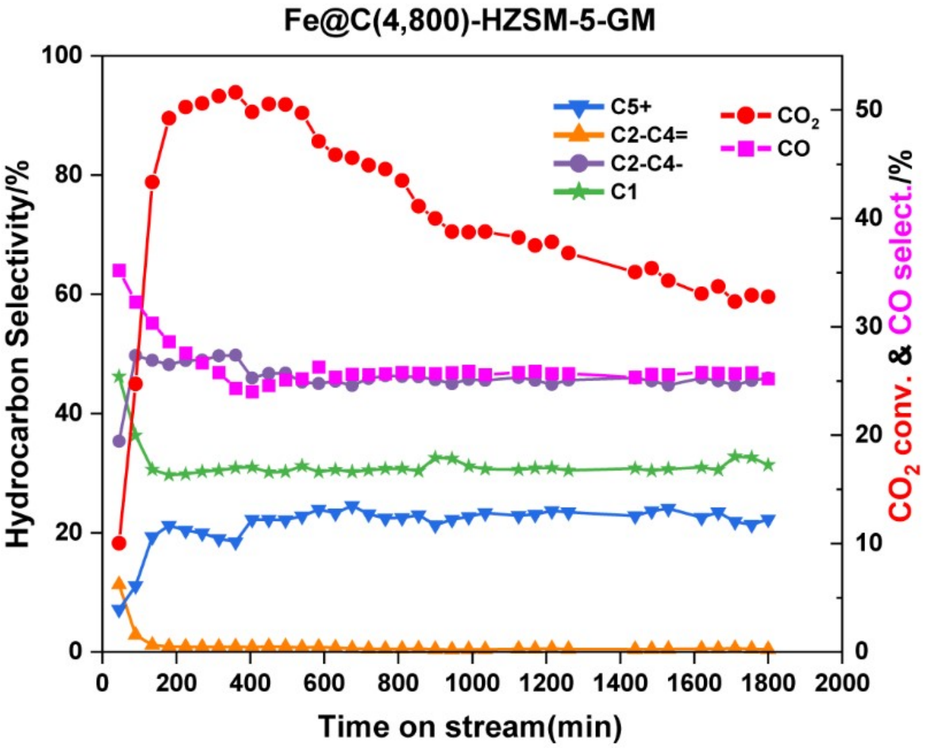

Fig. S77. Catalytic performance data of the metal/zeolite bifunctional material mediated CO_2 hydrogenation process: [Fe@C(4,800) + ZSM-5] granule-mixing catalysts with respect to time-on-stream (in min) [Reaction condition: $H_2/CO_2 = 3$, 350 °C, 3 MPa, 4800 mL h^{-1}].

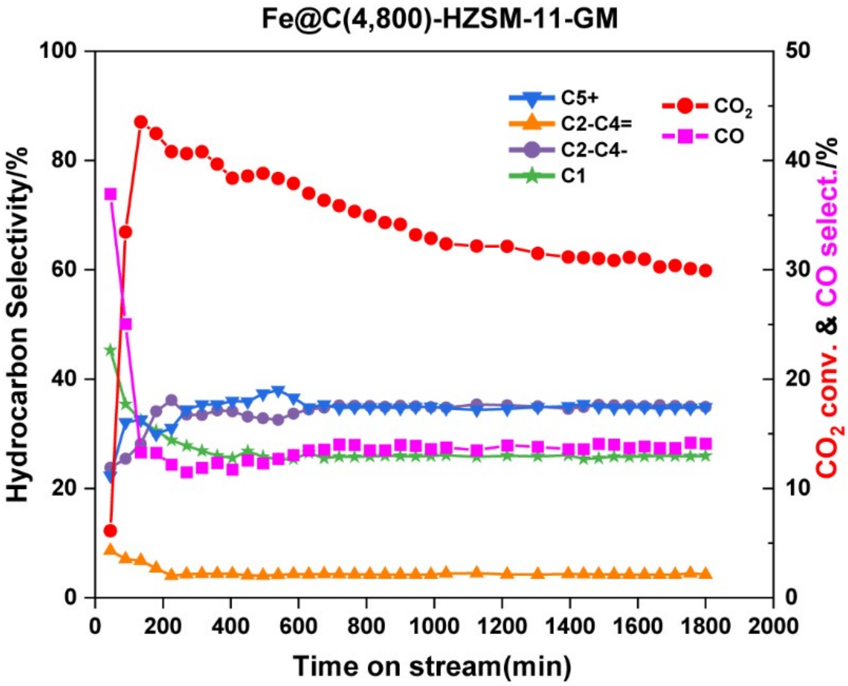

Fig. S78. Catalytic performance data of the metal/zeolite bifunctional material mediated CO_2 hydrogenation process: [Fe@C(4,800) + ZSM-11] granule-mixing catalysts with respect to time-on-stream (in min) [Reaction condition: $H_2/CO_2 = 3$, 350 °C, 3 MPa, 4800 mL h^{-1}].

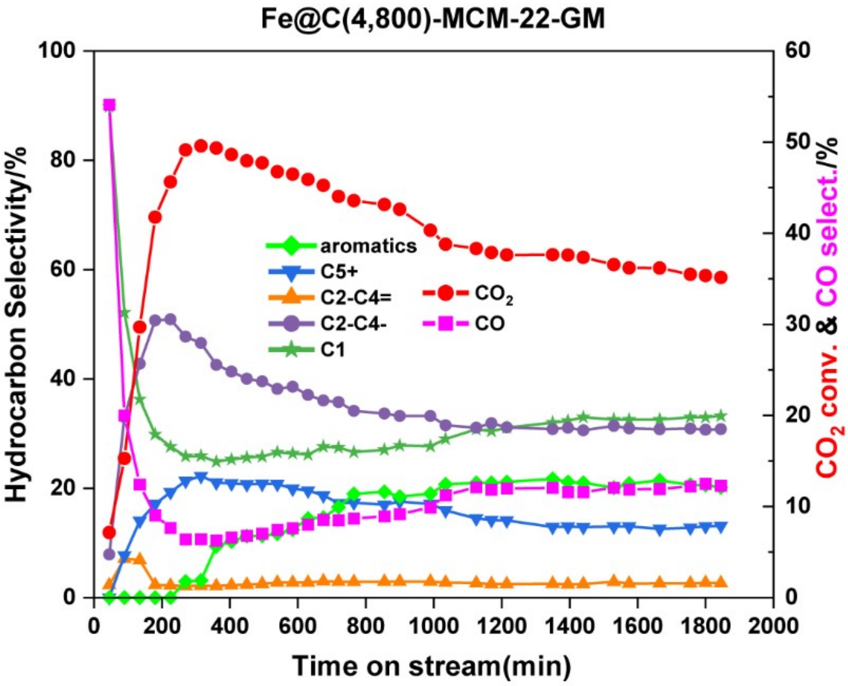

Fig. S79. Catalytic performance data of the metal/zeolite bifunctional material mediated CO_2 hydrogenation process: [Fe@C(4,800) + MCM-22] granule-mixing catalysts with respect to time-on-stream (in min) [Reaction condition: $H_2/CO_2 = 3$, 350 °C, 3 MPa, 4800 mL h^{-1}].

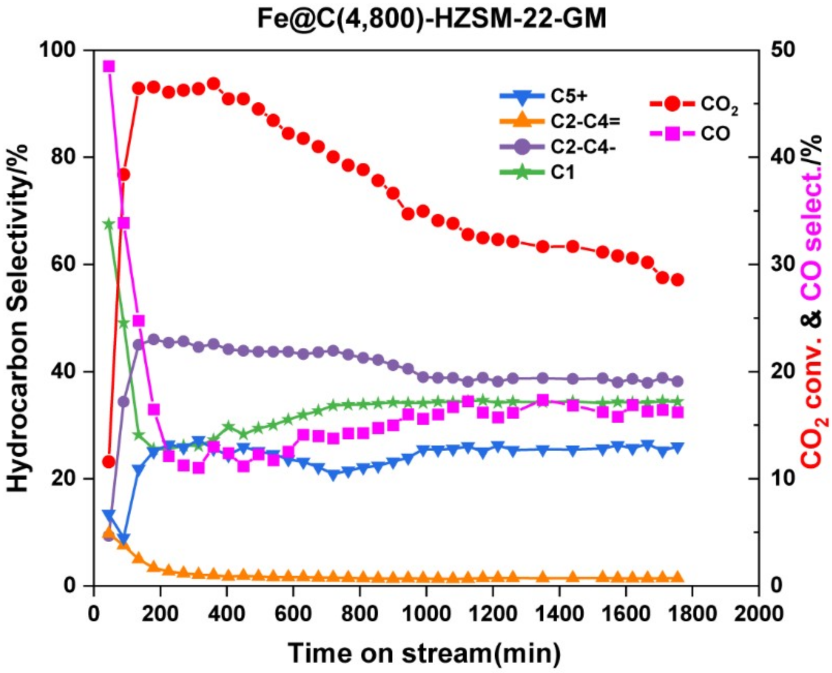

Fig. S80. Catalytic performance data of the metal/zeolite bifunctional material mediated CO_2 hydrogenation process: [Fe@C(4,800) + ZSM-22] granule-mixing catalysts with respect to time-on-stream (in min) [Reaction condition: $H_2/CO_2 = 3$, 350 °C, 3 MPa, 4800 mL h^{-1}].

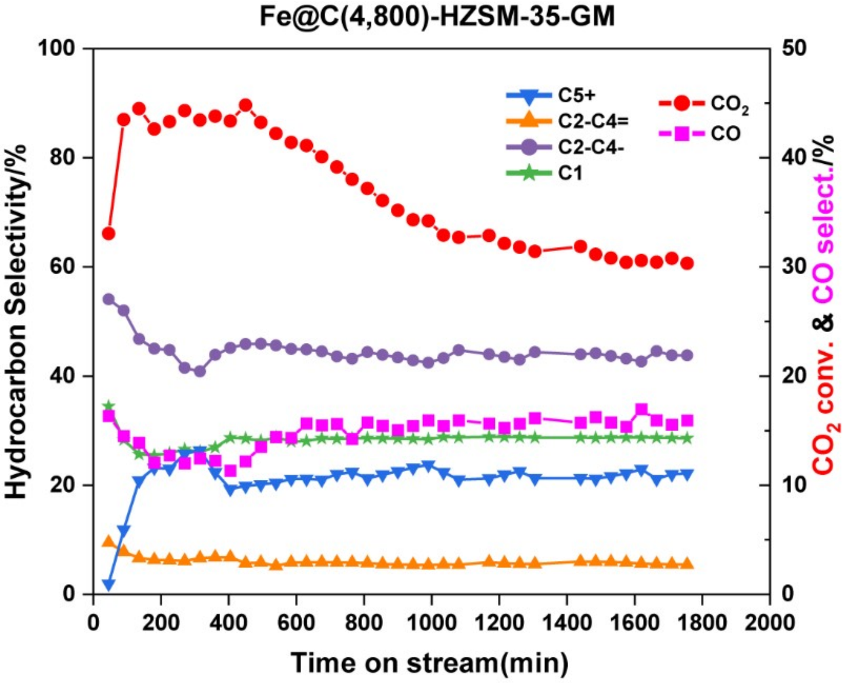

Fig. S81. Catalytic performance data of the metal/zeolite bifunctional material mediated CO_2 hydrogenation process: [Fe@C(4,800) + ZSM-35] granule-mixing catalysts with respect to time-on-stream (in min) [Reaction condition: $H_2/CO_2 = 3$, 350 °C, 3 MPa, 4800 mL h^{-1}].

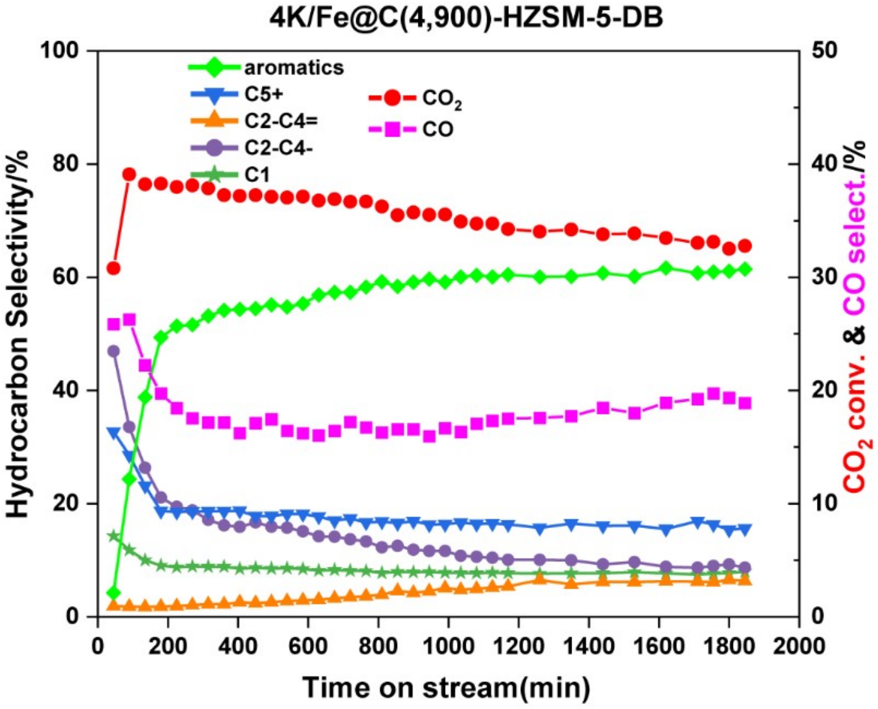

Fig. S82. Catalytic performance data of the metal/zeolite bifunctional material mediated CO_2 hydrogenation process: [4K/Fe@C(4,900) + ZSM-5] dual-bed catalysts with respect to time-on-stream (in min) [Reaction condition: $H_2/CO_2 = 3$, 350 °C, 3 MPa, 18000 mL h^{-1}].

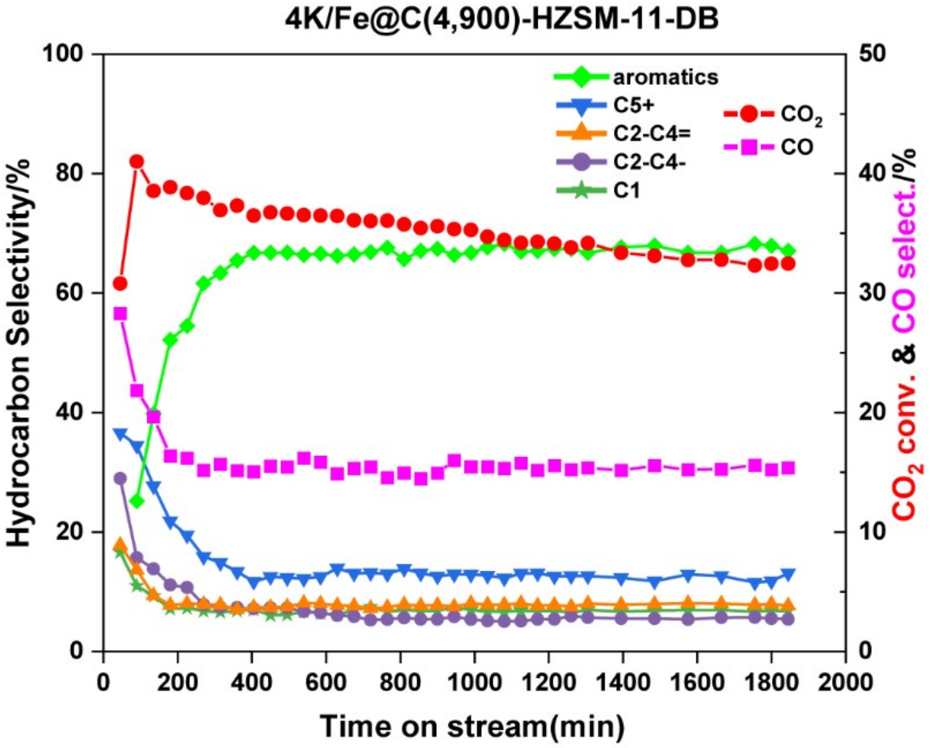

Fig. S83. Catalytic performance data of the metal/zeolite bifunctional material mediated CO_2 hydrogenation process: [4K/Fe@C(4,900) + ZSM-11] dual-bed catalysts with respect to time-on-stream (in min) [Reaction condition: $H_2/CO_2 = 3$, 350 °C, 3 MPa, 18000 mL h^{-1}].

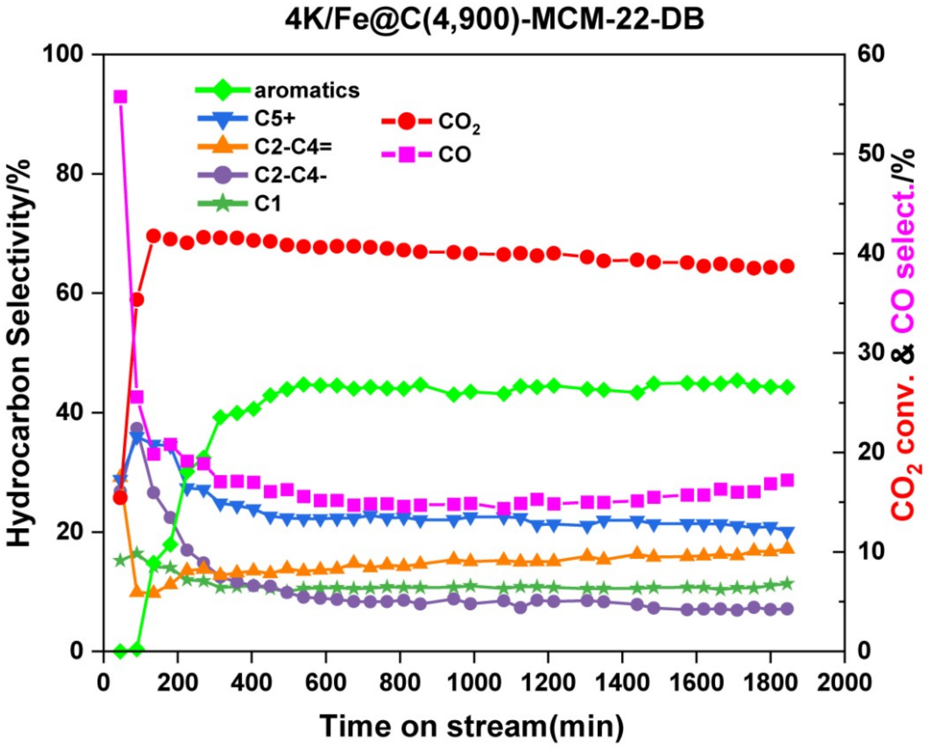

Fig. S84. Catalytic performance data of the metal/zeolite bifunctional material mediated CO_2 hydrogenation process: [4K/Fe@C(4,900) + MCM-22] dual-bed catalysts with respect to time-on-stream (in min) [Reaction condition: $H_2/CO_2 = 3$, 350 °C, 3 MPa, 18000 mL h^{-1}].

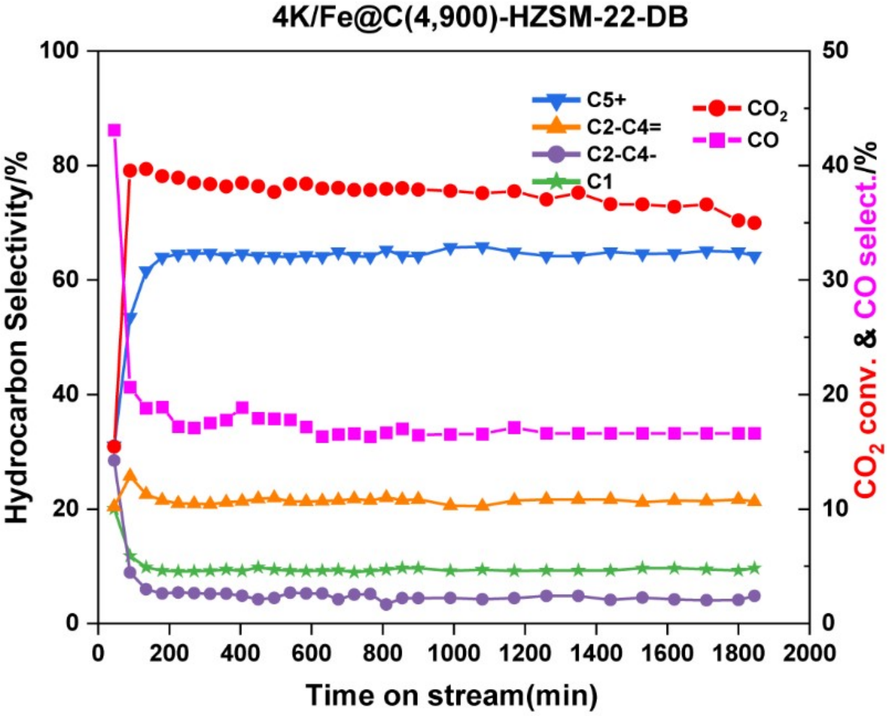

Fig. S85. Catalytic performance data of the metal/zeolite bifunctional material mediated CO_2 hydrogenation process: [4K/Fe@C(4,900) + ZSM-22] dual-bed catalysts with respect to time-on-stream (in min) [Reaction condition: $H_2/CO_2 = 3$, 350 °C, 3 MPa, 18000 mL h^{-1}].

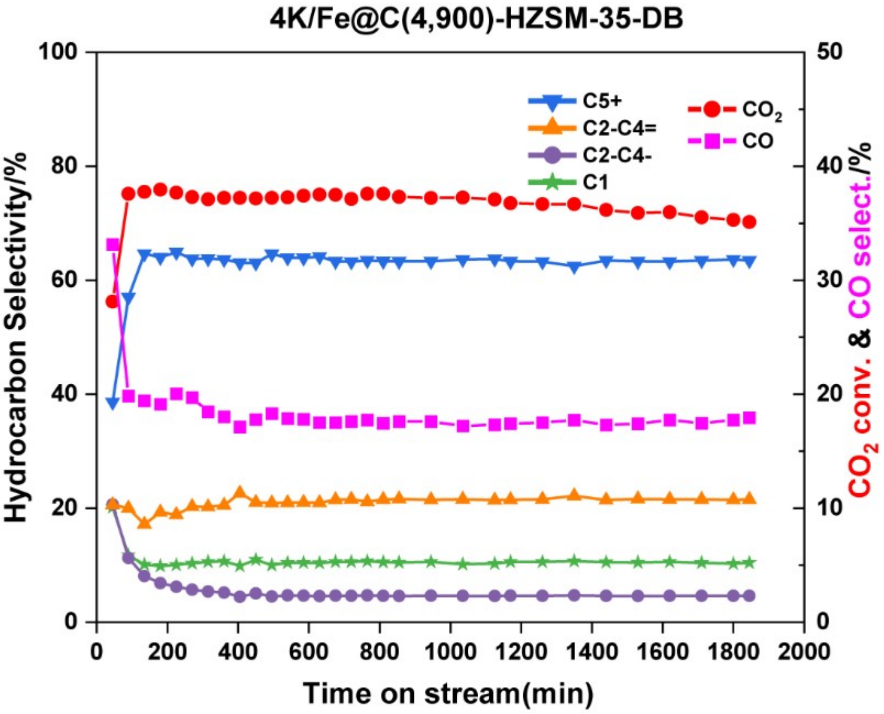

Fig. S86. Catalytic performance data of the metal/zeolite bifunctional material mediated CO_2 hydrogenation process: [4K/Fe@C(4,900) + ZSM-35] dual-bed catalysts with respect to time-on-stream (in min) [Reaction condition: $H_2/CO_2 = 3$, 350 °C, 3 MPa, 18000 mL h^{-1}].

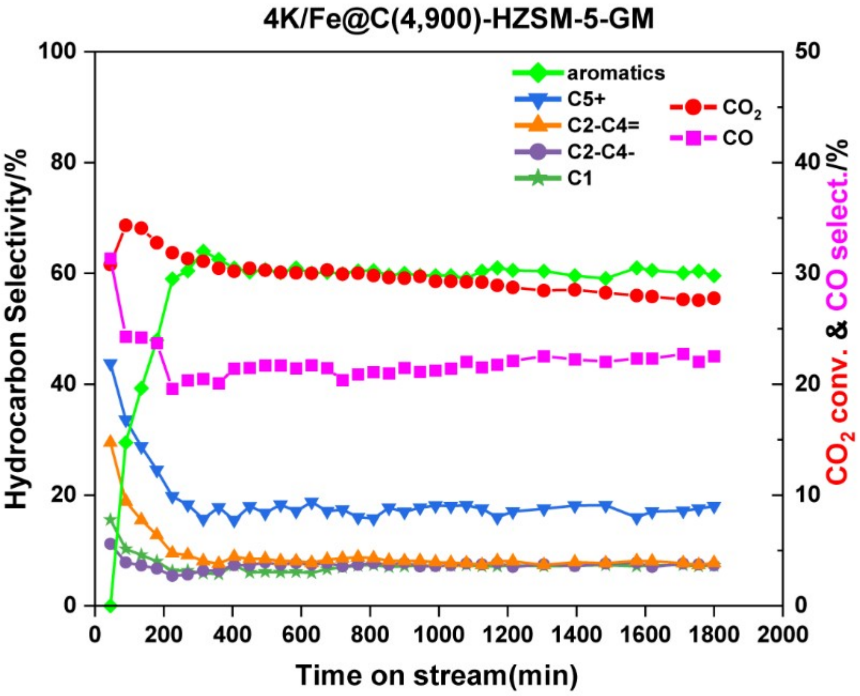

Fig. S87. Catalytic performance data of the metal/zeolite bifunctional material mediated CO_2 hydrogenation process: [4K/Fe@C(4,900) + ZSM-5] granule-mixing catalysts with respect to time-on-stream (in min) [Reaction condition: $H_2/CO_2 = 3$, 350 °C, 3 MPa, 18000 mL h^{-1}].

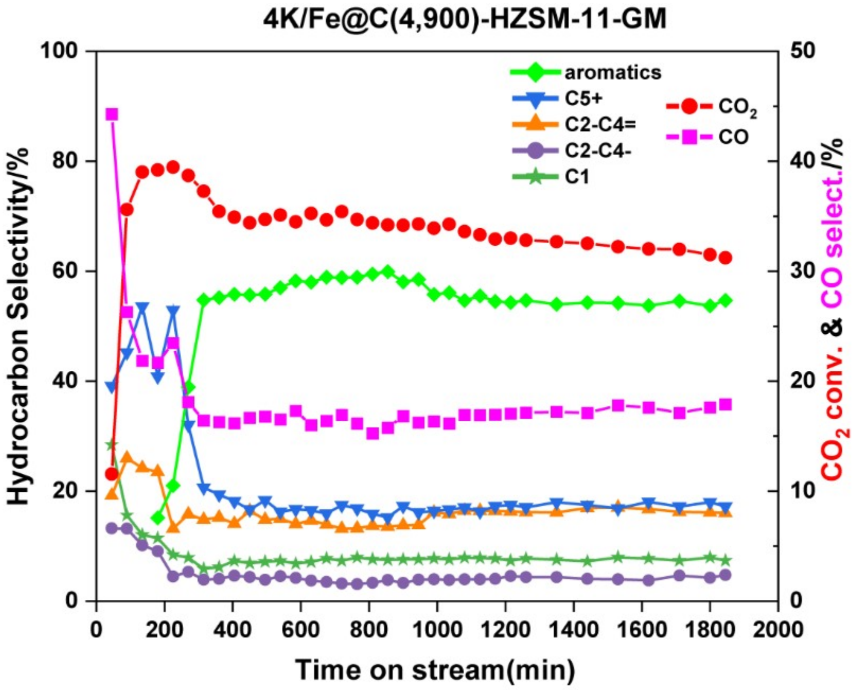

Fig. S88. Catalytic performance data of the metal/zeolite bifunctional material mediated CO_2 hydrogenation process: [4K/Fe@C(4,900) + ZSM-11] granule-mixing catalysts with respect to time-on-stream (in min) [Reaction condition: $H_2/CO_2 = 3$, 350 °C, 3 MPa, 18000 mL h^{-1}].

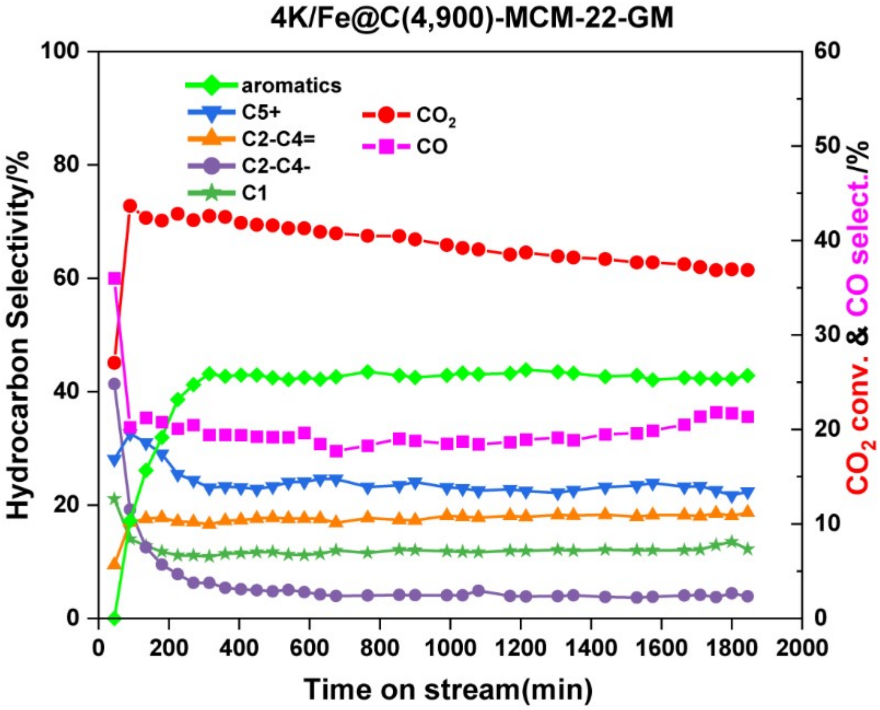

Fig. S89. Catalytic performance data of the metal/zeolite bifunctional material mediated CO_2 hydrogenation process: [4K/Fe@C(4,900) + MCM-22] granule-mixing catalysts with respect to time-on-stream (in min) [Reaction condition: $H_2/CO_2 = 3$, 350 °C, 3 MPa, 18000 mL h^{-1}].

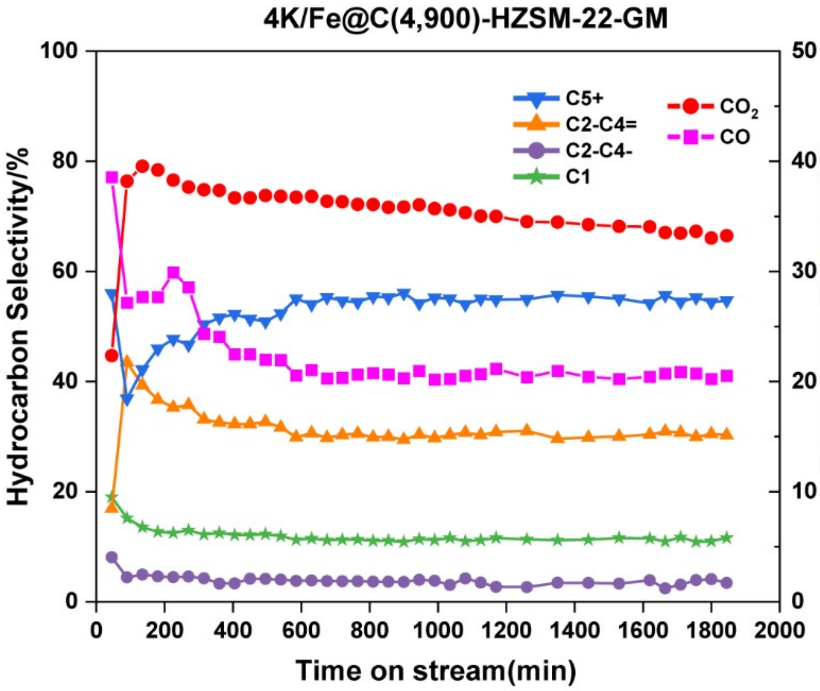

,L

Fig. S90. Catalytic performance data of the metal/zeolite bifunctional material mediated CO_2 hydrogenation process: [4K/Fe@C(4,900) + ZSM-22] granule-mixing catalysts with respect to time-on-stream (in min) [Reaction condition: $H_2/CO_2 = 3$, 350 °C, 3 MPa, 18000 mL h^{-1}].

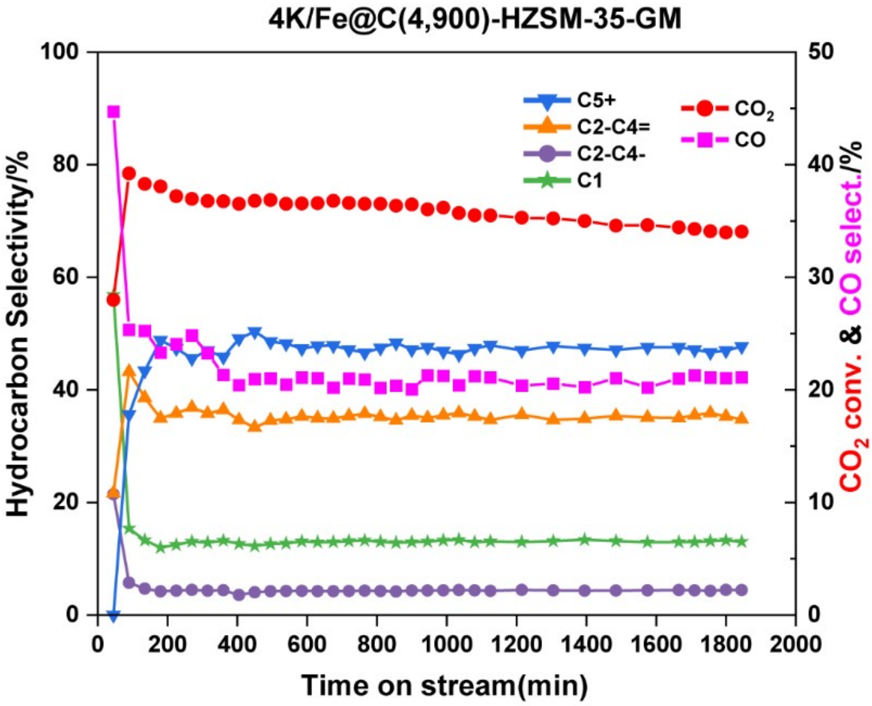

Fig. S91. Catalytic performance data of the metal/zeolite bifunctional material mediated CO_2 hydrogenation process: [4K/Fe@C(4,900) + ZSM-35] granule-mixing catalysts with respect to time-on-stream (in min) [Reaction condition: $H_2/CO_2 = 3$, 350 °C, 3 MPa, 18000 mL h^{-1}].

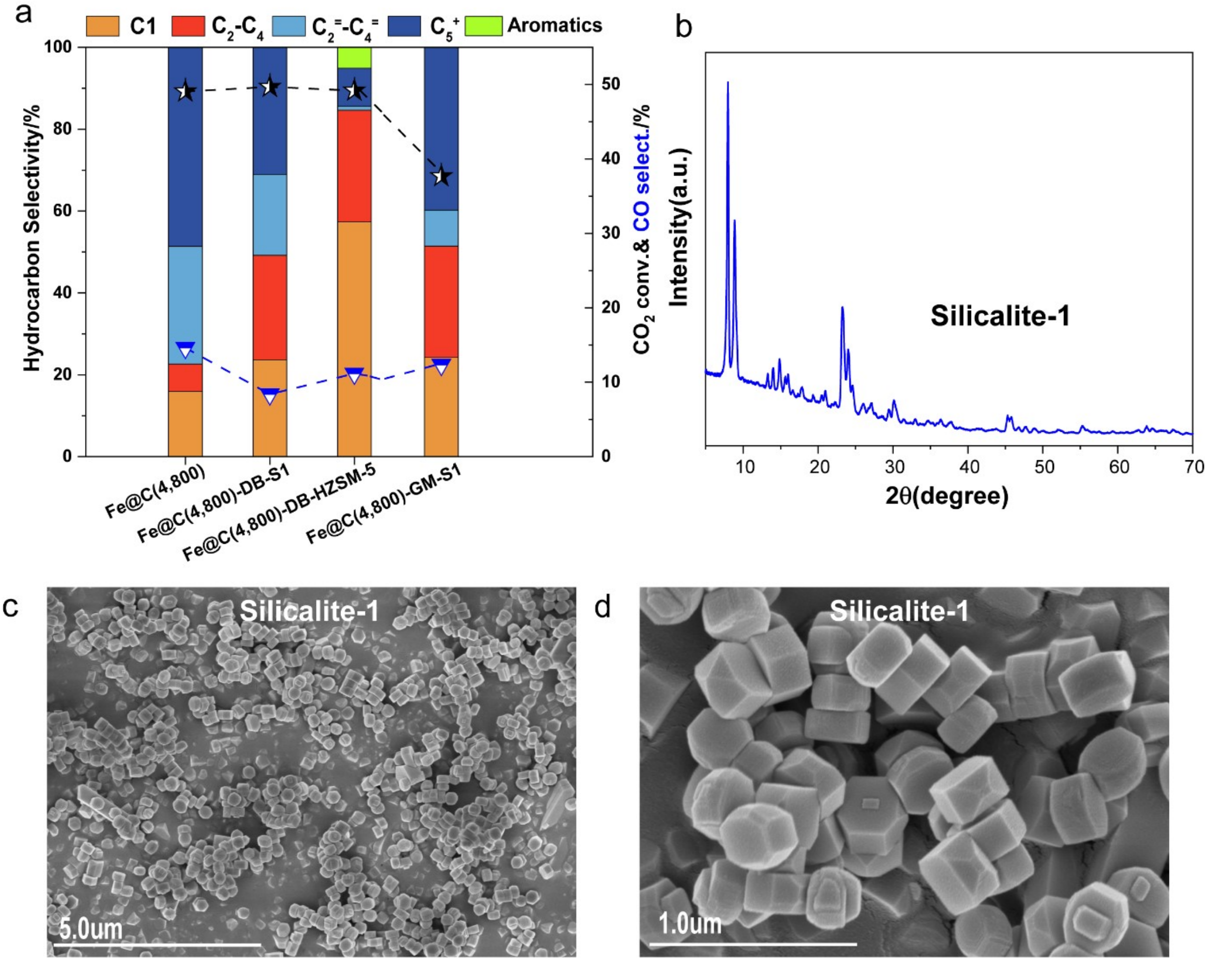

Fig. S92. (a) The catalytic performance evaluation of the hydrogenation of CO_2-to-hydrocarbons process over the bifunctional [Fe@C(4,800) + zeolites] catalytic systems [Reaction conditions: $H_2/CO_2 = 3$, 350 °C, 3 MPa, 18000 mL h^{-1}]. (b) XRD patterns of silicalite-1, (c) SEM image of silicalite-1, (d) SEM image of silicalite-1. Note that synthesized materials were presented in a Fe@C(x,y) manner, where x and y refer to the pyrolysis duration (in hours) and temperature (in °C), respectively.

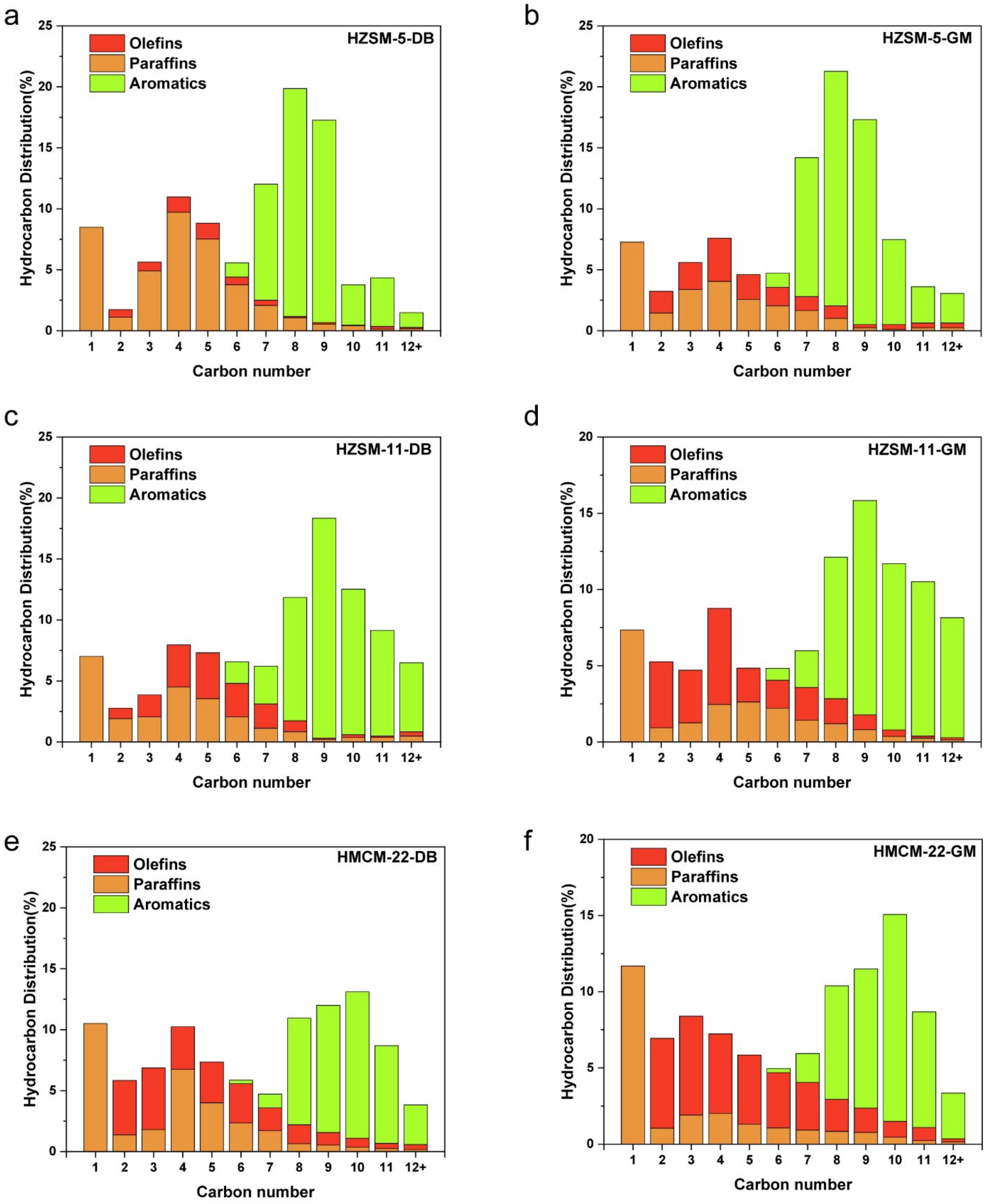

Fig. S93. The product distribution of (a) [4K/Fe@C(4,900) + ZSM-5 (SAR 38)-dual-bed], (b) [4K/Fe@C(4,900) + ZSM-5 (SAR 38)-granule-mixing], (c) [4K/Fe@C(4,900) + ZSM-11-dual-bed], (d) [4K/Fe@C(4,900) + ZSM-11-granule-mixing], (e) [4K/Fe@C(4,900) + MCM-22-dual-bed], (f) [4K/Fe@C(4,900) +MCM-22-granule-mixing] catalysts [Reaction conditions: $H_2/CO_2 = 3$, 350 °C, 3 MPa, 18000 mL g^{-1} h^{-1}]. Note that synthesized materials were presented in a Fe@C(x,y) manner, where x and y refer to the pyrolysis duration (in hours) and temperature (in °C), respectively.

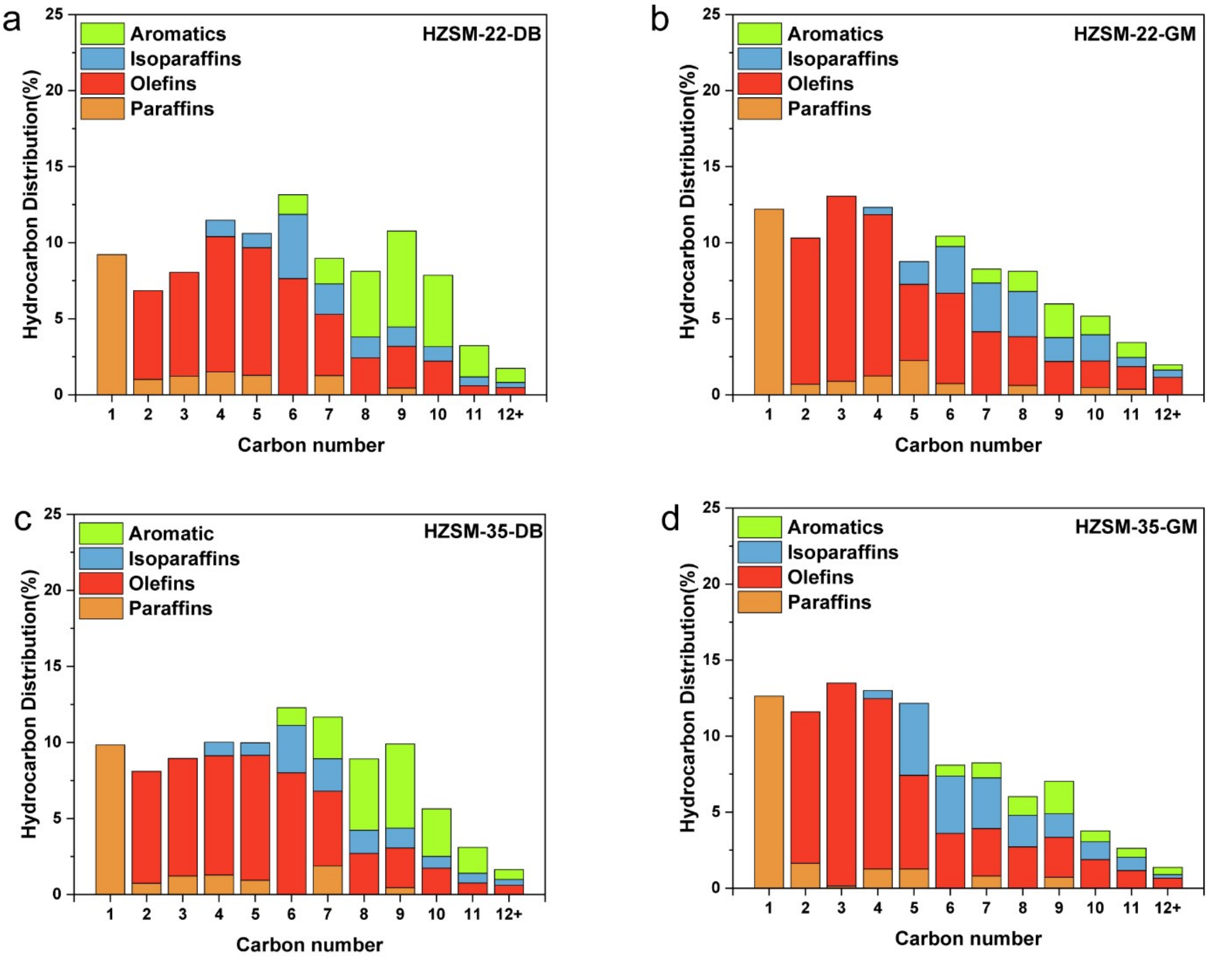

Fig. S94. The product distribution of (a) [4K/Fe@C(4,900) + ZSM-22-dual-bed], (b) [4K/Fe@C(4,900) + ZSM-22-granule-mixing], (c) [4K/Fe@C(4,900) + ZSM-35-dual-bed], (d) [4K/Fe@C(4,900) + ZSM-35-granule-mixing] catalysts [Reaction conditions: $H_2/CO_2 = 3$, 350 °C, 3 MPa, 18000 mL g^{-1} h^{-1}]. Note that synthesized materials were presented in a Fe@C(x,y) manner, where x and y refer to the pyrolysis duration (in hours) and temperature (in °C), respectively.

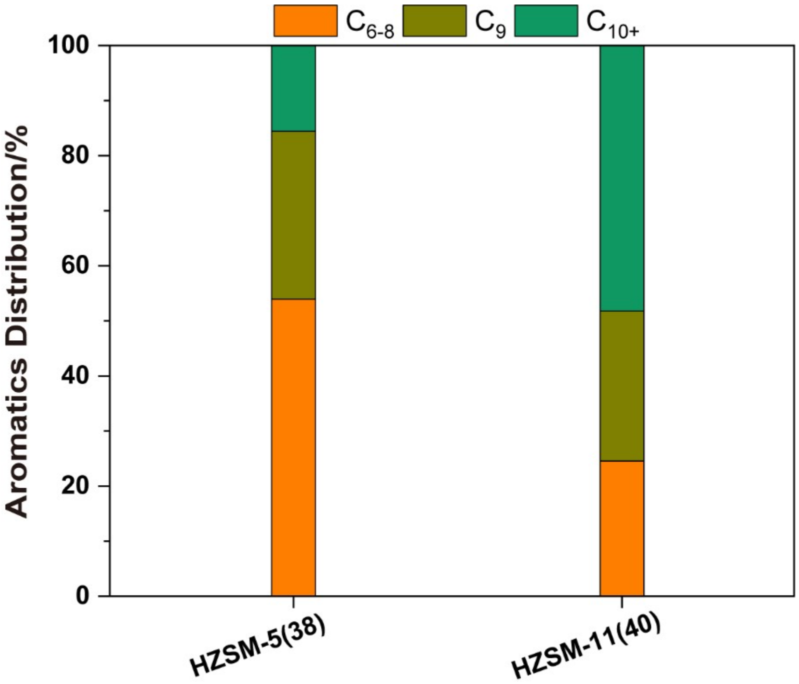

Fig. S95. Aromatic distribution over different bifunctional [4K/Fe@C(4,900) + zeolites-dual-bed] systems, delivering comparable BTX selectivity [Reaction conditions: $H_2/CO_2 = 3$, 350 °C, 3 MPa, 18000 mL g^{-1} h^{-1}]. Note that synthesized materials were presented in a Fe@C(x,y) manner, where x and y refer to the pyrolysis duration (in hours) and temperature (in °C), respectively.

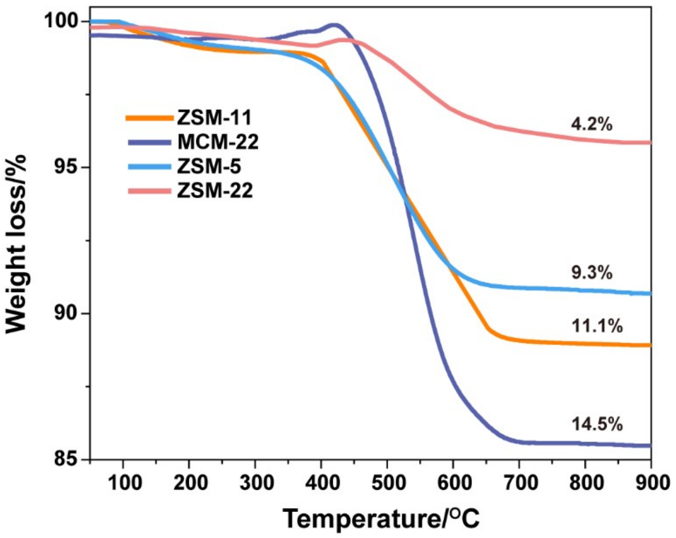

Fig. S96. TG analysis of the reacted zeolites. The reacted zeolites were separated from bifunctional 4K/Fe@C(4,900)+zeolites-dual-bed catalysts after 30 h of reaction.

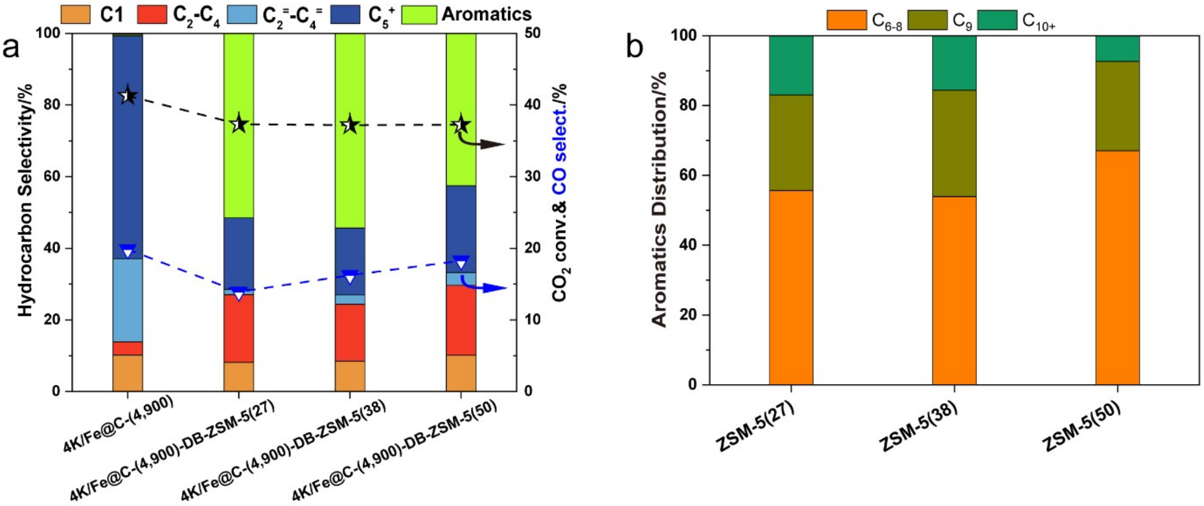

Fig. S97. The catalytic performance evaluation of the hydrogenation of CO_2-to-hydrocarbons process over the bifunctional [4K/Fe@C(4,900) + ZSM-5 with different SARs-dual-bed] catalytic systems: (a) The hydrocarbon distribution. (b) aromatic distribution over different bifunctional [4K/Fe@C(4,900) + ZSM-5 with different SARs-dual-bed] systems, delivering comparable BTX selectivity.[GM: Granule-mixing; DB: Dual-bed; Reaction condition: $H_2/CO_2 = 3$, 350 °C, 3 MPa, 18000 mL g^{-1} h^{-1} at a time on stream of 7 h]. Note that synthesized materials were presented in a Fe@C(x,y) manner, where x and y refer to the pyrolysis duration (in hours) and temperature (in °C), respectively.

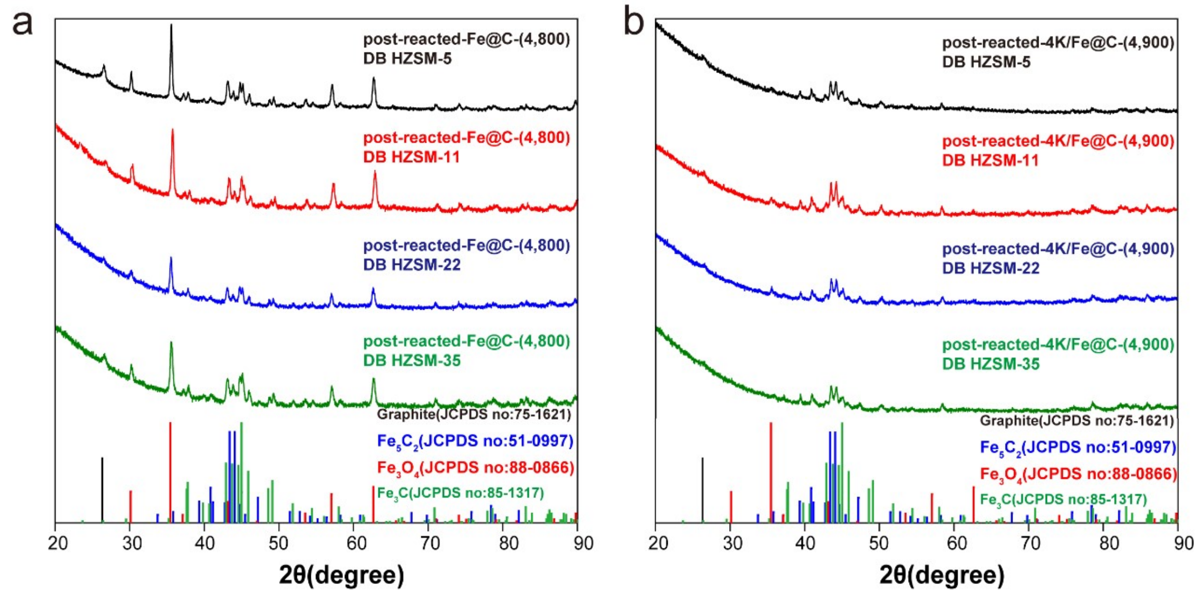

Fig. S98. XRD patterns of post-reacted (a) [Fe@C(4,800) + zeolites-dual-bed] and (b) [4K/Fe@C(4,900) + zoelites-dual-bed] catalysts. Note that synthesized materials were presented in a Fe@C(x,y) manner, where x and y refer to the pyrolysis duration (in hours) and temperature (in °C), respectively. The XRD of Fe@C (4,800) was mainly composed of Fe_3O_4 and Fe_5C_2 after combination reaction with zeolite using a dual-bed manner, which was consistent with the no zeolites combination. The XRD of 4K/Fe@C (4,900) was mainly Fe_5C_2 after combination reaction with zeolite using a dual-bed manner, which was consistent with that of the no zeolites combination.

S3. Supplementary Tables

Table S1. Structural and textural properties of various fresh iron-based catalysts.

Samples	S_{BET}(m^2/g)	V_{total}(cm^3/g)
MIL-100(Fe)	1207.5	0.60
Fe@C(16,700)	28.8	0.07
Fe@C(4,800)	65.6	0.16
Fe@C(16,800)	23.8	0.06
Fe@C(4,900)	60.6	0.13
4K/Fe@C(4,900)	52.4	0.22

Table S2: XRF (X-Ray Fluorescence) elemental and metal oxide analysis of as-synthesized and post-reacted catalysts.

Metal oxide analysis (weight %)

Samples	Na_2O	Fe_2O_3	K_2O	*CaO*	SiO_2	*MnO*
MIL-100(Fe)	0.07	97.23	--	0.11	0.4	0.22
Fe@C(16,700)	0.02	97.49	--	--	0.21	0.27
Fe@C(4,800)	--	99.17	--	--	0.18	0.28
Fe@C(16,800)	0.03	98.86	--	--	0.29	0.3
Fe@C(4,900)	--	99.49	--	--	0.16	0.17
4K/Fe@C(4,900)	--	95.43	3.8	0.07	0.23	0.1
Fe@C(4,800)- post-reacted	--	97.27	--	--	2.12	0.28
4K/Fe@C(4,900)- post-reacted	--	94.72	4.01	--	1.1	0.1

Elemental analysis (weight %)

Samples	*Na*	*Fe*	*K*	*Ca*	*Si*	*Mn*
MIL-100(Fe)	0.05	68.06	--	--	0.19	0.17
Fe@C(16,700)	0.01	68.24	--	--	0.10	0.21
Fe@C(4,800)	--	69.36	--	--	0.08	0.22
Fe@C(16,800)	0.02	69.20	--	--	0.13	0.23
Fe@C(4,900)	--	69.58	--	--	0.07	0.13
4K/Fe@C(4,900)	--	66.80	3.15	0.05	0.11	0.08
Fe@C(4,800)- post-reacted	--	68.09	--	--	0.99	0.22
4K/Fe@C(4,900)- post-reacted	--	66.30	3.33	--	0.51	0.08

Table S3. Full Width Half Maximum (FWHM) values of as-synthesized catalysts.

Samples	Iron distribution/%			Oxygen distribution/%		Carbon distribution/%
	Fe^0	Fe^{2+}	Fe^{3+}	O_L	I_O/ I_{Fe}[a]	C=C
Fe@C(4,800)	18.6	44.0	37.4	34.6	1.12	33.3
Fe@C(16,800)	22.7	39.5	37.8	40.3	1.58	36.2
Fe@C(4,900)	44.1	32.9	23.0	49.9	1.12	36.3
4K/Fe@C(4,900)	9.2	46.9	43.8	35.4	1.28	47.0
post-reacted Fe@C(4,800)	3.8	66.7	29.5	35.8	1.29	36.6
post-reacted Fe@C(16,800)	--	24.8	43.9	45.9	2.09	37.6
post-reacted Fe@C(4,900)	--	52.2	22.7	50.4	1.62	47.6

[a] Surface ratios of the I_O/I_{Fe} on the Fe@C and K/Fe@C catalysts, where I_O and I_{Fe} represent the integrated area of the separate XPS peaks of O 1s and Fe 2p3/2, were obtained by deconvoluting XPS spectra after the corrections by using atomic sensitivity factors. As shown here, it was observed that both the I_O/I_{Fe} ratios on fresh Fe@C(4,800) and Fe@C(4,900) catalysts were relatively low. The I_O/I_{Fe} ratio exhibited significant variation on the 4K/Fe@C(4,900) catalyst, which could be attributed to the further oxidation of Fe induced by K, leading to the formation of more FeO_x species.[22] On the other hand, the I_O/I_{Fe} ratio on the post-reacted catalysts was larger than that on fresh catalysts. This indicates that re-oxidation of fresh catalysts,[23,24]which aligns with the findings of the XRD results (see **Fig.S29, S66**).

Table S4. Surface elements on the Fe based catalysts.

Samples	Fe wt.%		O wt.%		C wt.%		K wt.%	
	Fe[a]	Fe[b]	O[a]	O[b]	C[a]	C[b]	K[a]	K[b]
Fe@C(16,700)	**13.1**	**90.8**	**9.1**	**0.3**	**77.8**	**8.8**	/	/
Fe@C(4,800)	**8.1**	**75.7**	**9.3**	**1.1**	**82.6**	**23.1**	/	/
Fe@C(16,800)	**14.1**	/	**9.6**	/	**76.3**	/	/	/
Fe@C(4,900)	**8.9**	**83.5**	**5.1**	**0.5**	**85.9**	**15.9**	/	**/**
4K/Fe@C(4,900)	**8.8**	**75.1**	**8.7**	**3.7**	**75.9**	**18.1**	**6.5**	**3.11**
post-reacted Fe@C(4,800)	**8.5**	/	**11.1**	/	**80.4**	/	/	**/**
post-reacted Fe@C(16,800)	**24.2**	/	**13.7**	/	**62.1**	/	/	**/**
post-reacted Fe@C(4,900)	**23.3**	/	**16.1**	/	**60.6**	/	/	**/**
post-reacted 4K/Fe@C(4,900)	**8.3**	/	**10.5**	/	**73.6**	/	**7.6**	**/**

[a] The data in white square was obtained by XPS.

[b] The data in the grey zone was obtained by EDS from HRTEM.

Table S5. Acidity properties of various zeolites.

Zeolites	Acidity by strength (mmol·g^{-1})[a]				
	Weak	Strong	Strong/Total	Weak/Strong	Total
ZSM-22	0.23	0.09	0.28	2.55	0.32
ZSM-35	0.50	0.17	0.25	2.94	0.67
MCM-22	0.28	0.08	0.22	3.50	0.36
ZSM-5	0.37	0.22	0.37	1.68	0.59
ZSM-11	0.21	0.10	0.32	2.10	0.31

[a] By deconvolution of NH_3-TPD profiles.

Table S6. Physiochemical properties of zeolites.

Zeolites	S_{BET}(m^2/g)	S_{micro}(m^2/g)	S_{meso}(m^2/g)	V_{micro}(cm^3/g)	V_{total}(cm^3/g)
ZSM-22	180	152	28	0.18	0.25
ZSM-35	400	330	70	0.11	0.18
MCM-22	440	379	61	0.42	0.59
ZSM-5	350	308	42	0.08	0.10
ZSM-11	350	251	99	0.27	0.31

Table S7. Physiochemical properties of zeolites.

Zeolites	Pore size(nm^2)	SiO_2/Al_2O_3[a]
ZSM-22	0.46×0.57	42
ZSM-35	0.42×0.54, 0.32×0.48	25
MCM-22	0.40×0.55, 0.41×0.51	28
ZSM-5	0.51×0.55, 0.53×0.56	38
ZSM-11	0.53×0.54	40

[a] SAR was obtained from an X-ray Fluorescence Spectrometer.

Table S8. Structural properties of various zeolites

Zeolites	Topology	Channel		D_{max} (nm)[a]
		Dimensionality	Pore size (nm^2)	
ZSM-22	TON	1D	10MR, 0.46×0.57	0.57
ZSM-35	FER	2D	10MR, 0.42×0.54; 8MR, 0.35×0.48	0.63
MCM-22	MWW	2D	10MR, 0.40×0.55; 10MR, 0.41×0.51	0.97
ZSM-5	MFI	3D	10MR, 0.53×0.56; 10MR, 0.51×0.55	0.64
ZSM-11	MEL	3D	10MR, 0.53×0.54	0.77

[a] Maximum diameter of a sphere that can be included.

Table S9. Summary of the MOF-derived catalysts and their catalytic performance for hydrocarbon synthesis from CO_2 hydrogenation.

Entry	Catalysts	Reaction conditions				CO_2 conv.(%)	CO sel.(%)	Hydrocarbon distribution (%)					Ref
		H_2/ CO_2	T/ (°C)	P/MPa	GHSV[a]			CH_4	C_2-C_4	$C_2^=$-$C_4^=$	C_5^+	Aro.	
1	Basolite F300	3	350	3.0	24000	38	18	24	14(C_2-C_6)	46(C_2-$C_6^=$)	16(C_{7+})		3
2	ZIF-8/Fe_2O_3	3	300	3.0	3600	30	18	35	44	7	14	--	25
3	Fe-MIL-88B	3	400	1.0	3600	46	17	32	18	23	27	--	26
4	Fe@MIL-53(Al)	3	300	3.0	3600	22	20	50	43	1	6	--	25
5	Ni@MOF-5	4	280	1.0	2000	75	1	100	--	--	--	--	27
6	Ni@UiO-99	8	350	1.0	1650	47	17	100	--	--	--	--	28
7	Ni@MIL-101	8	320	1.0	4650	56	9	100	--	--	--	--	28
8	FeZn@ZIF-8	3	320	3.0	7200	29	20	21	8	37	34	--	29
9	FeZnK@ZIF-8	3	320	3.0	7200	34	21	24	7	41	28	--	29
10	Ni@MIL-101-Al_2O_3	5	350	1.0	4650	85	15	100	--	--	--	--	30
11	Co@MIL-53(Al)	2.7	340	3.0	800	37	3	53	24	--	23	--	31
12	K/Fe@NC-400	3	320	3.0	7200	31	19	21	8	41	30	--	32
13	FeCo/NC-600	3	320	2.0	6240	37	1	45	21	27	7	--	33
14	K/Fe@C-MIL-100	3	350	3.0	4800	48	16	12	7	21	59	1	4
15	Fe@C(4,800)	3	350	3.0	4800	49	15	16	6	28	49	0.9	TW[b]
16	4K/Fe@C(4,900)	3	350	3.0	18000	41	19	10	4	22	63	1	TW[b]
17	8K/Fe@C(4,900)	3	350	3.0	24000	34	26	12	5	26	56	0.9	TW[b]
18	8K/Fe@C(4,900)	3	350	3.0	36000	35	33	16	7	25	51	0.9	TW[b]

[a] GHSV: ($mL \cdot g^{-1} \cdot h^{-1}$).

[b] This work.

Table S10. Summary of representative reported catalysts and their catalytic performance for hydrocarbon synthesis from CO_2 hydrogenation.

Entry	Catalysts	Reaction conditions				CO_2 conv.(%)	CO sel.(%)	Hydrocarbon distribution (%)					Ref
		H_2/CO_2	T/ (^oC)	P/MPa	GHSV[a]			CH_4	C_2-C_4	$C_2^=$-$C_4^=$	C_5^+	C_{5+} productivity ($mL\cdot g_{cat}^{-1}\cdot h^{-1}$)[b]	
1	10Fe0.8K1.11Co	3	300	2.5	560	57.2	1.6	22.4	8.7	23.5	43.8	140.3	[34]
2	22Fe3K/$CuAl_2O_4$	3	320	3	20000	36.8	16.5	14.3	11.4	29	45.2	565.0	[35]
3	Na–Fe_3O_4	3	320	3	4000	34.0	14.0	12.0	48.0	--	40.0	117.0	[36]
4	Na–CoCu/TiO_2	3	250	5	3000	18.4	30.2	26.1	31.8	--	42.1	38.9	[37]
5	ZnFeOx	3	320	3	4000	38.4	11.2	11.0	4.5	34.8	49.7	154.8	[38]
6	15Fe–K/m-ZrO_2	3	320	1.5	10000	38.8	19.9	30.1	12.8	42.8	14.3	66.1	[39]
7	Fe_2N@C	4	250	1	36000	33.7	15.8	46.0	15.4	31	7.5	157.6	[40]
8	5Zn–FeAlK	3	300	2.5	4500	38.6	8.0	8.2	17.4	--	73.8	283.0	[41]
9	K0.016Pd0.12Fe	3	340	3.0	6000	41.8	33.8	17.2	12.1	21.5	70.6	288.0	[42]
10	FeK/MPC	3	300	2.5	8000	50.6	8.2	16.8	34.7	--	48.5	432.3	[43]
11	KZnFe-5.0Co	3	320	2.0	6000	50.2	8.1	11.5	30.7	--	57.8	392.5	[44]
12	K/Fe@C-MIL-100	3	350	3.0	4800	48	16	12	7	22	59	274.1	[4]
13	Fe@C(4,800)	3	350	3.0	4800	49	15	16	6	29	49	235.1	TW[c]
14	4K/Fe@C(4,900)	3	350	3.0	18000	41	19	10	4	23	63	899.6	TW[c]
15	4K/Fe@C(4,900)	3	350	3.0	36000	36	19	29	13	14	44	1106.6	TW[c]
16	8K/Fe@C(4,900)	3	350	3.0	24000	34	26	12	5	27	56	803.6	TW[c]
17	8K/Fe@C(4,900)	3	350	3.0	36000	35	33	16	7	26	51	1061.9	TW[c]

[a] GHSV: ($mL\cdot g^{-1}\cdot h^{-1}$).

[b] C_{5+} productivity $=GHSV_{CO2} * C_{5+}$ yield.

[c] This work.

Table S11. Summary of the representative catalysts and their catalytic performance for aromatic synthesis from CO_2 hydrogenation via CO_2 – FTS mechanism

Entry	Catalysts	SiO_2/Al_2O_3	Reaction conditions				CO_2 conv.(%)	CO sel.(%)	Hydrocarbon distribution (%)				*Aro.*productivity($mL\cdot g^{-1}\cdot h^{-1}$)[b]	Ref
			H_2/CO_2	T/ (°C)	P/MPa	GHSV[a]			CH_4	C_2-C_4	C_5^+	Aro.		
1	Na–Fe_3O_4/HZSM-5	160	3	320	3.0	4000	22	20	4	17	30	49	82	[36]
2	Na-Fe/HZSM-5	25	3	340	1.0	4800	31	26	27	29	3	41	108	[45]
3	#1Na–Fe/HZSM-5	60	3	340	3.0	4000	45	11	9	25	10	56	215	[46]
4	Cr_2O_3/Zn-ZSM-5@SiO_2	80	3	350	3.0	1500	22	35	4	23	3	70	36	[47]
5	Na-Fe@C/HZSM-5	60	3	320	3.0	9000	33	13	5	10	35	50	310	[48]
6	Na–Fe_3O_4/HZSM-5	25	2	320	3.0	4000	29	15	6	33	18	43	101	[49]
7	Fe_2O_3@KO_2/ZSM-5	26	3	375	3.0	5000	49	13	14	46	15	25	127	[50]
8	#Fe-K/a-Al&P/ZSM-5	50	1	400	3.0	3000	36	10	11	40	10	39	90	[48]
9	$ZnFeO_x$-Na/S-HZSM-5	50	3	340	2.0	2600	35	39	4	4	24	68	90	[51]
10	#$ZnFeO_x$-Na/SHZSM5	25	3	320	3.0	4000	37	11	10	28	21	41	129	[45]
11	#Cu-Fe_2O_3/HZSM-5	50	3	320	3	1000	57	4	11	9	23	57	74	[52]
12	4K/Fe@C(4,900) /HZSM-5	38	3	350	3.0	18000	37	16	9	20	18	53	711	TW[c]
13	4K/Fe@C(4,900) /HZSM-11	40	3	350	3.0	18000	36	15	7	14	12	67	885	TW[c]
14	4K/Fe@C(4,900) /HZSM-5	27	3	350	3.0	18000	37	14	8	20	19	53	728	TW[c]
15	4K/Fe@C(4,900) /HZSM-5	50	3	350	3.0	18000	37	18	10	23	24	43	563	TW[c]

[a] GHSV: ($mL\cdot g^{-1}\cdot h^{-1}$).

[b] *Aro.*productivity=$GHSV_{CO2}$**Aromatics* yield.

[c] This work.

S4. Supplementary References

1 M. Sanchez-Sanchez, I. De Asua, D. Ruano and K. Diaz, *Cryst Growth Des*, 2015, **15**, 4498–4506.

2 K. Guesh, C. A. D. Caiuby, Á. Mayoral, M. Díaz-García, I. Díaz and M. Sanchez-Sanchez, *Cryst Growth Des*, 2017, **17**, 1806–1813.

3 A. Ramirez, L. Gevers, A. Bavykina, S. Ould-Chikh and J. Gascon, *ACS Catal*, 2018, **8**, 9174–9182.

4 S. Jiang, X. Gong, X. You, X. Zhang, Y. Li and A. D. Chowdhury, *CCS Chemistry*, 2024, 1–18.

5 C. Wang, W. Fang, Z. Liu, L. Wang, Z. Liao, Y. Yang, H. Li, L. Liu, H. Zhou, X. Qin, S. Xu, X. Chu, Y. Wang, A. Zheng and F. S. Xiao, *Nat Nanotechnol*, 2022, **17**, 714–720.

6 N. Lohitharn, J. G. Goodwin and E. Lotero, *J Catal*, 2008, **255**, 104–113.

7 X. Gong, A. Ramirez, E. Abou-Hamad, T. B. Shoinkhorova, M. Çağlayan, Y. Ye, W. Wang, N. Wehbe, R. Khairova, A. D. Chowdhury and J. Gascon, *Chem Catalysis*, 2022, **2**, 2328–2345.

8 Y. Fang, Z. Yang, H. Li and X. Liu, *Environmental Science and Pollution Research*, 2020, **27**, 4703–4724.

9 I. Bezverkhyy, G. Weber and J. P. Bellat, *Microporous and Mesoporous Materials*, 2016, **219**, 117–124.

10 X. Yang, X. Guo, C. Zhang, X. Wang, Y. Yang and Y. Li, *Acta Chimi Sin*, 2017, **75**, 360–366.

11 Y. Xu, H. Liang, R. Li, Z. Zhang, C. Qin, D. Xu, H. Fan, B. Hou, J. Wang, X. K. Gu and M. Ding, *Angewandte Chemie - International Edition*, 2023, **62**, e202306786.

12 K. Wu, Z. Zhang, R. Shan, L. Li, J. Wang, B. Hou, Y. Xu and M. Ding, *Appl Catal B*, 2024, **353**, 124067.

13 S. Munir, M. Amin, N. Iqbal, A. Iqbal and A. A. Ghfar, *Front Chem*, 2023, **11**, 1150565.

14 Y. Liang, X. Feng, L. Zhi, U. Kolb and K. Müllen, *Chemical Communications*, 2009, 809–811.

15 L. Hu, Y. Huang, F. Zhang and Q. Chen, *Nanoscale*, 2013, **5**, 4186–4190.

16 A. Molino, J. Holzinger, K. A. Łukaszuk, D. Rojo-Gama, A. E. Gunnæs, J. Skibsted, L. F. Lundegaard, S. Svelle, P. Beato, S. Bordiga and K. P. Lillerud, *Catal Sci Technol*, 2019, **9**, 6782–6792.

17 S. Xiong, J. Sun, H. Li, W. Wang and W. Wu, *Microporous and Mesoporous Materials*, 2024, **365**, 112895.

18 S. M. Al-Jubouri, *Microporous and Mesoporous Materials*, 2020, **303**, 110296.

19 G. V. A. Martins, G. Berlier, C. Bisio, S. Coluccia, H. O. Pastore and L. Marchese, *Journal of Physical Chemistry C*, 2008, **112**, 7193–7200.

20 M. Zhang, Y. Chen, L. Wang, Q. Zhang, C. W. Tsang and C. Liang, *Ind Eng Chem Res*, 2016, **55**, 6069–6078.

21 J. Wei, Q. Ge, R. Yao, Z. Wen, C. Fang, L. Guo, H. Xu and J. Sun, *Nat Commun*, 2017, **8**, 15174.

22 J. M. Cho, B. G. Kim, G. Y. Han, J. Sun, H. K. Jeong and J. W. Bae, *Fuel*, 2020, **281**, 118779.

23 P. A. Chernavskii, G. V. Pankina, R. V. Kazantsev and O. L. Eliseev, *ChemCatChem*, 2018,

10, 1313–1320.

24 A. Ramirez, L. Gevers, A. Bavykina, S. Ould-Chikh and J. Gascon, *ACS Catal*, 2018, **8**, 9174–9182.

25 S. Hu, M. Liu, F. Ding, C. Song, G. Zhang and X. Guo, *Journal of CO2 Utilization*, 2016, **15**, 89–95.

26 J. Liu, A. Zhang, M. Liu, S. Hu, F. Ding, C. Song and X. Guo, *Journal of CO2 Utilization*, 2017, **21**, 100–107.

27 W. Zhen, B. Li, G. Lu and J. Ma, *Chemical Communications*, 2015, **51**, 1728–1731.

28 M. Mihet, O. Grad, G. Blanita, T. Radu and M. D. Lazar, *Int J Hydrogen Energy*, 2019, **44**, 13383–13396.

29 J. Liu, Y. Sun, X. Jiang, A. Zhang, C. Song and X. Guo, *Journal of CO2 Utilization*, 2018, **25**, 120–127.

30 O. Grad, M. Mihet, G. Blanita, M. Dan, L. Barbu-Tudoran and M. D. Lazar, *Catal Today*, 2021, **366**, 114–122.

31 A. L. Tarasov, V. I. Isaeva, O. P. Tkachenko, V. V. Chernyshev and L. M. Kustov, *Fuel Processing Technology*, 2018, **176**, 101–106.

32 J. Liu, A. Zhang, X. Jiang, G. Zhang, Y. Sun, M. Liu, F. Ding, C. Song and X. Guo, *Ind Eng Chem Res*, 2019, **58**, 4017–4023.

33 Z. Dong, J. Zhao, Y. Tian, B. Zhang and Y. Wu, *Catalysts*, 2020, **10**, 455.

34 F. Jiang, B. Liu, S. Geng, Y. Xu and X. Liu, *Catal Sci Technol*, 2018, **8**, 4097–4107.

35 Y. Kim, Y. Song, Y. Kim and K. Na, *J Mater Chem A Mater*.

36 J. Wei, Q. Ge, R. Yao, Z. Wen, C. Fang, L. Guo, H. Xu and J. Sun, *Nat Commun*, 2017, **8**, 1–8.

37 Z. Shi, H. Yang, P. Gao, X. Chen, H. Liu, L. Zhong, H. Wang, W. Wei and Y. Sun, *Chinese Journal of Catalysis*, 2018, **39**, 1294–1302.

38 X. Cui, P. Gao, S. Li, C. Yang, Z. Liu, H. Wang, L. Zhong and Y. Sun, *ACS Catal*, 2019, **9**, 3866–3876.

39 J. Huang, S. Jiang, M. Wang, X. Wang, J. Gao and C. Song, *ACS Sustain Chem Eng*, 2021, **9**, 7891–7903.

40 B. Zhao, M. Sun, F. Chen, Y. Shi, Y. Yu, X. Li and B. Zhang, *Angewandte Chemie - International Edition*, 2021, **60**, 4496–4500.

41 K. Nasriddinov, J. E. Min, H. G. Park, S. J. Han, J. Chen, K. W. Jun and S. K. Kim, *Catal Sci Technol*, 2022, **12**, 906–915.

42 L. Xiong, S. Liu, Y. Men, L. Li, X. Niu, K. Guo, J. Xu, W. An, J. Wang and Y. Cong, *J Environ Chem Eng*, 2022, **10**, 108407.

43 S. M. Hwang, C. Zhang, S. J. Han, H. G. Park, Y. T. Kim, S. Yang, K. W. Jun and S. K. Kim, *Journal of CO2 Utilization*, 2020, **37**, 65–73.

44 L. Guo, X. Gao, W. Gao, H. Wu, X. Wang, S. Sun, Y. Wei, Y. Kugue, X. Guo, J. Sun and N. Tsubaki, *Chem Sci*, 2022, **14**, 171–178.

45 Y. Xu, C. Shi, B. Liu, T. Wang, J. Zheng, W. Li, D. Liu and X. Liu, *Catal Sci Technol*, 2019, **9**, 593–610.

46 C. Wen, J. Jiang, C. Chiliu, Z. Tian, X. Xu, J. Wu, C. Wang and L. Ma, *Energy and Fuels*, 2020, **34**, 11282–11289.

47 Y. Wang, W. Gao, S. Kazumi, H. Li, G. Yang and N. Tsubaki, *Chemistry - A European*

Journal, 2019, **25**, 5149–5153.

48 Y. Wang, S. Kazumi, W. Gao, X. Gao, H. Li, X. Guo, Y. Yoneyama, G. Yang and N. Tsubaki, *Appl Catal B*, 2020, **269**, 118792.

49 J. Wei, R. Yao, Q. Ge, D. Xu, C. Fang, J. Zhang, H. Xu and J. Sun, *Appl Catal B*, 2021, **283**, 119648.

50 A. Ramirez, A. Dutta Chowdhury, A. Dokania, P. Cnudde, M. Caglayan, I. Yarulina, E. Abou-Hamad, L. Gevers, S. Ould-Chikh, K. De Wispelaere, V. Van Speybroeck and J. Gascon, *ACS Catal*, 2019, **9**, 6320–6334.

51 S. Wang, T. Wu, J. Lin, J. Tian, Y. Ji, Y. Pei, S. Yan, M. Qiao, H. Xu and B. Zong, *ACS Sustain Chem Eng*, 2019, **7**, 17825–17833.

52 G. Song, M. Li, P. Yan, M. A. Nawaz and D. Liu, *ACS Catal*, 2020, **10**, 11268–11279.